EFFECT OF POLY(METHYL METHACRYLATE) WRAPPING ON THE STRUCTURE AND PROPERTIES OF CNT FILMS, AND POLYMER/CNT FILMS AND FIBERS

A Dissertation
Presented to
THE ACADEMIC FACULTY

By

Amir Ahmad Bakhtiary Davijani

In Partial Fulfillment
of the Requirements for the Degree
Doctor of Philosophy in the
School of Materials Science and Engineering

Georgia Institute of Technology

May 2017

EFFECT OF POLY(METHYL METHACRYLATE) WRAPPING ON THE STRUCTURE AND PROPERTIES OF CNT FILMS, AND POLYMER/CNT FILMS AND FIBERS

Approved by:

Dr. Satish Kumar, Advisor
School of Materials Science and Engineering
Georgia Institute of Technology

Dr. Hamid Garmestani
School of Materials Science and Engineering
Georgia Institute of Technology

Dr. Karl Jacob
School of Materials Science and Engineering
Georgia Institute of Technology

Dr. Seung Woo Lee
School of Mechanical Engineering
Georgia Institute of Technology

Dr. Donggang Yao
School of Materials Science and Engineering
Georgia Institute of Technology

Date Approved: January 20, 2017

ACKNOWLEDGEMENTS

Writing this dissertation would not have been possible without guidance and assistance from many people. First and foremost, I would like to thank Dr. Satish Kumar, for providing me with this opportunity and his continued support throughout the years. His encouragement and guidance resulted in improvement of the current work, and more importantly my analytical skills.

I would like to thank my committee members Dr. Hamid Garmestani, Dr. Karl Jacob, Dr. Seung Woo Lee, and Dr. Donggang Yao for the constructive advice.

I would like to express my gratitude to the following people; Dr. An-Ting Chien for his assistance with XRD and providing invaluable advice; Dr. Brad Newcomb for help with Raman spectroscopy and valuable discussions; Clive Liu for our daily scientific discussions, providing his input on many subjects, and assistance in experiments; Huibin Chang, Po-Hsiang Wang and Jeff Luo for helping overcome experimental challenges and valuable discussions. I would like to thank Dr. Yaodong liu, Dr. Kishor Gupta and Dr. Reza Kavian for sample preparation and electrochemistry training, and Dr. Han Gi Chae and Dr. Prabhakar Gulgunje for their input and assistance.

Finally, I would like to thank my parents for instilling the values of hard work and resilience, and for their unconditional support throughout all stages of my life, and my wife, Atefeh, for her support, sacrifices and love.

TABLE OF CONTENTS

LIST OF TABLES

LIST OF FIGURES

SUMMARY

Carbon nanotubes (CNTs) exhibit high electrical and thermal conductivity and good mechanical properties, making them suitable fillers for composites. Their effectiveness as a filler is affected by their state of aggregation. Various solvents, surfactants, and processing techniques have been studied to improve CNT dispersion in polymers. However, prior to this work there is no suitable solution for achieving good CNT dispersion. In this study, a novel process has been developed that prevents CNT aggregation. Ordered helical wrapping of poly (methyl methacrylate) (PMMA) has been achieved on single wall carbon nanotubes (SWNTs). PMMA wrapped SWNT dispersions in dimethylformamide (DMF) are found to be stable for over three months at room temperature. Ordered PMMA wrapping has been confirmed by X-ray diffraction, and the wrapping behavior has also been verified using molecular modeling. PMMA only wraps on SWNTs with diameter of ~1 nm and not on larger diameter CNTs, such as few wall and multi wall carbon nanotubes. PMMA wrapped SWNT dispersions have also been characterized using UV-vis and Raman spectroscopy which confirm exfoliation of PMMA wrapped SWNTs.

The novel finding has been successfully leveraged for electrical energy storage and mechanical reinforcement. SWNT buckypapers, typically have a surface area of about 650 m^2/g. Using PMMA wrapping, SWNT buckypapers with surface area as high as 950 m^2/g have been processed. These buckypapers exhibited significantly higher energy storage performance when used as electrodes in electrochemical supercapacitor. At a given power density, the energy density of the high surface electrodes was more than

four times higher than the best value reported in the literature to-date for carbon nanotube or graphene electrodes.

Wrapping SWNTs with PMMA in buckypaper increased the modulus and tensile strength by a factor of 5.9 and 3.7, respectively, compared to pristine SWNT buckypaper. Stress transfer studies on buckypapers revealed that while non-wrapped SWNTs experienced negligible stress during deformation, PMMA wrapped SWNTs took up to ~1 GPa stress before mechanical failure of the buckypaper. The modulus of composite films with PMMA wrapped SWNTs was 75 % higher than non-wrapped SWNT films. The effect of PMMA wrapping on thermomechanical properties and electrical conductivity of composite films is also reported.

PMMA wrapped and non-wrapped SWNTs were incorporated in PAN fibers and the effect of PMMA wrapping on mechanical properties, and stress transfer was characterized. The stress transfer analysis of SWNTs in precursor fiber indicated 45 % higher interfacial shear strength in PMMA wrapped SWNTs compared to non-wrapped SWNTs. PMMA wrapping effectively debundled SWNTs in the PAN fibers as evidenced by Raman spectroscopy of the precursor fiber. SEM images of the carbon fiber fracture surface revealed 60% reduction in fibril size when PMMA wrapped SWNTs were used instead of non-wrapped SWNTs.

CHAPTER 1

INTRODUCTION

1.1 Overview

Carbon nanotubes (CNTs) are an allotrope of carbon that have received a lot of attention since their discovery due to their electrical, mechanical, optical and thermal properties. Despite its scientific popularity, the high cost associated with CNTs and complexity of processing them has limited their wide spread use and restricted them to high-end applications and basic fundamental research. Carbon nanotubes can be utilized in different ways, as filler materials, such as in nanocomposites and fibers, or in freestanding form, buckypapers (CNT mats) and CNT fibers. Carbon nanotubes tend to aggregate due to the van der Waals force between them. This limits their applicability as functional fillers in other materials or as free standing CNT films. Improving the dispersion of CNTs in composites has always been a challenge. Due to aggregation, they typically form bundles and the bundles form globules, which is typically detrimental for the intended functional properties of the composite, such as electrical conductivity, mechanical, magnetic and optical properties. For electrical conductivity, aggregation increases the percolation threshold and may even prevent conductivity at higher CNT content [1].

1.2 Carbon Nanotubes

At first glance, carbon seems to be a simple element. Carbon is a very versatile element; its compounds are the basis of life on earth, hydrocarbons are by far the most common source of fuel, and the properties of its allotropes vary widely. Its allotropes include graphite, diamond, amorphous carbon, C_{60} and carbon nanotubes (Figure 1-1). When in diamond form, carbon is the hardest bulk material, it has great thermal conductivity while being an insulator, whereas in graphitic form it is soft and conductive. The properties of carbon depend on how it is bonded to other carbon atoms or other atoms. It is the type of covalent bonding that defines the structure and ultimately the properties of the material, which also influences the monetary value. During recent decades the discovery of nanoscale structures has greatly revived interest in this element. Buckyballs were discovered by Kroto et al. in 1985 [2] followed by the discovery of carbon nanotubes by Ijima in 1991 [3]. Carbon nanotubes are cylindrical nanostructures which can have a very large aspect ratio. CNTs can have different chiralities and can be uniquely defined by a pair of indices (*n,m*). Values *n* and *m* represent the number of unit vectors in the hexagonal 2-D lattice of graphene as shown in Figure 1-2. The band gap varies with these indices, (*n,m*), and their electrical conductivity can show metallic or semiconducting behavior. As a general rule the nanotube is a metallic if $n - m = 3i$, i is an integer, otherwise it is a semiconductor. Armchair and zig-zag CNTs are chiralities that have indices $n = m$ and $m = 0$ (Figure 1-3), respectively, otherwise CNTs are referred to as chiral. Carbon nanotubes can also consist of multiple CNTs inside one another, referred to as multi-walled CNTs (MWNT). The synthesis technique determines what types of tubes are made and the production yield. These techniques include arc

discharge [4], laser ablation [5], and chemical vapor deposition (CVD) [6]. Recent focus has been on chirality selective synthesis to produce specific chirality CNTs [7, 8].

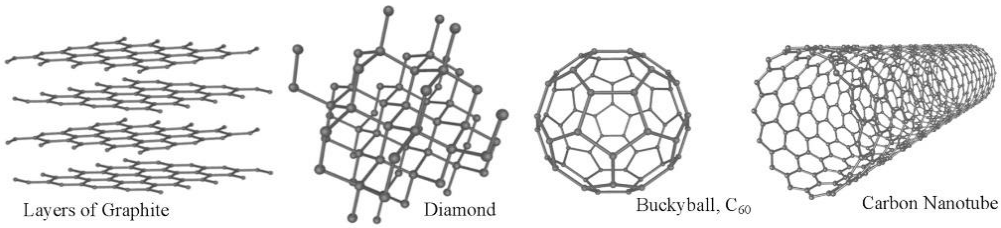

Figure 1-1. Various allotropes of carbon [9].

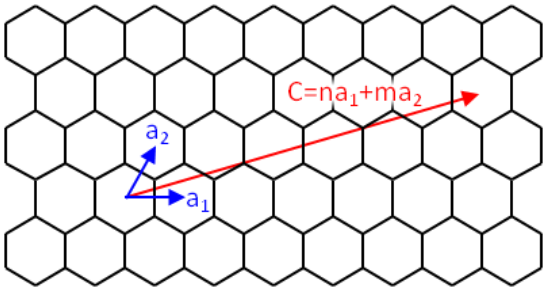

Figure 1-2. Nanotube chirality (n,m) can be thought of as a vector, C, in graphene sheet that describes how to roll the graphene sheet to make the nanotube. The vector perpendicular to C is the CNT axis, and a_1 and a_2 are the unit vectors of graphene.

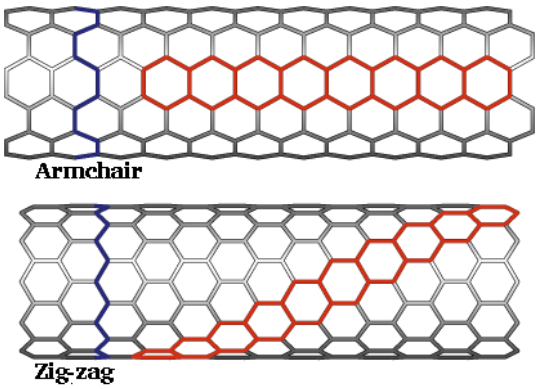

Figure 1-3. Two specific types of chiralities are armchair CNTs when $n = m$, and zig-zag CNTs when $m = 0$.

1.2.1 CNT Aggregation and Dispersing CNTs

Different solvents, techniques and matrix materials have been investigated to improve CNT dispersions. While some solvents have been shown to be more effective in dispersing nanotubes, such as nitromethane and DMF, others, such as toluene and Methyl ethyl ketone are not as good [10]. The solvent-CNT interaction plays a big role in the dispersion of the CNTs, obviously a better interaction will lead to less aggregation of the nanotubes. Dispersing CNTs can be done in several ways. Depending on the dispersing media, solvent or polymer, different approaches can be used. In solvents, sonication, homogenization and microfluidization [11, 12] have been shown to be effective to disperse nanotubes. These methods shear, cut and debundle nanotubes, resulting in smaller bundles and mostly shorter nanotubes. However, after debundling, the nanotubes are free to bundle again and form aggregates. To prevent re-aggregation, surfactants are added to the suspension. These surfactants have hydrophilic and hydrophobic ends and facilitate suspending CNTs in less favorable solvents, such as water. The hydrophobic end interacts with the CNTs while the hydrophilic tail interacts with water for dissolution. Rastogi et al.[13] investigated four different types of surfactants, Triton X-100, sodium dodecylsulfate (SDS), Tween 20, and Tween 80, with CNTs, concluding that Triton X-100 is the most effective between them, resulting in bundle size as small as 4 nm, without specifying the number of walls and outer diameter of the MWNTs. They reported a 90% extractability at a CNT concentration of 40 mg/L with CNT:Triton-X100 1:350. The large amount of surfactant with respect to MWNTs was attributed to the large surface-to-weight ratio of carbon nanotubes. Therefore, it can be deduced that single wall carbon nanotubes (SWNTs) would require much higher surfactant concentration. Another study

investigated different conditions for suspending SWNTs in Aqueous Solutions of the Anionic Surfactant NaDDBS [14] and found a maximum stable concentration of 260 mg/L.

Another approach is to functionalize the nanotubes to improve their interaction with the solvent or matrix. CNTs are typically functionalized using acid treatment to introduce carboxylic acid or hydroxyl groups on the side of carbon nanotubes [15-17]. These functional groups enable suspension of CNTs in aqueous solvents, whereas they would aggregate and sediment without functionalization. Since the functional groups are covalently bonded to CNTs, they open the π-bonds and alter the structural integrity of the CNTs, which can affect the electrical and mechanical properties. Surfactants such as SDS have been used to functionalize SWNTs[18]. This has been done with and without solvent. The advantage of the solvent-free method is obviously that solvent will not be required. However, more exfoliation and debundling is achieved with solvent and prior sonication. The SWNTs are sonicated in SDS, centrifuging the dispersion to sediment the bundles and extracting the upper 75% of the suspension. This suspension was functionalized with diazonium salts which could be completely removed through thermal treatment. The thermal treatment returned the SWNTs to their pristine condition according to Raman spectroscopy. TEM was used to determine improvement of the dispersion by measuring the bundle size.

Polymers have also been used to improve CNT dispersions. Star et al.[19] used the rigid polymer poly(metaphenylenevinylene) (PmPV) to improve SWNT dispersion in DMF. It was found that as the polymer concentration was increased, the dispersion improved, from an average bundle diameter of 7.1 nm to 3.2 nm using atomic force

microscopy (AFM), and the bundle diameter distribution narrowed down, indicating that the polymer had wrapped bundles, not individual CNTs.

Dispersing CNTs in many polymers including PMMA has been extensively studied. Considering CNT/PMMA nanocomposite, some studies have suggested different methods to improve CNT dispersion in the matrix. One study reported improvement of the dispersion by melt mixing solvent-casted MWNT/PMMA films, after several steps of melting and drying as evidenced by optical micrographs; even after 20 melting cycles still some particles existed [20]. Other studies have suggested functionalization of carbon nanotubes with nitric, sulfuric acid or hydrofluoric acid introduces functional groups such as carboxyl, hydroxyl or carbonyl on the sidewall of CNTs which in turn improve the interaction between CNTs and different polymers [20-22]. Another approach is in-situ polymerization of polymers with CNTs [22-25]. In this process the monomers and CNTs are added to the solvent along with initiators. The initiator can open π-bonds of the CNTs, hence chemically connecting the CNTs with polymer chains. These studies generally rely on TEM, SEM, rheological and optical measurements to conclude better dispersion. This technique is particularly effective for the preparation of thermally unstable and insoluble polymers, which cannot be processed by melt or solution processing. While in-situ polymerization of polymers with SWNTs leads to a better dispersion, this does not mean the nanotubes have been completely individualized. Though generally the tensile properties improve with this method due to improved dispersion and adhesion, but reduction in tensile properties has been reported. Lower tensile properties has been reported for Poly(ether ketone) polymerized in-situ with

FWNTs, which has been attributed to lower molecular weight when polymerization is carried out in the presence of nanotubes [26].

1.2.2 Theoretical Approach to Aggregation

A SWNT can be considered as a rolled up graphene layer. The specific surface area can be easily calculated by considering a single hexagon unit. The side length of this hexagon corresponds to the average carbon-carbon bond length which is 0.142 nm. This single unit has six carbons at each vertex, where each carbon is shared between three hexagons. The mass of a single carbon atom, 1.994×10^{-23} g, can be obtained by dividing the atomic weight by the Avogadro number. The specific surface area, SSA, of a hexagon is obtained by dividing the surface area of a single hexagon by the mass of two carbon atoms; which results in the value S=1313 m^2/g [27]. For MWNTs the specific surface area is lower and depends on the number of walls; the inner wall surface areas are not accessible. Therefore while the inner walls contribute to the mass, they do not contribute to the SSA which is expressed in eq. (1-1).

$$SSA_n = \frac{\pi l(d_i + 2(n-1)d_{ss})}{\pi l(nd_i + n(n-1)d_{ss})} 1313 \qquad (1\text{-}1)$$

where n is the number of walls, d_i is the inner diameter, d_{ss} =0.34 nm is the shell to shell distance. The SSA of individual MWNT as a function of number of walls is shown in Figure 1-4.

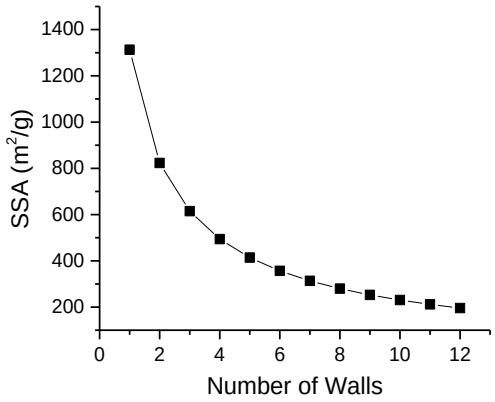

Figure 1-4. Specific surface area of nanotubes as a function of number of walls for CNTs with inner diameter d_i=1.

For the purpose of calculating bundle size the bundle is approximated as a hexagonal bundle as shown in Figure 1-5, whereas only the outer CNT surfaces are available, n_b, the total number of CNTs in a perfect bundle with *N* layers, follows the relation $n_b = 3N^2 - 3N + 1$ and the number of exposed CNTs which their surface are available is $n_e = 3N - 2$. The fraction of the exposed CNTs to the total CNTs follows the ratio:

$$f_N = \frac{n_e}{n_b} = \frac{3N - 2}{3N^2 - 3N + 1} \qquad (1\text{-}2)$$

Using this equation one can easily obtain the accessible surface area and hence the SSA of a bundle of SWNTs or MWNTs is $SSA_b = SSA_n \cdot f_N$. The size of the bundle, d_b, is calculated according to eq. (1-3), where d_o is the outer diameter of the nanotube. The influence of bundling on reduction of SSA is shown in Figure 1-6.

$$d_b = {n_b}^{0.5}(d_o + d_{ss}) \qquad (1\text{-}3)$$

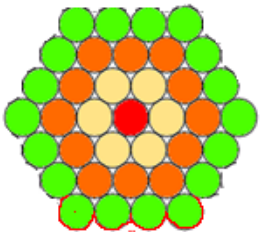

Figure 1-5. Bundling of CNTs limit accessible surface area (four layers in this case N=4).

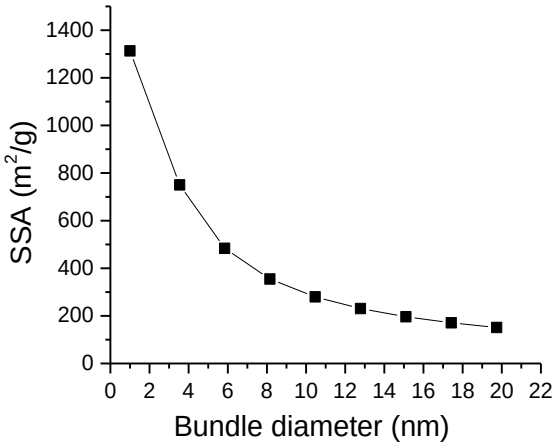

Figure 1-6. Specific surface area as a function of bundle diameter for SWNTs with d_i=1 nm.

A few examples of experimental CNT surface area in previous studies is shown in Table 1-1. The materials are in powder or buckypaper form. Bacsa et al. [28] prepared individual CNTs with high surface area and compared the calculated surface area to the measured surface area. Their CNTs which were predominantly single and double walled had an experimental specific surface area of 948 m^2/g while their calculations predicted 900-1000 m^2/g. Hernandi et al. [29] used zeolite support to synthesize their buckypaper and removed the zeolite for SSA analysis. In another study, single walled carbon nanohorns (SWNH) were sonicated with SWNT to obtain such high SSA, 1430

m2/g[30]. The majority of this increase in surface area was due to opening of SWNH. In another work, an as-grown SWNT forest displayed a specific surface area of 1000 m^2/g, but the density was very low, 0.029 g/cm^3 [31]. After densification of the SWNT forest with a liquid such as water or alcohol, the density increased to 0.57 g/cm^3 while the SSA remained unchanged.

Table 1-1. BET SSA of CNT samples from literature.

Type of CNT	SSA (m^2/g)	Comments
SWNT/DWNT [28]	948	Powder
SWNT [29]	653	Buckypaper
SWNT-SWNH [30]	1430	nanocomposite
SWNT [30]	470	Buckypaper
SWNT [32]	642	Buckypaper
SWNT [31]	1000	Densified forest

1.2.3 Polymer Wrapping Around CNTs

There have been many reports on the polymer wrapping of carbon nanotubes over the last two decades [33-37]. In some studies, microscopic techniques (AFM, SEM, TEM) have been used to show polymer wrapping on carbon nanotubes (CNT) [22, 37-40] while in other studies spectroscopic methods such as photoluminescence [33, 35], UV-Vis and Raman spectroscopies [36] demonstrate selective interaction between the polymer and certain chiralities. The polymers that have been shown to wrap on carbon nanotubes include 9,9-dioctylfluorene derivatives [33], polyvinyl pyrrolidone, polystyrene sulfonate [38], DNA [41, 42], polybenzimidazole (PBI) [43], aromatic polyimide[44], poly[(m-phenylenevinylene)-alt-(p-phenylenevinylene)] (PmPV) [45].

Helical wrapping of polymers has been suggested as early as 1998 [37]. In this study, by polymerizing poly(phenylacetylenes) (PPA) in the presence of MWNT, they concluded helical wrapping of polymer around the nanotubes from TEM (Figure 1-7a). While the TEM does show some coating, there is no evidence of helical wrapping. The XRD data (Figure 1-7b) shows PPA in the structure, but in no way does it prove that the polymer is wrapping the CNTs, let alone a helical morphology. From XRD, PPA signature in the PPA/SWNT samples is similar to that of pure PPA, suggesting similar morphology. Since the polymerization is carried out with the nanotubes, it is expected that the nanotubes participate in the polymerization and the PPA would cling on the sidewalls.

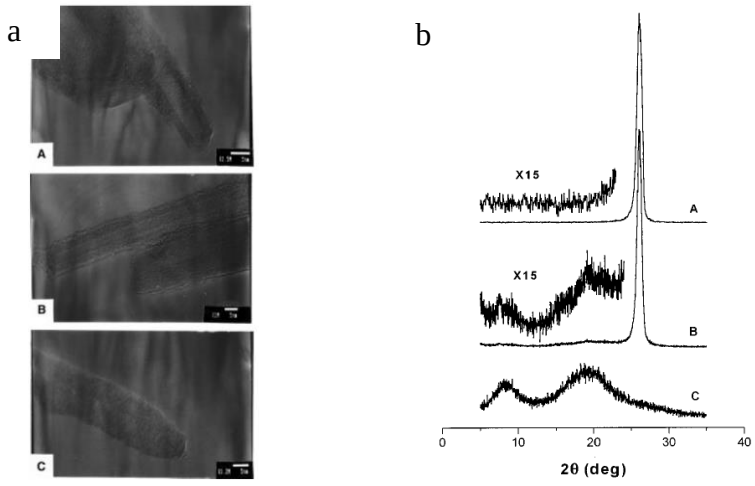

Figure 1-7. PPA/MWNT. a) TEM micrograph of PPA chains around nanotube shells. (scale bar 5 nm). b) X-ray diffraction patterns of (A) nanotubes, (B) PPA-wrapped nanotubes, and (C) PPA. Diffratograms were recorded on a powder diffractometer. Note the similar peaks for PPA in B and C, indicating the same morphology with and without MWNTs [37].

O'Connell et al. suggested helical wrapping of CNTs with polyvinyl pyrrolidone (PVP) and polystyrene sulfonate (PSS) based on a thermodynamical approach [38]. They consider the favorable interaction of individualized SWNT/polymer over, SWNT/water is the main drive behind polymer wrapping. Based on AFM measurements (Figure 1-8a) they determined that the monolayer is covering the surface uniformly with a monolayer of polymer. Based on their observations they suggest a helical wrapping of polymer around the nanotube (Figure 1-8b). While there are some smaller bundles and the heights seem to be uniform (the height data is not provided). (But from the lateral dimensions, I obtained a size of 11 nm, which seems to be more than a monolayer of polymer. Considering a 1 nm nanotube, the thickness seems to be too much). It is difficult to discern bundled nanotubes from polymer coated nanotubes, or even polymer coated bundles.

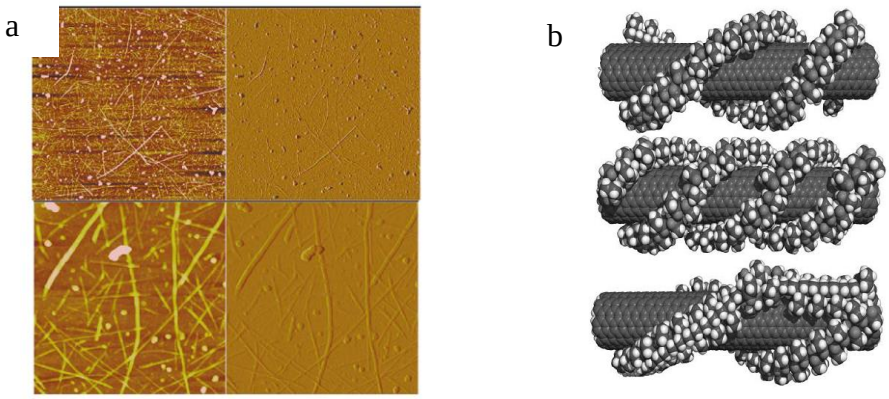

Figure 1-8. PVP/SWNT. a) AFM images of PVP–SWNTs on a functionalized substrate. 5 μm height image (top left) and amplitude image (top right). 1 μm expanded height image (bottom left) and amplitude image (bottom right). b) Schematics of some possible wrapping arrangements of PVP on an (8,8) SWNT. A double helix (top) and a triple helix (middle). [38].

Another study relied on TEM to determine helical wrapping of the polymer which was used in their studies [40]. From the TEM images (Figure 1-9) it seems that small polymer sections have helical arrangements, but the wrapping goes clockwise and counter clockwise along the tube and does not arrange as an ordered helix. The computational molecular dynamics initializes with the helical wrapping and evolves into disordered wrapping. While polymer wrapping is observable from TEM, this could be true for some tubes which have been individualized, due to the localized nature of TEM imaging. The polymer wraps the nanotubes with a large pitch due to very rigid nature of the polymer that was used in this study.

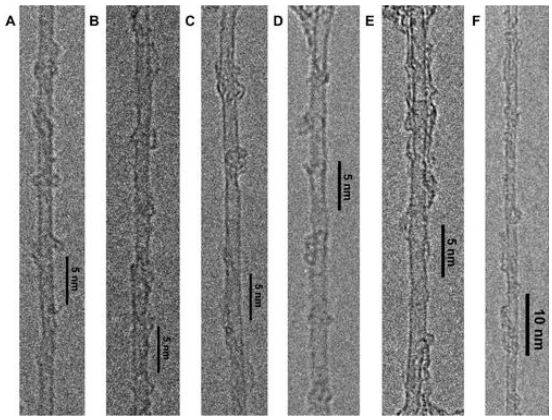

Figure 1-9. TEM images highlighting expected left-handed helical structures formed by S-PBN(b)-Ph4PhCN-wrapped (A–C) and S-PBN(b)-Ph2PZn2-wrapped (D–F) [PLV SWNTs] (d = ~1.4 nm) from corresponding aqueous suspensions [40].

Polymer wrapping of SWNTs has been shown to be effective for separating semiconducting nanotubes from metallic nanotubes. One of the earliest reports of polymer assisted separation is related to DNA wrapping of HiPco SWNTs[41, 42]. They argued that the DNA phosphate group provides a negative charge density on the surface

of the carbon nanotube, the distribution of which should be a function of the DNA sequence and electronic property of the nanotube. DNA-metallic CNT is expected to have less surface charge due to the opposite image charge created in the metallic tube, than DNA-semiconducting CNT. Ion-exchange liquid chromatography was used to exploit this difference in surface charge. After preparing the DNA/SWNT suspension, ion-exchange chromatography was carried out and the suspensions were separated based on elution time. Separated parts of the suspension displayed different absorption peaks for the metallic and semiconducting peaks, with early fractions displaying higher absorption at smaller wavelengths (400-600 nm) characteristic of metallic tubes while later fraction had a higher absorption at higher wavelengths. Complete removal of the DNA wrapping after the sorting has not been reported. Selective CNT interaction has been studied for other polymers as well, which generally involve conjugated polymers[33, 35, 40, 45-47], due to the π-stacking interaction between the polymers and SWNTs. Although chiral selectivity has been studied extensively, there has been no success in separating SWNTs from MWNTs and while selectivity and interaction has been demonstrated, the only evidence pertaining to wrapping has been AFM and TEM, which are local methods.

While these experimental studies report polymer wrapping on SWNT and/or MWNT, they do not provide evidence of ordered polymer wrapping. The only evidence which pertains to ordered polymer wrapping on carbon nanotubes (to-date) comes from computational studies [39-41, 45]. There are many studies on PMMA/CNT system [20-22, 48-50]. However, evidence of PMMA wrapping on CNTs has never been reported. The only account of ordered helical wrapping is of wrapping of syndiotactic PMMA

around C_{60} (Figure 1-10) [51]. X-ray diffraction showed an ordered structure of st-PMMA around the buckyballs. The helical pitch of PMMA was ~0.9 nm, with the possibility to incorporate larger buckyballs, C_{70} and C_{84} with slight alteration of the helical pitch. Syndiotactic PMMA has also been shown to crystallize using solvent-induced crystallization with a helical pitch of 0.885 nm. But there has been no report of atactic PMMA crystallization or helical wrapping.

Figure 1-10. schematic of C_{60} encapsulated by helical PMMA [51].

1.3 Electrochemical Capacitors

Energy storage has become crucial part of everyday life. With portable electronics finding their way into our lives more and more every day, the need for portable energy storage devices is sharply increasing. Batteries power devices, such as cell phones, laptops and tablets, throughout the day, and while they have high energy density it takes some time for them to recharge. In other situations, such as starting large machinery or regenerative braking, batteries cannot respond to the large charge/discharge rates. For rapid energy delivery and recharging, electrochemical capacitors or supercapacitors are used. Various types of energy storage devices are compared according to their energy and

power density in Figure 1-11. Batteries and supercapacitors rely on different electrochemical processes to store energy. Redox reactions power batteries and limit the power density. Energy storage in supercapacitors is based on the adsorption of electrolyte ions on the surface area of electrically conductive porous electrodes, usually porous carbons. Energy is stored by separation of charge in the double layer at the surface of the conductive electrode as shown in Figure 1-12, hence why they are also known as electric double layer capacitors (EDLC).

Many applications require rapid storage and release of energy for high power applications. While conventional batteries will suffice to start a car, for heavy machinery higher power is required to start it. Also in emergency situations, for instance opening aircraft doors quickly and ejection, a high surge of power is required. Supercapacitors are devices suited for such applications which are able to provide quick bursts of energy in short durations, where the capacitance arises from the charge separation at an electrode-electrolyte interface. The key advantages of EDLCs over batteries include lower internal resistance, higher power density, broader temperature window of a stable operation, rapid charging, and significantly longer life cycle. EDLCs are consisted of two high surface area porous conductive electrodes immersed into electrolyte and separated by an electron-insulating and ion-conducting separator membrane. When a voltage is applied across these electrodes the electrolyte ions of the opposite sign accumulate on the surface of each electrode. When the two electrodes are similar the cell is symmetric cell. For asymmetric electrochemical capacitors different types of materials are used for the positive and negative electrodes. Usually, in asymmetric cells one of the porous carbon electrodes is replaced with a material used in batteries with high faradaic ion storage

capability. Since the charge is confined to the surface, energy density of EDLCs is limited by the surface area and are much less than batteries. In order the increase the energy storage of EDLCs another mechanism was studied which involved redox reactions at the surface of the electrodes, known as pseudocapacitance. Certain materials result in pseudocapacitance in the electrode structure such as metal oxides, namely ruthenium oxide, vanadium oxide, manganese oxide, etc, and functional groups in carbon materials. Pseudocapacitive materials enable high power energy storage devices with energy density comparable to batteries.

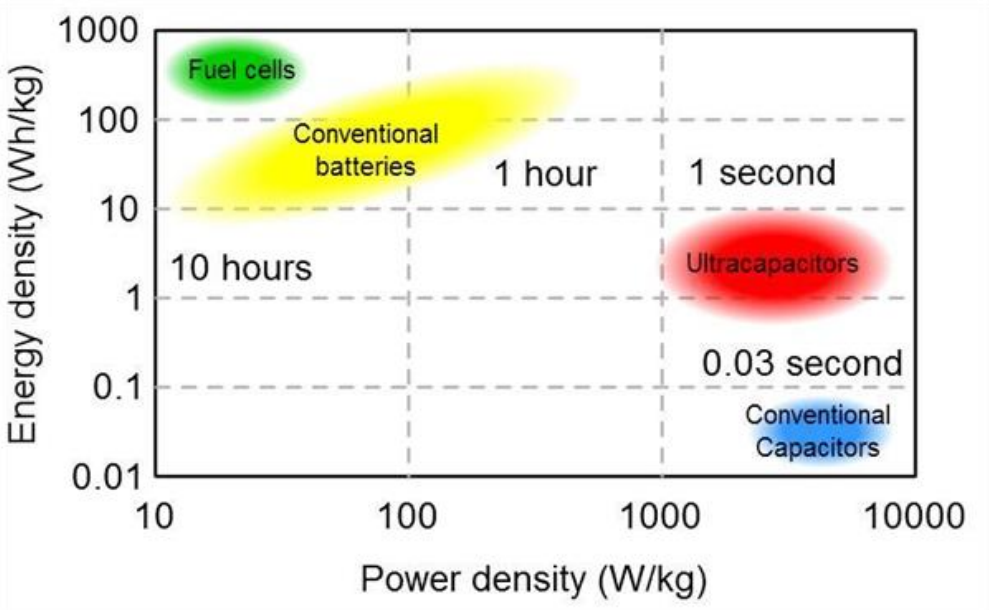

Figure 1-11. Comparison of energy and power density of different energy storage devices [52].

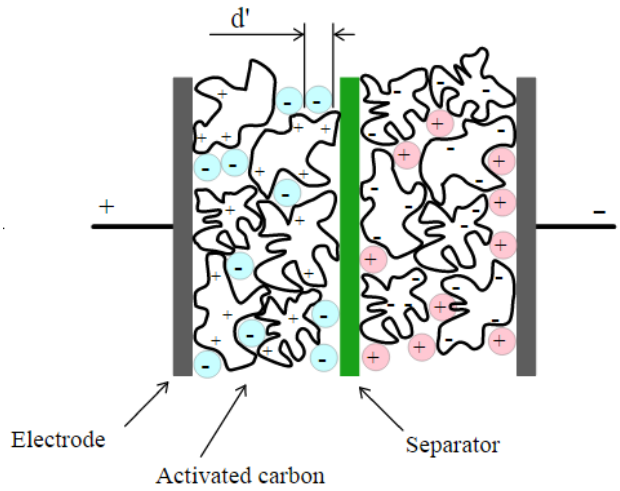

Figure 1-12. Schematic of EDLC, showing charge storage on each electrode at the electrode-electrolyte interface.

1.3.1 Electrodes

Carbon based materials in a variety of dimensions, including activated carbon[53-55], graphene [56-58] and CNTs [59, 60], and forms, such as powders [61], gels [62-64], and composite[65-67], have been commercially and scientifically utilized for energy storage applications. Activated carbon, due to its low cost, porous structure and high specific surface area (SSA), is widely used in commercial supercapacitors. Although some studies suggest that capacitance increases with surface area [62], other studies on activated carbon have shown that higher SSA results in improved EDL (electrical double layer) capacitance at low discharge current, however at high discharge currents larger pores play an important role, making them more suitable for high power applications [68, 69]. Others have attributed the limitation of charge storage at higher SSA to space constriction for charge accommodation inside the pore walls [70]. There has not been a

study which investigates the effect of SSA on CNTs without inducing defects, opening them and adding functional groups.

Other forms of carbon such as CNTs and graphene also display high conductivity, porous structure and high surface area making them suitable candidate for EDLCs. Both of these materials suffer from aggregation and agglomeration and different techniques have been used to increase their performance. Hybrid structures of SWNT and graphene have been proposed to overcome aggregation and increase SSA and alter the pore size and structure to facilitate ion movement and storage[71-74]. Adding functional groups to these carbon based materials by means of oxidation also leads to increased capacitance due to contributions from pseudocapacitance [75, 76]. Acid treatment, KOH activation and plasma treatment have been used to increase SSA by inducing defects and opening CNT tips [55, 77-80]. A method to produce aligned SWNTs with SSA of 1000 m^2/g was proposed by Futaba et. al. [31], leading to a specific capacitance of 80 F/g at 1 mV/s.

Due to its high conductivity and nanostructure, CNTs have been used as a platform for other materials. As mentioned previously, some metal oxides have the potential to compete with Li-ion batteries but at higher power rates. The porous structure of carbon nanotubes can be used as the backbone network and by depositing thin layers of metal oxides, high energy density can be achieved. Atomic layer deposition (ALD) of vanadium oxide on MWNT resulted in very high capacitance, 600 F/g at a current density of 1 A/g with capacitance retention of 92% after 5000 cycles [81]. Upon increasing the ALD cycles from 100 to 500 cycles the thickness of the coating increases leading to the decrease of capacitance. Increased thickness lowered the capacitance since only the top surface was redox active, the increased thickness limited electrolyte ion access and the

vanadium oxide was electrically insulating, hindering electron transport. Pham et al. reported a hybrid CNT/graphene oxide system which displayed high energy storage. They created an activated SWNT/graphene 3D network (Figure 1-13) using electrostatic self-assembly and KOH activation [73]. The activation provided functional groups such as carboxylic acid, epoxy and hydroxyl which contributed to its high energy density and the porous network provided efficient ion diffusion for high power.

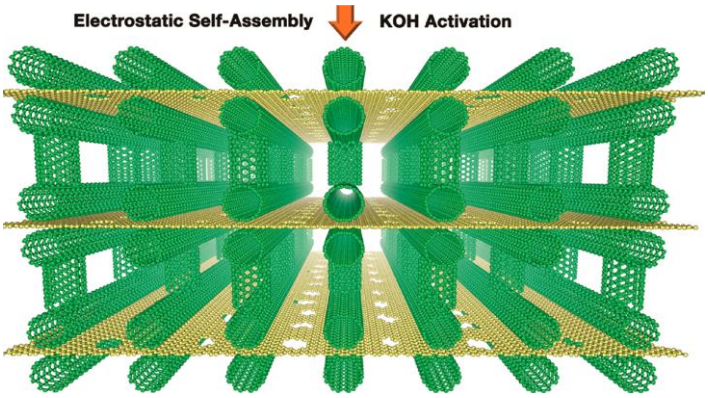

Figure 1-13. Schematic 3D block of activated SWNT/graphene [73].

Reporting capacitance is helpful when comparing cells with various electrolytes operating at different potential ranges. One should practice care when comparing values of capacitance and energy storage from the literature. This is due to the fact that there is no widespread approach to reporting these values. Capacitance, which is the slope of potential(x)-charge(y) plot, will depend on what potential or potential range was used to calculate it. Some studies use the specific capacitance of a single electrode and use that as a basis for calculating the energy density [31]; while this is completely unnecessary since the energy density and power density should be calculated using the stored charge and

voltage. This is especially crucial since determining capacitance has been rather arbitrary throughout the literature.

1.3.2 Electrolytes

The choice of electrolyte plays an important role in the performance of EDLCs. The potential window is the most important factor and has a large influence on the energy density. Aqueous electrolytes consist of aqueous solutions of strong bases, such as potassium hydroxide, acids, such as sulfuric acid or salts, such as sodium chloride, have an operating potential window of 1V. Above this threshold electrolysis of water takes place and the electrolyte deteriorates resulting in loss of performance. Due to the strong ionic bond, common salts tend to melt at a higher temperature compared to other solid molecules. Ionic liquids (IL) on the other hand are salts with a melting point below 100° C. The main advantage of these ionic liquids is their larger electrochemical potential window, ~3V. According to the energy density eq., $E = \frac{1}{2}CV^2$, this means that the energy density of a cell with ionic liquid is 9 times higher than that of a cell with aqueous electrolyte. However the energy density does not scale necessarily as such. The size of the IL ions are ~2 times larger than KOH ions [82]. This means that some pores which are accessible to the smaller ions are not available to the IL ions. Also aqueous electrolyte ions generally diffuse quicker resulting in better response at higher powers. The of IL ions can be improved by dissolving in non-aqueous solvents such as acetonitrile and ethylene carbonate [83].

1.4 Mechanical Reinforcement by CNTs

There are several requirements for efficient mechanical reinforcement of CNTs in polymers. These include good CNT dispersion, interfacial stress transfer, and large aspect ratio [84]. CNT dispersion is an important factor to maximize the effectiveness of the fillers. Uniform dispersion of isolated nanotubes which are coated by the polymer is necessary since nanotube bundles can slip by each other. However, a good dispersion is not enough for load transfer. If the interaction between the polymer and the nanotubes are not strong enough, upon applying loads the polymer chains will just slip past the CNTs, not only rendering them ineffective, but they become detrimental and areas for stress concentration. Hence efficient load transfer to the nanotubes is the most important requirement for composites for mechanical properties. The stress transferred to the nanotube is proportional to the shear stress at the polymer-CNT interface. As the composite is further strained, at some applied stress, known as the interfacial shear stress, the interface will fail and no additional stress is transferred to the nanotubes. The last requirement for improved load transfer to the nanotubes is a large aspect ratio [85-87].

The influence of CNTs for mechanical reinforcement has been studied for many polymers and studied extensively as evidenced by the sheer amount of literature [88-100]. While the impact of adding nanotubes vary from one study to another based on the type of polymers, type and purity of the nanotubes, sample preparation and fabrication, and testing methods, the general trend is similar in that a small addition of nanotubes increases the modulus, however, at higher loadings the reinforcement diminishes and may even deteriorate upon adding more nanotubes due to worsening the dispersion and nanotube aggregation. Chang et al. reported a threefold increase in modulus of drawn

polypropylene/SWNT fibers upon addition of 1 wt% SWNTs however upon further increase of SWNT concentration up to 5 wt% the modulus increased 45% [101]. Another work on polypropylene/SWNT fiber reported a 55% increase in modulus with 1 wt% SWNT [102]. The difference may be due to the processing conditions or the nanotubes; the nanotube purity is 70% while the purity was not reported by Chang et al. Velasco-Santos et al., polymerized PMMA in the presence of arc-MWNTs, where the stiffness was increased from 1.5 to 2.5 GPa by addition of 1 wt% MWNTs [103]. Some studies have shown the importance of the quality of CNT dispersion in the matrix [104], while other studies have emphasized the importance of the interaction between the CNT and matrix to ensure favorable load transfer. In another study on PMMA/CNT composites, PMMA was reinforced by the addition of PMMA grafted arc-MWNTs [92], where the modulus increased from 2.9 to 29 GPa on addition of 20 wt% nanotubes, suggesting . The nanotubes failed by the "sword and sheath" method suggesting strong adhesion between the nanotubes and the matrix. It seems intuitive that the CNTs would be well dispersed if there is a good interaction between the CNTs and the dispersant media [10].

1.4.1 Micromechanical Model for Prediction of Elastic Modulus

Mechanical reinforcement of polymers by CNTs has been modeled by computational methods such as molecular dynamics [105-109], computational mechanics methods such as micromechanics [110-113] and multi-scale methods that combine both of these modeling approaches [114-116]. Another approach which requires less preparation compared to computational methods is micromechanics models, such as the modified Halpin-Tsai model [117] and the Cox model [86]. Some of these models will be discussed in detail and used for comparison with the experiments.

1.5 Stress Transfer from Polymer Matrix to CNT

Stress transfer from the matrix to the CNTs occurs due to shear stresses at the matrix-CNT interface due to differences in axial elastic displacements while the composite is under strain. Different methods of calculating the interfacial shear strength of polymer/CNT composites include CNT nano-pullout tests [118-121], molecular dynamics simulations [108, 122, 123], and Raman spectroscopy [124, 125]. In addition to requiring a substantial amount of sample preparation for CNT pull out test, other factors influence the results such as yielding leading to large variations during the pull-out test. Although molecular modeling does not require as much preparation when the model is set up, however, the results are directly influenced by the input parameters. Usually simulations are compared with experiments to verify their accuracy. On the other hand, Raman spectroscopy can be easily used to monitor CNT stress and strain, and requires minimal preparation.

1.5.1 Monitoring Stress Transfer Using Raman Spectroscopy

Stress-induced Raman band shifts have been monitored in carbon fiber [126], individual SWNTs [127] and SWNT bundles [128]. SWNTs exhibit Raman active modes, which present themselves in four areas of the spectra; the radial breathing mode (RBM), disorder induced mode (D), graphitic mode (G), and the overtone of the D mode (G') (Figure 1-14). The *D*, *G* and *G'* modes depend on the C-C bonds in the SWNTs. The stretching of these bonds, results in their weakening and down-shifting of their frequencies[129]. That is why these modes are used to monitor stress-induced shifts. This has been done by straining individual CNTs using AFM and monitoring the spectra using

micro-Raman spectroscopy [127], where the *D*, *G*, and *G'* Raman modes are downshifted up to 27, 15 and 40 cm^{-1}, respectively, at a strain of 1.65%. The highest value reported for the *G* band shift is 157 cm^{-1} for ultralong SWNTs at a strain of 6.2% and they achieved a maximum strain of 13.2% where the G band shift was 86 cm^{-1} [130].

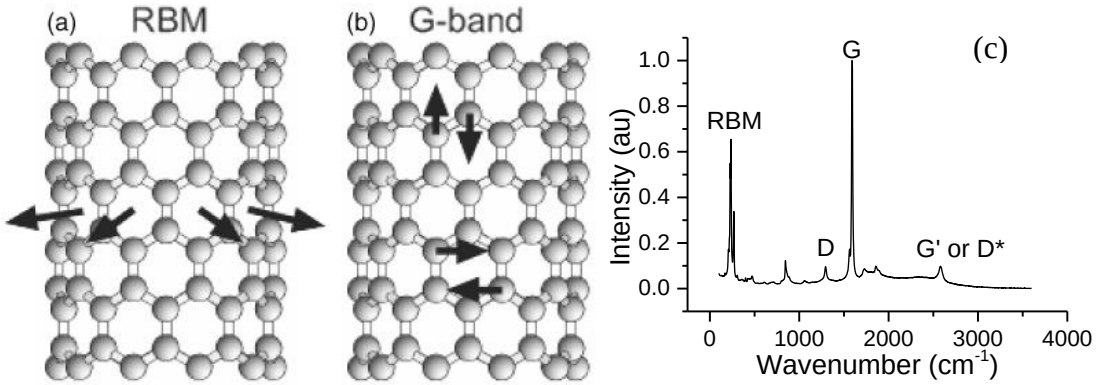

Figure 1-14. Raman spectroscopy of CNTs. a) Vibration of carbons in SWNTs resulting in RBM. b) Planar vibration along the CNT axis (G^+) and vibration in the circumferential direction (G^-) constitute the G-band. c) Raman spectra of SWNTs normalized to the G band with the different bands labeled.

As the composite is strained some of the stress is transferred from the matrix to the nanotubes. By monitoring the downshift of the Raman bands the strain on the nanotubes can be obtained and the interaction between the two components and the effectiveness of the load transfer to the nanotubes can be studied. The failure of the interface can be easily identified by monitoring the Raman shift behavior, indicated by plateauing of the Raman band shift upon further straining the composite. This effectively shows that while the composite is being strained no further strain is applied on the nanotube and that the polymer chains are slipping past the nanotubes.

1.6 Polyacrylonitrile Fibers

Polyacrylonitrile (PAN) was first synthesized in the 1930s, but it was not until the 1950s that it was commercialized for use as textile fibers by Dupont. The molecular weight of PAN can vary from ~10,000 to several millions g/mol. Various spinning methods can be used to produce PAN fibers, such as wet spinning, dry-jet-wet spinning, gel spinning, and melt spinning. Dry-jet-wet and gel spinning can produce highly drawn fibers with the low number of micro-voids throughout the fiber. For melt spinning, PAN polymer needs to be pretreated with plasticizer due to its high melting temperature, which is higher than its degradation temperature.

1.6.1 Polyacrylonitrile Based Carbon Fibers

PAN is the most common carbon fiber precursor, accounting for more than 90 percent of all carbon fiber production [131]. PAN based carbon fibers are widely used in composites due to their high tensile strength. Carbon fibers from PAN precursor is produced by stabilization (200-300 °C) and carbonization (+1000 °C). Stabilization and carbonization can be carried out in batch and continuous process. While, batch processing may provide flexibility to analyze different testing parameters, because of the nature of batch processing it is prone to unavoidable variations mainly arising from sample preparation. There are multiple variables during stabilization and carbonization which can affect the resulting carbon fiber structure, such as temperature ramp rate, stabilization temperature and residence time, and carbonization temperature and residence time.

Small diameter PAN/CNT fibers have been shown to have better mechanical properties compared to PAN fibers [132]. CNTs have been shown to template the

graphitic structure of carbon fiber [133] which could be lead to improved mechanical properties. However, it has been also demonstrated that as the CNTs bundle the templating effect is diminished. Reinforcement of poly(methyl methacrylate) (PMMA) composite films with carbon nanotubes (CNTs) was discussed in detail in the previous chapter. In this chapter, the effect of PMMA wrapping on SWNTs on the structure and properties of polyacrylonitrile precursor and carbon fibers will be studied and discussed.

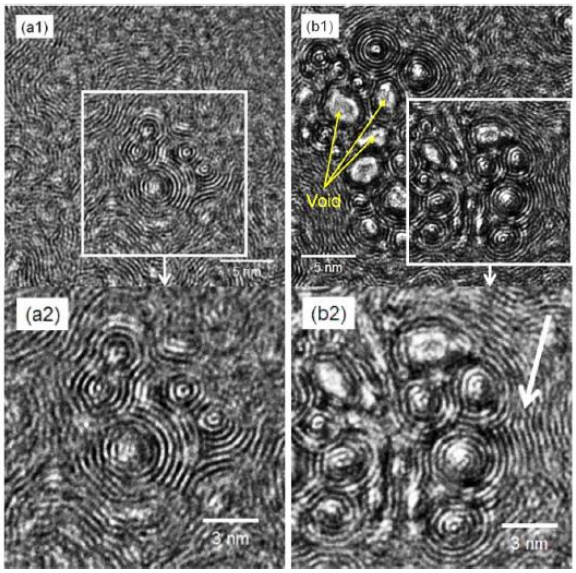

Figure 1-15. High resolution TEM image of PAN/CNT fibers. The arrow in (b2), shows evidence of graphitic templating and epitaxial growth at the surface of CNTs [133].

1.7 Objectives

The objectives of this study are:

1. To study the interaction between poly (methyl methacrylate) (PMMA) and single wall carbon nanotubes (SWNT).

2. To process high surface area carbon nanotube electrodes for electrochemical supercapacitors with the goal of improving the energy storage performance of CNT electrodes.
3. To study the effect of poly (methyl methacrylate) wrapping on single wall carbon nanotubes on the mechanical, thermomechanical, and electrical properties of PMMA/SWNT films.
4. To study the effect of poly (methyl methacrylate) wrapping on SWNTs on the structure and mechanical properties of polyacrylonitrile (PAN)/SWNT precursor fibers and carbon fibers.

CHAPTER 2

POLYMER ASSISTED DISPERSION

2.1 Introduction

As mentioned in the first chapter, the main key to efficient use of carbon nanotubes (CNTs) is a well dispersed system of nanotubes, as shown in Figure 2-1a. In composites, aggregation of carbon nanotubes (Figure 2-1b) leads to an inhomogeneous distribution of nanotubes in the matrix. Due to a mismatch in modulus of regions with different nanotube concentration, the PMMA rich regions will experience much higher stress, coupled with lower strength of the PMMA, severe aggregation may deteriorate the mechanical properties. Well dispersed individualized nanotube dispersion as shown in Figure 2-1a will provide the best mechanical reinforcement and maximize functional properties, such as electrical and thermal conductivity, of the composite. CNTs entangle in buckypapers, which provides it with modest mechanical stability. If the accessible surface area is favorable, bundling (Figure 2-1c) can limit the available surface area and the entangled state in Figure 2-1b is preferred. But the question is: how can we tailor the dispersion of CNTs in composites to maximize the benefits of these fillers?

Figure 2-1. Nanotubes in different aggregation states (a) individual and well dispersed, (b) individual but entangled, (c) bundled.

2.2 Experimental

2.2.1 Materials

HiPCO^{TM} single wall carbon nanotubes (SWNTs) (grade SP0300, average diameter 0.9 nm, purity 98%) and few wall carbon nanotubes (FWNTs) (grade XOC231U, average diameter 2.7 nm, mainly two and three walled, purity 98.8%) from Carbon Nanotechnologies, Inc., and multi wall carbon nanotubes (MWNTs) (average diameter 25 nm, purity 95 %) from Cheaptubes Inc were used. Dimethylformamide (DMF, ACS grade, 99.8% purity) and poly(methyl methacrylate) (PMMA) (M_w= 8,000, 350,000, and 996,000) was obtained from Sigma Aldrich. PTFE membranes (Zefon International, FPTPT147) with 1 μm and 5 μm pore size were used for the filtration.

2.2.2 Buckypaper Processing

A suspension containing 8 mg CNT in 600 mL DMF was homogenized (IKA ULTRA-TURRAX T18) for 30 minutes and then 80 mg PMMA (dissolved in 40 mL DMF) was added to this CNT/DMF suspension. The sonication concentration and PMMA content can vary based on the experiment. For all molecular weights used in this

study, the PMMA concentration in the suspension is well below the critical overlap concentration. After vigorous shaking, this PMMA/CNT/DMF suspension was sonicated for 24 hours (Branson 3510R-MT, 100 W, 42 kHz). Then the suspension was filtered using the PTFE membrane and washed with methanol to remove DMF. The SWNTs were filtered using the 1 μm membrane, while the FWNTs and MWNTs were filtered using 5 μm. The produced PMMA/CNT buckypaper was peeled from the PTFE membrane and dried in vacuum oven at 70 °C for 3 days. These buckypapers are referred to as "as produced" buckypaper. PMMA that is interacting with the CNTs, as well as the PMMA that is entangled or trapped, will remain in the buckypaper, and the rest of the PMMA will be filtered out. To analyze the weight of the buckypaper, thermo gravimetric analysis (TGA) was done in nitrogen at a heating rate of 10 °C/min. The TGA study shows that PMMA was removed from the PMMA/CNT buckypapers by heat treatment at 400 °C. Control buckypapers (without the use of PMMA) from different CNTs were also made for comparison using the above.

2.2.3 Composite Processing

PMMA was dissolved in DMF at a concentration of 150 mg per 10 mL, and the solution was dry cast in a glass mold. For CNT composites, CNTs were sonicated in 10 mL of DMF for 24 hours and the polymer powder was added to the solvent and stirred for 24 hours and poured into the mold. For PMMA wrapped SWNTs, SWNT and PMMA (1:1 weight ratio of SWNT:PMMA) were sonicated in 10 mL of DMF. Then polymer powder was added and stirred for 24 hours and dry cast.

2.2.4 Characterization

Wide-angle X-ray diffraction (WAXD) data were obtained in transmission mode on a Rigaku Micromax-002 (λ=0.15418 nm) system. Raman spectra were obtained using a 785 nm laser on a HORIBA XploRA Raman Microscope System. UV-vis spectra were obtained on Perkin Elmer Lambda 35 instrument. BET surface area measurements were made with Micromeritics ASAP 2020. MATLAB was used to generate initial PMMA coordinates and Chembio3D was used for energy minimization. After energy minimization the atom coordinates were used to simulate the diffraction pattern using Debyer [134].

2.3 Results and Discussions

2.3.1 Polymer Wrapping Model

In the first chapter, previous attempts to wrap CNTs with polymers were discussed. While some rigid polymers were shown to interact with CNTs no evidence of improvement of dispersion was provided. Other methods such as CNT functionalization and in-situ polymerization improve the interaction between CNTs and solvent or matrix material at the cost of altering the mechanical and electronic properties of the nanotubes and may not be very effective. The use of surfactants may not be possible in some cases, such as incompatibility with other components and can negatively impact desirable properties, e.g. mechanical properties. Also a high quantity of surfactants is usually required to achieve a good dispersion in a solvent. For these reasons an approach is required which prevents bundling and aggregation of nanotubes in the solvent and

different polymer matrices, at low weight percent. In the next step, we will study possible polymers which may wrap CNTs.

Molecular dynamics was used to identify polymers which may wrap CNTs. ChemBio 3D was used to carry out simulations. Short polymer chains (3-6 monomers) were initialized in trans configuration and allowed to relax to reach a minimum energy state and the bond angles of the backbone were measured. In a head-to-tail configuration, which is usually the case, the bond angle of the backbone carbon with the pendant group is smaller than the CH_2 due to the steric hindrance from the large side group. The difference between the bond angles determines the curvature and ultimately the diameter of the helix the polymer makes. Poly (methyl methacrylate) (PMMA) and polyacrylonitrile (PAN) are used demonstrate the effect of side groups on the bond angles of the polymer backbone (Figure 2-2). The subsequent bond angles are ~107 and 124° for PMMA and ~111 and 115° for PAN. The slight variation of the bond angles from one carbon to the other is due to the tacticity of the polymers. The difference between bond angles, ~17° for PMMA and ~4° for PAN, can be used to determine the approximate number of monomers to form one complete helix turn by dividing 360° degrees (one complete turn) by the bond angle difference. This results in ~21 monomers and ~90 monomers for PMMA and PAN respectively. A complete helix turn for each polymer is shown in Figure 2-3. The diameter of the PMMA helix is ~1.6 nm and PAN helix is ~6 nm. Considering a van der Waals distance of 0.3 nm, a ~1 nm CNT could fit inside the PMMA chain and ~5.4 nm CNT inside the PAN chain. The helical polymer can accommodate CNTs with diameters within close range of the target diameter by minor change in bond angles and dihedral angles. However, the polymer chain may not

necessarily form such a helical conformation. This can be due to more favorable morphologies, for example crystallization of PAN may lead to lower energy than the helical state, or that the side chain-solvent interaction may not be favorable for a helix to be formed. Another factor is the stability of the polymer chain in all-trans configuration. If both hydrogens are substituted, the polymer chain is more likely to remain in trans state, as is the case of PMMA. But for PAN which has one hydrogen atom substituted with the nitrile group, it has a strong tendency to flip into gauche, due to lower steric hindrance. After verifying possible candidates, experimentation is required to determine if the polymer wraps the CNTs.

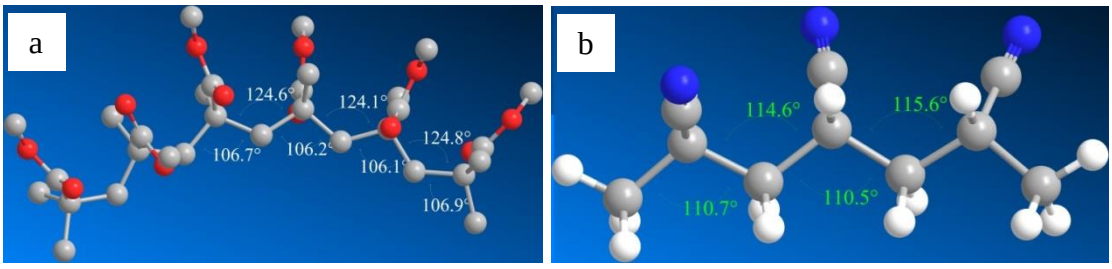

Figure 2-2. Bond angles of two polymers in trans state after energy minimization: (a) atactic PMMA, (b) atactic PAN.

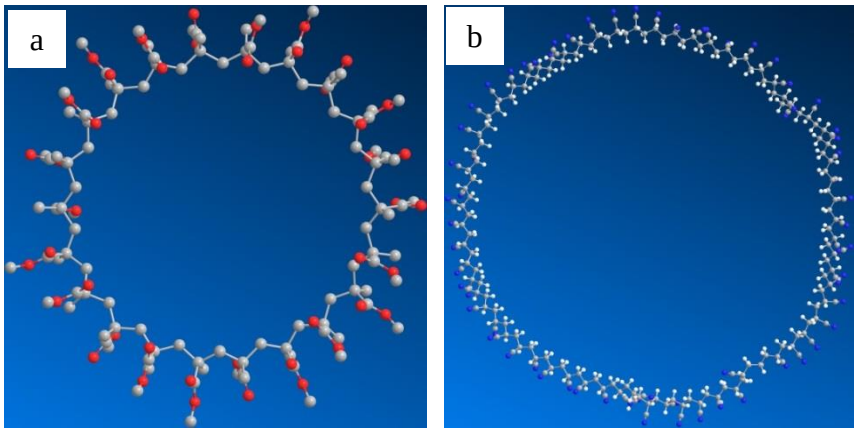

Figure 2-3. The diameter of **(a)** PMMA and **(b)** PAN, when the chain is in trans configuration. The diameter of the helix created by these two polymers is ~1.6 and ~6 nm for PMMA and PAN, respectively.

2.3.2 TGA, XRD, and Raman Spectroscopy and Elemental Analysis

All three PMMA dispersions (with SWNT, FWNT, and MWNTs) contained 91% PMMA with respect to the total weight of PMMA and CNT in DMF. However, based on the TGA study (Figure 2-4) and the weight of the buckypaper after drying, it was estimated that the PMMA in FWNT/PMMA and MWNT/PMMA as produced buckypaper was 9% and 7%, respectively, while it was 37% in as produced SWNT/PMMA buckypaper. The remaining PMMA is filtered out with DMF during vacuum filtration. Higher PMMA weight retention in SWNT containing samples as compared to FWNT and MWNT containing samples suggested a specific interaction between PMMA and SWNT, and not between PMMA and FWNTs, and nor between PMMA and MWNTs.

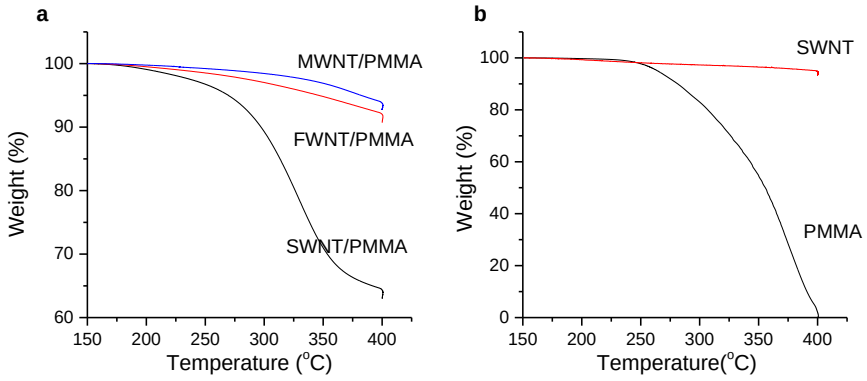

Figure 2-4. Thermogravimetric analysis of **(a)** CNT/PMMA and **(b)** PMMA and SWNT buckypapers under Nitrogen at a heating rate of 10 °C/min up to 400 °C and held at that temperature for 5 minutes. The SWNT buckypaper has a 6 percent mass loss.

The diffraction pattern of PMMA exhibits three amorphous peaks (Figure 2-5a). The diffraction pattern of the FWNT/PMMA and MWNT/PMMA buckypapers is similar to their control buckypaper patterns as shown in Figure 2-5b. Sonication of SWNTs and PMMA in DMF resulted in a stable suspension, which after filtering the solvent, displayed a sharp peak at 0.83 nm (Figure 2-6a). When the X-ray beam (Z-direction) was perpendicular to the buckypaper plane (XY plane), the diffraction pattern was isotropic, as expected. However, when the X-ray beam (Z-direction) was parallel to the plane of the buckypaper (XY plane), then the diffraction pattern exhibited anisotropy (Figure 2-6b). The new strong intensity peak at 0.83 nm appeared on the meridian, which suggested that the feature giving rise to this peak is oriented along the CNT axis. After burning out the PMMA at 400 °C in the presence of nitrogen, the sharp peak disappeared and the resulting diffraction pattern was similar to that of the control SWNT buckypaper processed without PMMA.

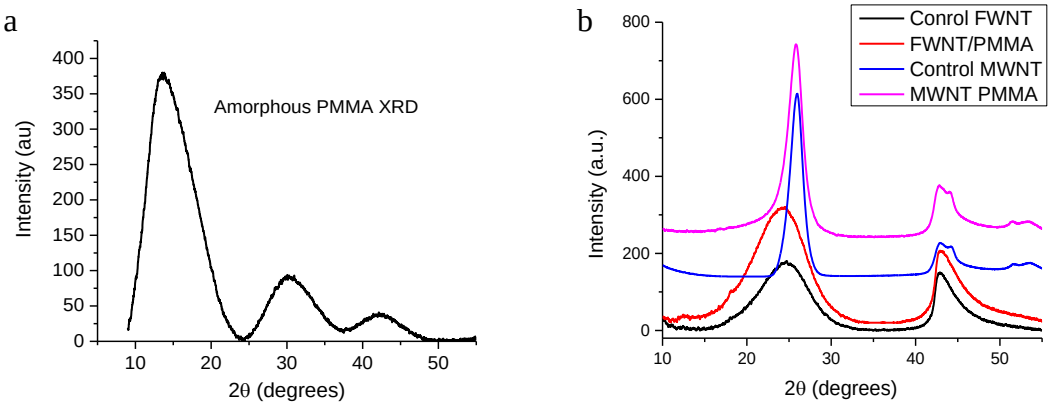

Figure 2-5. WAXD of (a) PMMA, and (b) FWNT and MWNT control and PMMA processed buckypapers.

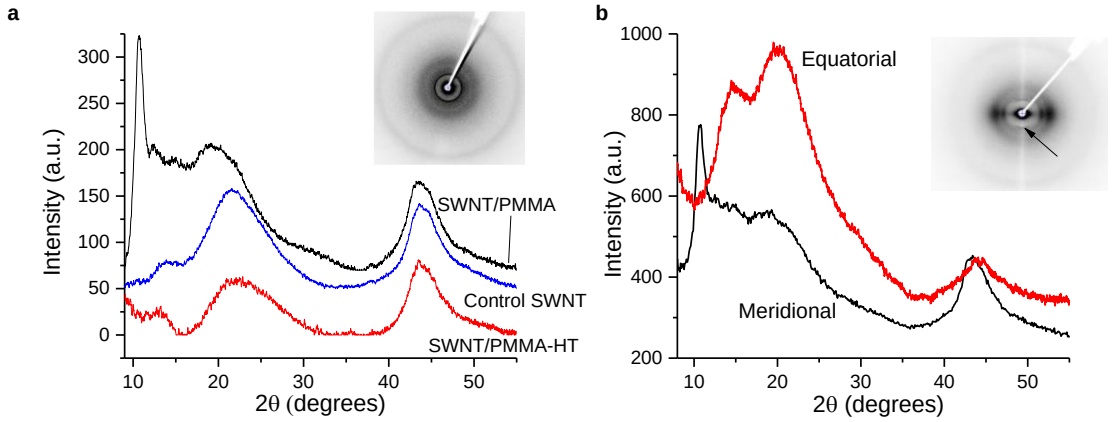

Figure 2-6. (a) WAXD of SWNT, SWNT/PMMA, and SWNT/PMMA – HT buckypapers. X-ray beam in all cases is perpendicular to the plane of the buckypaper. SWNT/PMMA – HT is a sample, where PMMA is completely removed. Inset is the 2D pattern of SWNT/PMMA. (b) Meridional and equatorial scans of SWNT/PMMA buckypaper, and the 2D pattern (inset) when the X-ray beam is parallel to the plane of the buckypaper.

The 0.83 nm peak was observed regardless of the PMMA molecular weight (Figure 2-7a). Three different molecular weight PMMA samples were used. The 0.83 nm peak intensity increases with molecular weight, while the PMMA content in all three buckypapers prepared *via* filtration was comparable at ~37%. In contrast to filtration,

where approximately 95% of the PMMA is filtered out with the solvent for the PMMA/SWNT buckypaper, when the solvent is removed *via* evaporation, all the PMMA remains in the buckypaper. Thus, the SWNT/PMMA buckypaper prepared by evaporation results in almost 20 times more PMMA than the buckypaper prepared by filtration. The SWNT/PMMA buckypaper prepared by evaporation still shows 0.83 nm ordered PMMA peak. However, this peak is almost dwarfed by the amorphous PMMA peak (Figure 2-7b).

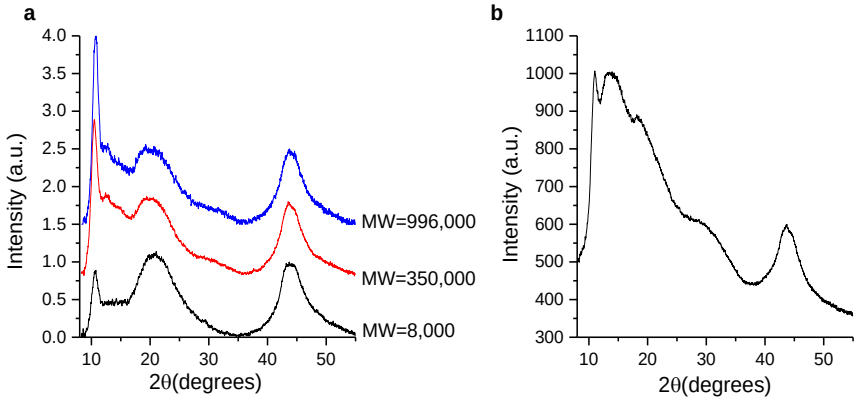

Figure 2-7. WAXD of **(a)** SWNT/PMMA buckypapers fabricated with different molecular weight PMMA as indicated and **(b)** SWNT/PMMA buckypaper, where solvent was removed *via* evaporation.

Polymer wrapping also takes place in other polar organic solvents such as dimethyl sulfoxide (DMSO) and nitromethane. When DMSO was used the intensity of the shark peak was smaller and shifted from 2θ=10.8° to 11.2°, corresponding to a d-spacing of 0.79 nm (Figure 2-8). The PMMA wrapped SWNTs did not disperse in DMSO and formed aggregates. This may be due to the interaction between the exposed methyl-methacrylate functional groups with the solvent.

The new peak was also observed when nitromethane, which is also a good solvent for both PMMA and SWNTs, was used instead of DMF. Since unpurified SWNTs were used, the diffraction pattern was swamped by the metallic impurities. Despite the strong baseline intensity from the impurities, the peak at ~10.8° was still visible in the buckypaper XRD (Figure 2-9).

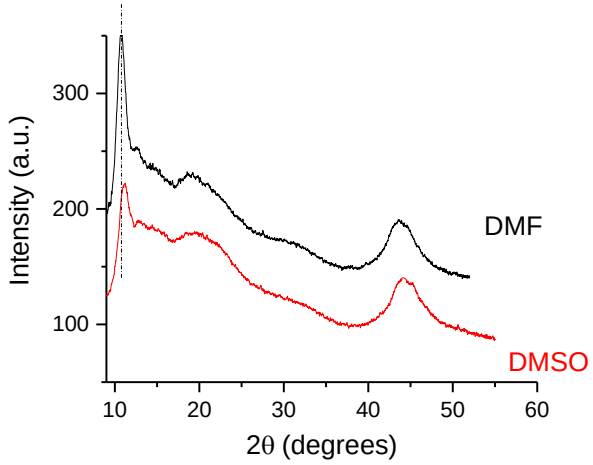

Figure 2-8. X-ray diffraction of SWNT/PMMA buckypapers processed with DMF and DMSO.

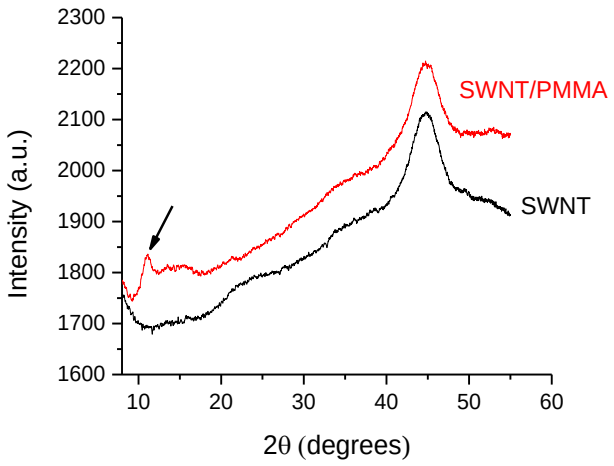

Figure 2-9. X-ray diffraction pattern of unpurified SWNT and SWNT/PMMA processed with nitromethane. Despite the strong background intensity from the SWNT impurities, the new peak is still visible.

The X-ray photoelectron spectroscopy (XPS) spectra of the pristine and PMMA processed buckypaper after removing PMMA, indicates that the elemental composition of the buckypaper does not change with PMMA processing (Table 2-1 and Figure 2-10). This suggests that the PMMA/SWNT interaction is non-covalent. The Raman spectra of the buckypapers have similar G:D band ratio, indicating no change in defect density upon PMMA processing and removal of the PMMA (Figure 2-11).

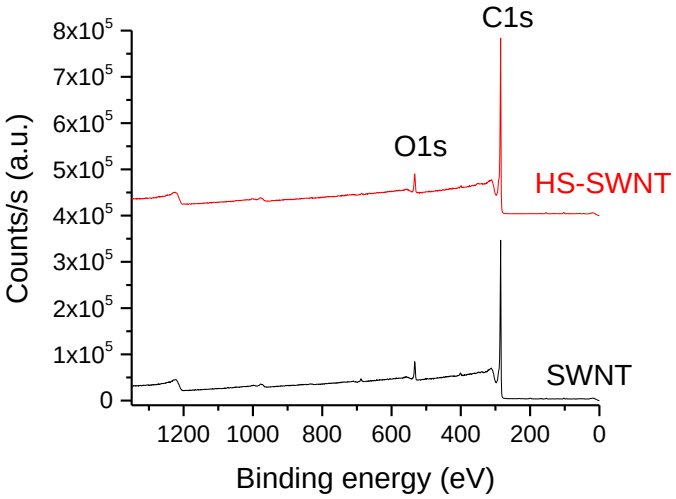

Figure 2-10. XPS plots of SWNT and HS-SWNT buckypapers.

Table 2-1. Chemical composition of SWNT buckypapers determined from XPS spectra in Figure 2-10.

Sample	**Atomic %**			**Ratio**
	C	O	N	**(C/O)**
HS-SWNT	94.65	5.35	0	17.7
SWNT	94.5	5.50	0	17.2

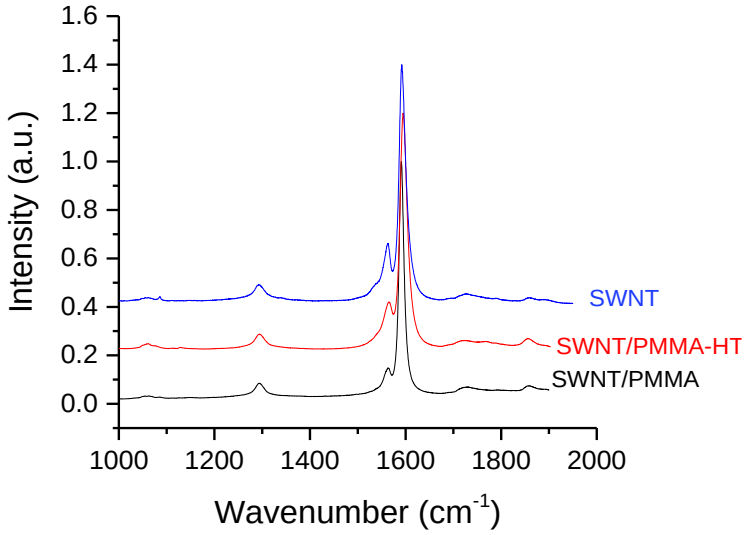

Figure 2-11. Raman spectra of the three buckypapers showing similar D-band intensities. Intensities have been normalized to the G-band.

2.3.3 Helical Model Validation

Helical wrapping of PMMA has been suggested for the SWNT/PMMA interaction (Figure 2-12). It has been proposed that PMMA wraps neatly around SWNTs and the sharp peak in the XRD corresponds to the distance between pendant groups along the nanotube axis. From energy minimization of PMMA chains in trans configuration, the C-C-C bond angle in the backbone is ~107°, when methyl methacrylate (MMA) is on the central carbon, and ~123°, for the other carbon. The model was initiated with these C-C-C bond angles. The dihedral angle was chosen to match the helical pitch of 0.83 nm. The tacticity was achieved by assigning the methacrylate group to the left or right side based on a randomly generated binary vector. Each complete helical revolution consists of 21 to 22 monomers, with a diameter of ~1.6 nm, creating a hole sized for smaller nanotubes. Energy minimization (using Chembio3D molecular dynamics simulation) was carried out on the initial chain model.

Enthalpy driven CH-π interactions are possibly the main drive for the wrapping, resulting in lower energy. The existence of CH-π interactions has been known for a long time [135-137]. The strength of the CH-π is one tenth of hydrogen bonding but multiple CH-π interactions along the polymer chain length between the CH_2 and the π bonds can add up to make the helical wrapping energetically favorable. If the SWNT structure does not change significantly after removing the PMMA as a first order approximate, the diffraction pattern of the PMMA in the SWNT/PMMA buckypaper can be obtained by subtracting the diffraction pattern of SWNT from SWNT/PMMA as shown in Figure 2-13a. The diffraction pattern of the energy minimized helical model was obtained using

Debyer and is shown in Figure 2-13b, which is similar to the diffraction pattern of the ordered PMMA.

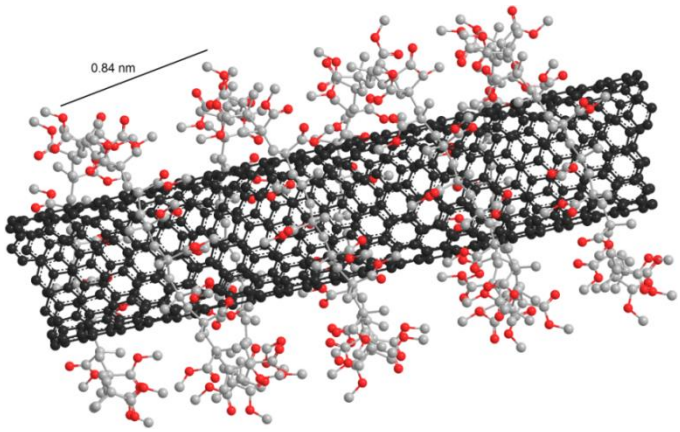

Figure 2-12. SWNT (12,1) wrapped by PMMA (Colors: Carbon (gray), Oxygen (Red), Hydrogen hidden).

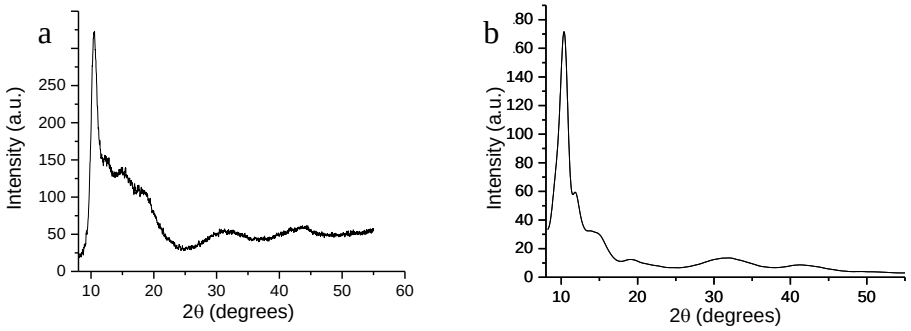

Figure 2-13. a) Ordered PMMA diffraction pattern in SWNT/PMMA buckypaper obtained by subtracting the SWNT diffraction pattern from the SWNT/PMMA pattern, b) Calculated diffraction pattern from model.

Energy minimization (using Chembio3D molecular dynamics simulation) was carried out on the initial chain model shown in Figure 2-14a, and the minimum energy configuration is shown in Figure 2-14b. After this energy minimization, chain was heated

to 400 K, and the energy minimization process was again carried out. The resulting random coil configuration is shown in Figure 2-14c. The total energy of the PMMA went from 77670, to 2980, and subsequently to 2890 kcal/mol, showing that the energy for the helical configuration is slightly higher than that of the random coiled state.

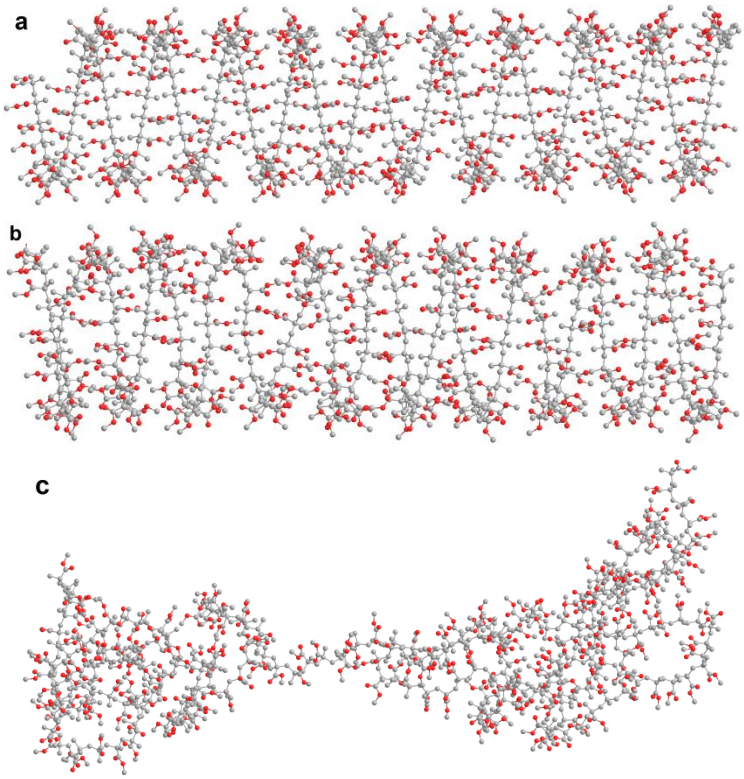

Figure 2-14. PMMA with 220 monomers (a) initial configuration (E=77,670 kcal/mol) (b) After energy minimization (E=2,980 kcal/mol) (c) Configuration in (b) was heated to 400 K and then the energy minimization step was repeated (E=2,890 kcal/mol).

2.3.4 Dispersion Analysis

2.3.4.1 CNT suspension quality and its influence on Buckypaper and film quality

The suspendability of CNTs are generally low, even in good solvents. In order to get a good SWNT suspension during sonication, a concentration of at most ~14mg/L is required. If the concentration of the SWNTs is too high, the nanotubes will not disperse regardless of the sonication time (Figure 2-15).

Figure 2-15. SWNT/DMF (100 mg/L) suspension after 48 hours of sonication. At this concentration the aggregates do not disperse.

As sonicated SWNT/DMF and SWNT/PMMA/DMF suspensions had similar appearance initially (Figure 2-16a,b). However, the SWNT/DMF suspension precipitated within 2 hours of centrifugation at 2,000 g while the SWNT/PMMA/DMF dispersion was quite stable and exhibited very little sedimentation under comparable centrifugation conditions (Figure 2-16c,d). This SWNT/PMMA/DMF suspension exhibited no further change even after prolonged centrifugation time of 72 hours, and it remained stable indefinitely (observed for 3 months).

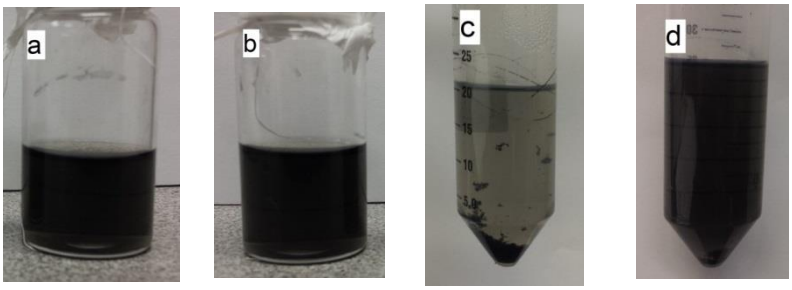

Figure 2-16. As sonicated (a) SWNT/DMF, and (b) SWNT/PMMA/DMF suspensions. (c) SWNT/DMF suspension after 2-hour centrifugation, d) SWNT/PMMA/DMF suspension after 72-hour centrifugation.

The dispersion quality will have an influence on the preparation of the films, fibers and buckypapers. A bad dispersion will result in non-homogeneous samples which are difficult to process, and will have negative impact on the mechanical and functional properties of the composite. When the concentration is high and the SWNT dispersion is not well suspended, as in Figure 2-15, the resulting buckypaper does not have good integrity and tears easily upon peeling (Figure 2-17a). This is the result of individual aggregates stacking on each other during filtration (Figure 2-18a), resulting in a minimal interaction between these bundles. In addition to that, since the nanotubes are not entangled and restrained, the buckypaper shrinks a third in diameter upon drying. Therefore, just by visually examining the buckypaper the dispersion quality can be inferred.

When a buckypaper is made with a well dispersed suspension at low CNT concentration, an entangled network of individual and small bundles of nanotubes is created (Figure 2-18b). The entangled network of CNTs provides the buckypaper with modest mechanical properties and integrity, which facilitates peeling and handling of the

buckypaper. By processing the SWNTs with PMMA, the SWNTs can be suspended at concentrations as high as (800 mg/L), where the resulting buckypapers exhibit the qualities of well dispersed SWNTs (Figure 2-17).

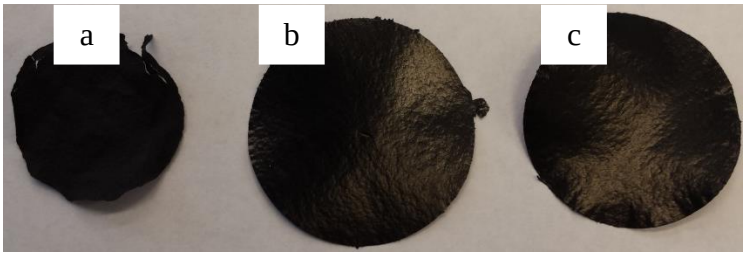

Figure 2-17. SWNT Buckypapers made at concentrations of (a) SWNT/DMF (160 mg/L), (b) SWNT/DMF (30 mg/L), (c) SWNT/PMMA/DMF (800 mg/L, 1:1 ratio SWNT:PMMA)

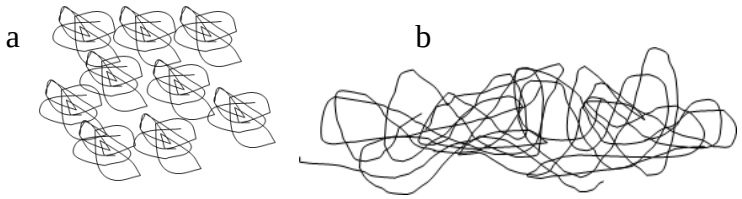

Figure 2-18. Schematic of a) well dispersed nanotubes and b) stacked aggregated bundles.

The effect of PMMA wrapping on dispersion is even more obvious in dry cast PMMA films. PMMA/SWNT films were made with 0.1 wt% SWNT by dry casting. The suspensions were prepared at a concentration of 15 mg/L. The films were made with and without PMMA wrapped SWNTs. This was done by adding a small amount of PMMA (1:1 PMMA:SWNT) before sonication to achieve PMMA wrapping. After 24 hours of sonication, PMMA was added to the suspensions to reach the final PMMA:SWNT ratio of 1000:1 and stirred for 24 hours. For the SWNT wrapped system, the dispersion was

stable and homogeneous resulting in a homogenous film (Figure 2-19). On the other hand, the non-wrapped SWNTs form aggregates in the film (Figure 2-19). While the SWNT suspension was visibly homogeneous after sonication, after adding PMMA powder and initiating stirring, the SWNTs started to form visible aggregates within 20 minutes. Micrographs of the films presented in Figure 2-20 show severe aggregation and inhomogeneities in the non-wrapped SWNT film, while the wrapped SWNT film exhibits a fine uniform dispersion.

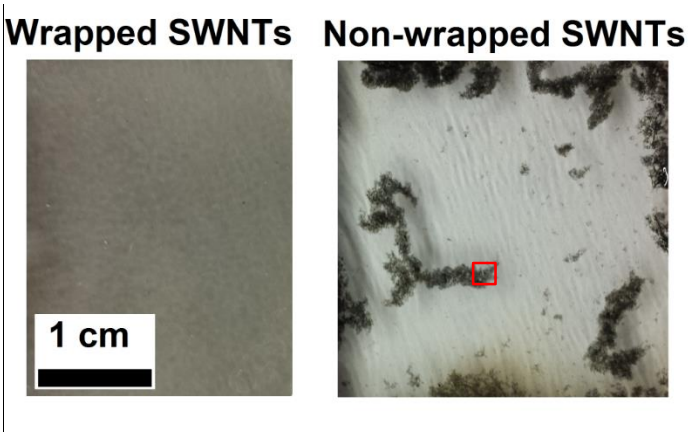

Figure 2-19. Image of 0.1 wt% SWNT films, with wrapped and non-wrapped SWNTs. SWNTs aggregate into small islands when they are not wrapped with polymer. Scale bar applies to both images. The red box outlines the section from which the optical micrograph was taken in Figure 2-20.

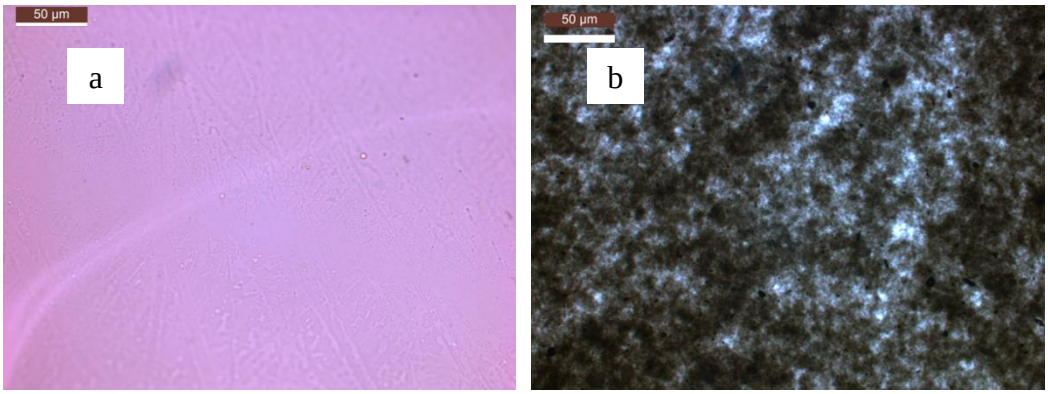

Figure 2-20. optical micrographs of PMMA/SWNT (1 wt %) film (a) wrapped SWNTs, (b) non-wrapped SWNTs.

2.3.4.2 UV-vis spectroscopy of suspension

The UV-vis absorption spectra of the SWNT/DMF and SWNT/PMMA/DMF suspensions before and after centrifugation are shown in Figure 2-21. The suspensions were centrifuged for 2 hours at 10,000 RPM and the supernatants were collected for UV-vis. The SWNT/DMF suspension shows much lower absorbance after centrifugation due to higher re-aggregation and sedimentation of the nanotubes, resulting in lower SWNT concentration in the supernatant. The van Hove transitions in SWNT/PMMA/DMF were blue shifted 12-24 meV as compared to SWNT/DMF both before and after centrifugation (Figure 2-21). The van Hove transition energy of nanotubes redshift upon bundling [138]. This indicates that the SWNT reaggregation starts immediately after stopping sonication. So the PMMA wrapping not only prevents nanotube aggregation and sedimentation, but the PMMA wrapped nanotubes are more exfoliated compared to the SWNT suspension.

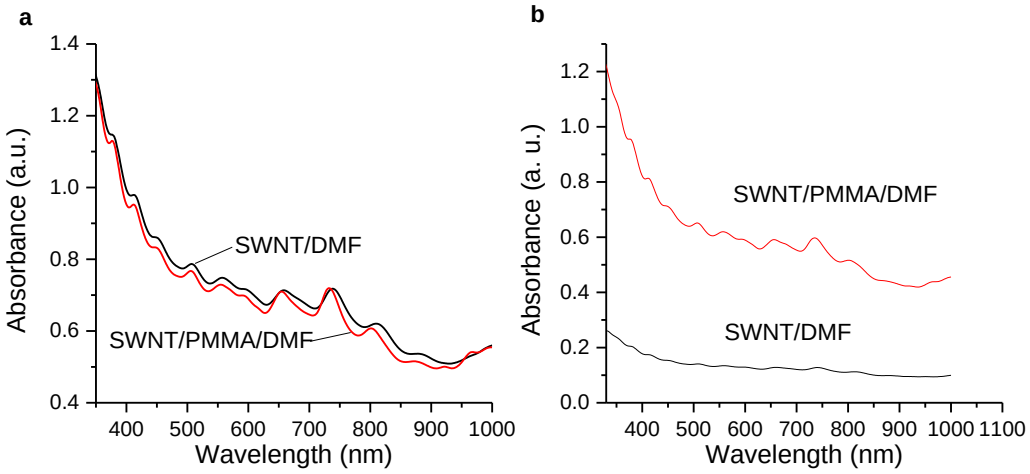

Figure 2-21. Absorption spectra of (a) as sonicated and (b) centrifuged supernatant SWNT/DMF and SWNT/PMMA/DMF suspensions. Significantly lower absorption in SWNT/DMF suspension as compared to SWNT/PMMA/DMF suspension after centrifugation is due to sedimentation in SWNT/DMF than in SWNT/PMMA/DMF.

2.3.4.3 Monitoring aggregation using Raman spectroscopy

The Raman spectra using a 785 nm laser in Figure 2-22a shows higher intensity for (12,1), (10,5) and (9,7) and lower intensity for (10,2), (9,4) and (13,3) nanotubes for SWNT/PMMA compared to SWNT samples; at that laser energy the former three nanotubes are in resonance when individualized while the latter three are in resonance while bundled [138] (Table 2-2), showing the influence of polymer wrapping on individualizing the nanotubes. The Raman profile of the SWNT/PMMA sample is similar to that of SDS/SWNT [139, 140], where the SDS surfactant is intended to exfoliate the bundled nanotubes.

After removing the PMMA by heat treatment, the nanotube-nanotube interaction increases, causing a redshift in the transition energy, hence a change in RBM intensities (Figure 2-22b). The nanotubes are restricted in the buckypaper network and are not free

to rebundle and pack as well as the as sonicated SWNT. The redshift of E_{22} transition energy reverses the intensity of the peaks of the debundled SWNT/PMMA. Since the change in transition energy is not the same for all nanotubes [138], the intensities do not change proportionately. There is an upshift of ~2 cm^{-1} for all of the RBM frequencies in the SWNT/PMMA and SWNT samples compared to SWNT/PMMA-HT, which could be attributed to polymer wrapping [141-143] and bundling [144, 145], respectively.

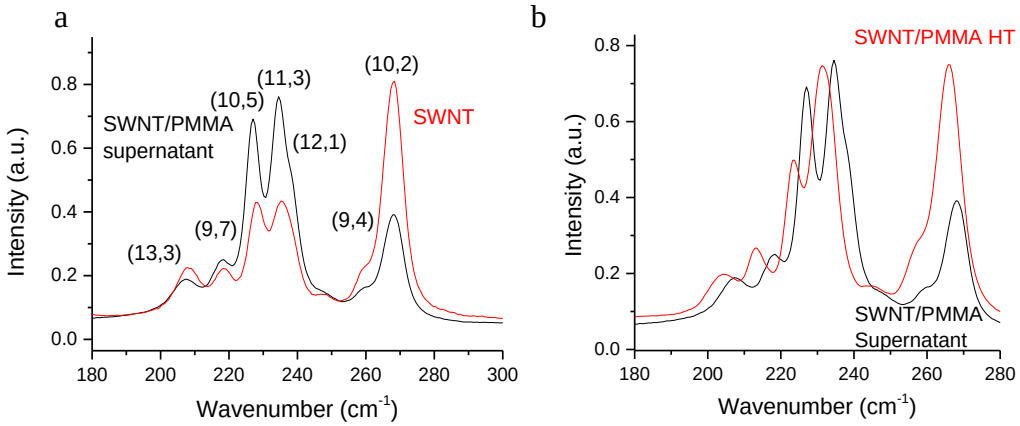

Figure 2-22. Raman RBM spectra using 785 nm laser. (a) The samples were prepared by depositing SWNT/DMF or SWNT/PMMA/DMF on a glass slide. (b) Raman spectra after removing the PMMA wrapping. All intensities were normalized to G-band intensities.

Table 2-2. HiPco chiralities that can be detected with the 785 nm excitation wavelength [138]. *close to excitation wavelength, 785 nm, of the laser.

(n,m)	Diameter (nm)	Frequency (cm^{-1})	E (indiv.) (nm) [eV]	E (roped) (nm) [eV]
(10,2)	0.88	264	729 [1.7]	776 [1.6]*
(9,4)	0.92	256	718 [1.73]	763 [1.62]*
(12,1)	0.99	236	792 [1.57]*	825 [1.50]
(11,3)	1.04	233	792 [1.57]*	-
(10,5)	1.05	225	784 [1.58]*	819 [1.51]
(9,7)	1.10	215	789 [1.57]*	820 [1.51]
(13,3)	1.17	205	754 [1.64]	787 [1.58]*

Sonicating SWNTs with another polyacrylate also resulted in a debundled state. The Raman spectrum of poly(butyl methacrylate) (PBMA)/SWNT samples also indicated debundled SWNTs (Figure 2-23). PBMA has a larger side chain than PMMA Figure 2-24, but the bond angles are similar to that of PMMA, allowing it to wrap SWNTs.

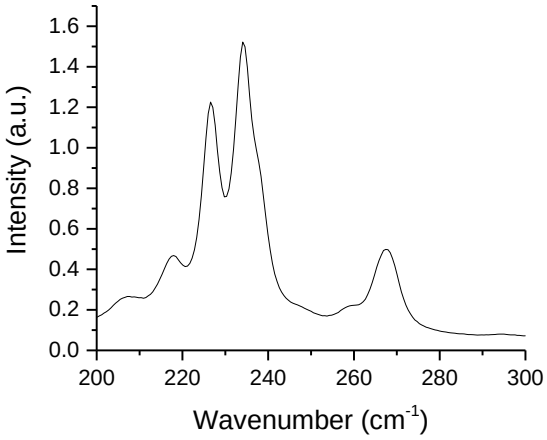

Figure 2-23. Raman spectrum of SWNT wrapped with PBMA. Intensity normalized to Raman G band.

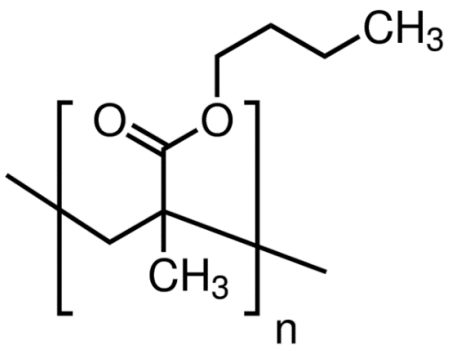

Figure 2-24. Repeat unit of PBMA polymer.

2.3.4.4 Porosimetry

The surface area and pore size of nanomaterials can be measured using gas adsorption. To analyze the porosity, the sample is first degassed to remove all moisture from the porous structure. The sample is heated to 90° C under vacuum and kept at that temperature for 16 hours to ensure complete removal of moisture. The sample tube is then backfilled with nitrogen gas. At this stage the sample is ready for analysis. In the beginning of the analysis, the sample tube is evacuated to very low pressures. Depending on the analysis gas and the bath temperature, different amounts of gas is admitted into sample tube to probe the material structure. When the adsorbate gas is nitrogen (N_2) the bath temperature is maintained at 77 K. Nitrogen is admitted in incremental doses at different partial pressures up to the gas saturation pressure to probe the pore structure of the material. The amount of gas quantity adsorbed vs gas pressure is plotted to generate an adsorption isotherm, which can reveal the structure of the adsorbing material (called adsorbent) from the shape of isotherm. The classical adsorption theory assumes that the adsorbate first forms a monolayer on the surface before beginning to form a second layer. The surface area is calculated using the adsorbate molecule dimensions and the number of molecules admitted to the sample tube at increasing partial pressures. The Brunauer–Emmett–Teller (BET) theory can be used to calculate the surface area of the material. The isotherm of silica alumina, which is used to ensure the accuracy of the porosimetry system, is shown in Figure 2-25. The BET equation is:

$$\frac{1}{v[(p_0/p)-1]} = \frac{c-1}{v_m c}\left(\frac{p}{p_0}\right) + \frac{1}{v_m c} \qquad (2\text{-}1)$$

where p and p_0 are the equilibrium and the saturation pressure of adsorbates at the adsorption temperature, v is the adsorbed gas quantity, and v_m is the monolayer adsorbed gas quantity. c is the BET constant:

$$c = \frac{E_1 - E_L}{RT} \quad (2\text{-}2)$$

where E_1 is the heat of adsorption for the first layer and E_L is that for higher layers, R is the gas constant and T is the temperature. The constant c can be regarded as the affinity of the solid with the adsorbate. The left side of (2-1) can be plotted as a function of $\frac{p}{p_0}$ as a straight line which is called the BET plot. The linear relationship only holds within a limited range, usually $0.05 < \frac{p}{p_0} < 0.35$. The value of slope A and intercept I of the fitted line is used to calculate the monolayer adsorbed gas quantity v_m and constant c, using the equations $v_m = \frac{1}{A+I}$ and $c = 1 + \frac{A}{I}$. The BET plot of the reference silica alumina sample is shown in Figure 2-26. There are some criteria for correct selection of the pressure range from which I and A are calculated. First of all the constant c must be positive (c>0). Secondly, the Rouquerol transform $v[1 - (p/p_0)]$ should be increasing with p/p_0 for the data selected to calculate the BET parameters. For the alumina silica sample the Rouquerol transform decreases above $p/p_0 = 0.25$ (Figure 2-27). When the correct ranged is used to obtain the v_m and c values, the specific surface area is obtained by the following equation:

$$S_{\mathrm{BET}} = \frac{v_m . N . s}{V . m} \quad (2\text{-}3)$$

where *N* is the Avogadro number, *s* is the cross sectional area of the adsorbate molecule, *V* is the molar volume of the adsorbate gas and *m* is the sample mass.

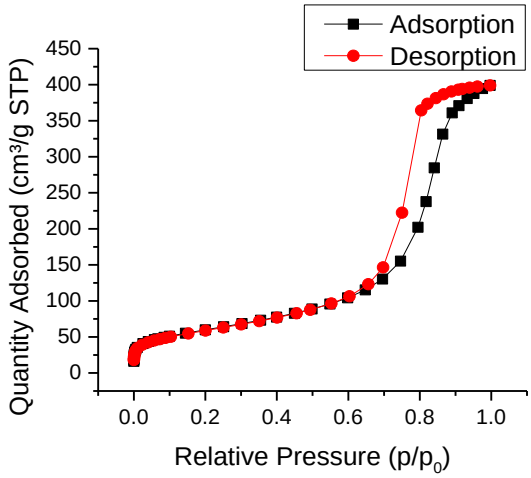

Figure 2-25. Nitrogen adsorption–desorption isotherm of silica alumina standard sample at 77 K.

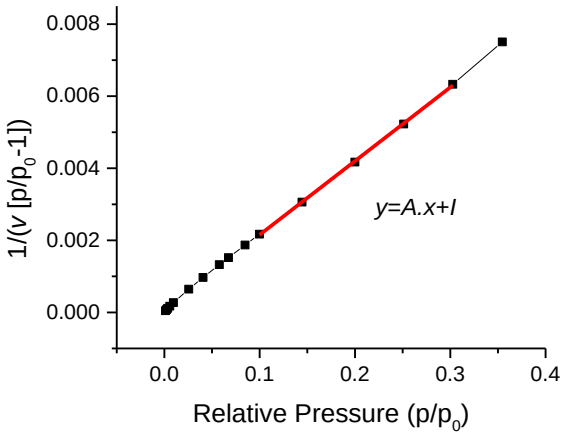

Figure 2-26. BET plot with a fitted line (in red) in the linear region.

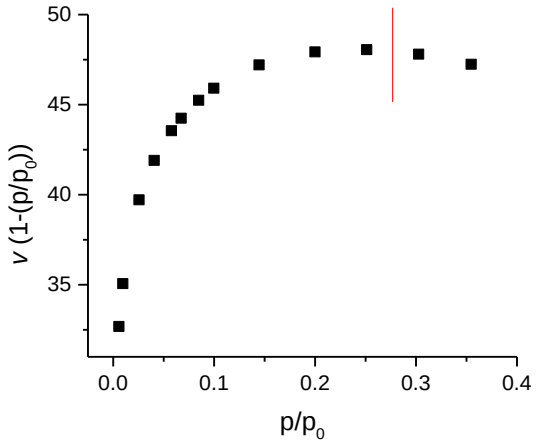

Figure 2-27. The Rouquerol transform as a function of partial pressure for the silica alumina sample. The red line denotes the cut of point where the Rouquerol transform starts to decrease.

The specific surface area (SSA) of the different buckypapers is presented in Table 2-3. FWNTs have lower SSA than SWNTs since the inner walls are not accessible. The SWNT sample exhibits an SSA of 600 m^2/g, since the nanotubes can rebundle after sonication and reduce surface area. However, for the high surface area PMMA processed buckypapers, HS-SWNT, we obtained SSA as high as 1030 m^2/g (average bundles of 4 SWNT from theoretical calculations). Measurements of 11 PMMA processed buckypapers yielded an average specific surface area of 943 ± 69 m^2/g (nitrogen gas adsorption isotherms for these 11 samples are shown in Figure 2-28). The increase of SSA for the PMMA processed SWNT buckypaper compared to the SWNT buckypaper confirms that the PMMA wrapping prevents the aggregation of the SWNTs, resulting in higher SSA after the PMMA is removed. The added pores are mainly micro and mesopore in size, from 1 to 11 nm pore width, as shown in Figure 2-29. The additional surface area in the 1 nm region are likely due to the removed PMMA wrapping, resulting

in micropores between adjacent nanotubes (Figure 2-30). The isotherm of the sample is shown in Figure 2-31.

Table 2-3. Surface Area measurement for the CNT and CNT/PMMA buckypapers. SWNT sample average of 5 measurements and HS-SWNT sample average of 10 measurements.

Sample	BET SSA (m^2/g)	Comments
FWNT	260	Slurry
FWNT	450	As sonicated
SWNT	460	Slurry
SWNT	600 ± 100	As sonicated
SWNT/PMMA	280	PMMA processed
HS-SWNT	950 ± 70	PMMA processed- PMMA removed

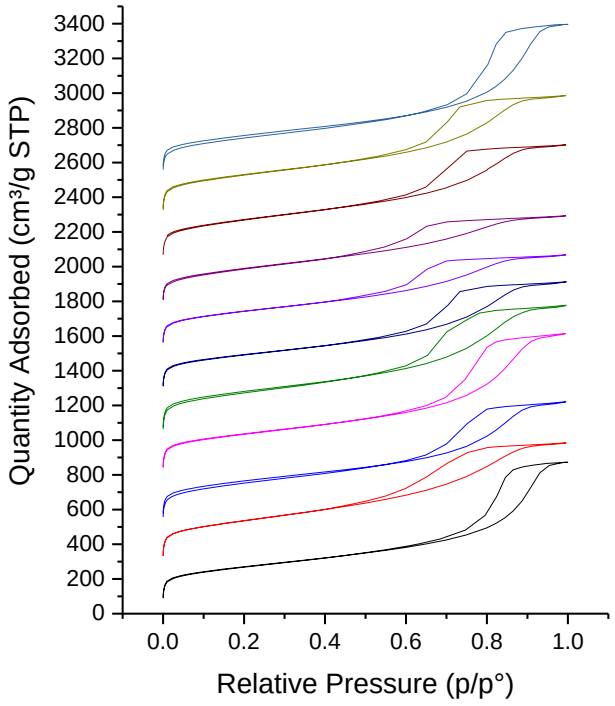

Figure 2-28. N_2 gas adsorption isotherms of PMMA processed buckypapers, with an average specific surface area of 943 m^2/g. Each isotherm has been shifted 250 units vertically with respect to the previous plot for clarity.

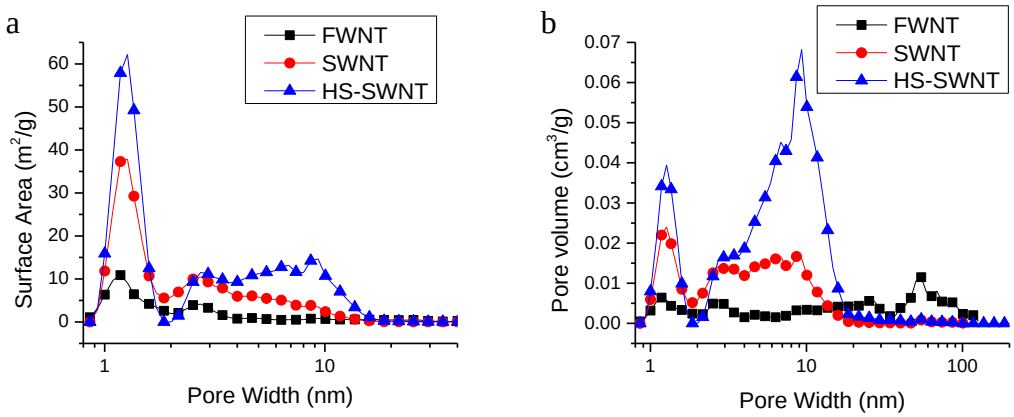

Figure 2-29. Pore size distribution, (a) surface area and (b) pore volume at different pore size.

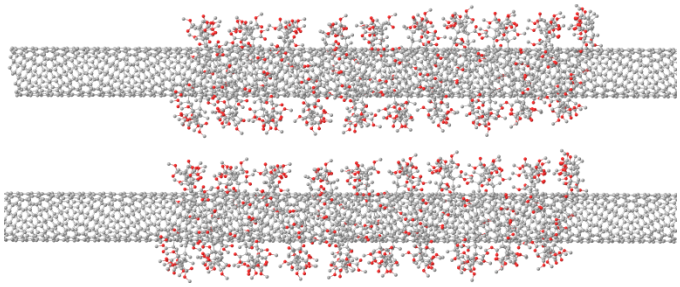

Figure 2-30. PMMA wrapping around SWNTs prevent them from aggregating. Micropores are created when the wrapped PMMA from adjacent SWNTs is removed.

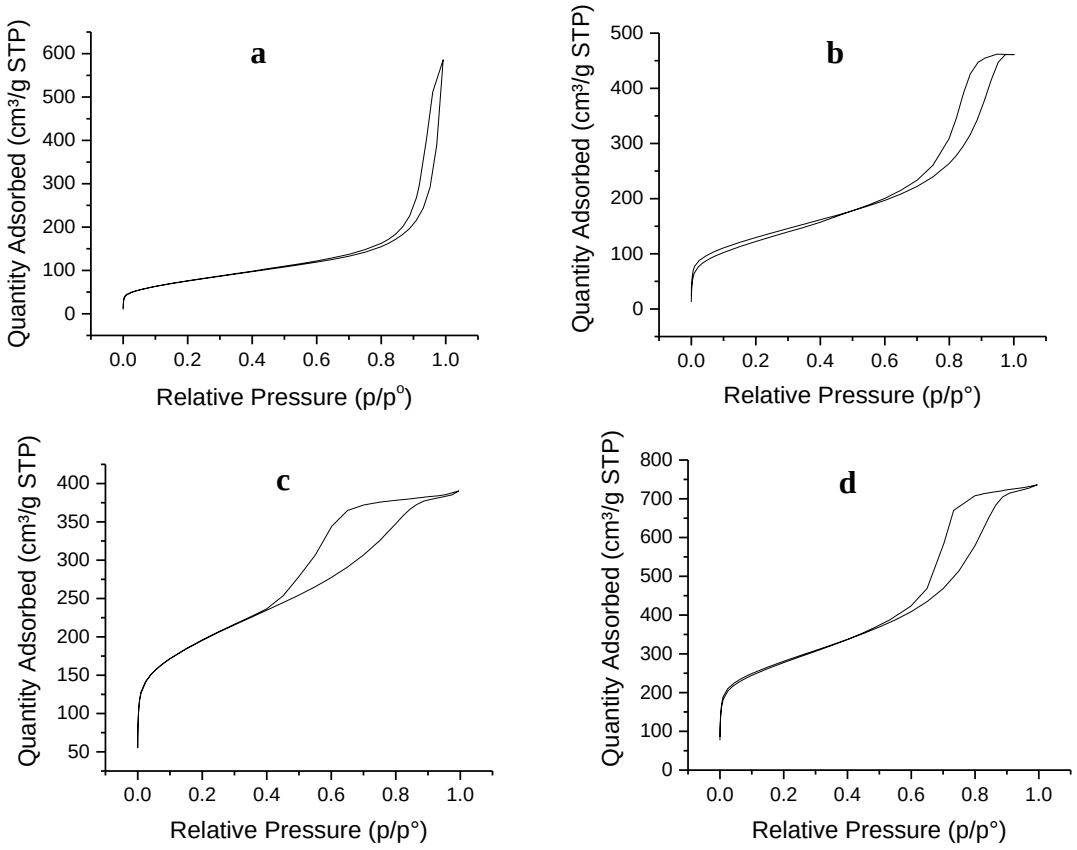

Figure 2-31. N_2 adsorption isotherms of a) FWNT, b) SWNT slurry, c) SWNT, and d) HS-SWNT buckypapers at 77 K.

2.4 Conclusions

Carbon nanotubes tend to bundle due the collective van der Waals interaction along the length of CNTs. In this chapter we demonstrated a technique to wrap SWNTs with PMMA. The wrapping only takes place around CNTs with a diameter of ~1 nm, and it does not occur with FWNTs or MWNTs. This has been attributed to the bond angles of the PMMA backbone which provide a hole sized for SWNTs, and favorable interaction between the CH_2 side chains of PMMA with SWNT and the polymer-solvent interactions. PMMA wraps in an ordered helical manner around SWNTs, and while the helical wrapping cannot be observed directly using TEM due to the dimensions of the

structure, the ordered morphology of the wrapping results in a sharp peak in the X-ray diffraction pattern. The helical morphology of PMMA was confirmed by simulating the diffraction pattern of the proposed model, which was a good match with the experimental diffraction pattern.

The PMMA wrapping not only increases the suspendability of SWNTs from 0.014 mg/mL to more than 1 mg/mL, but also improves the suspension stability over the period of several months as compared to days for as sonicated SWNTs. From UV-vis spectroscopy, we observed that all excitation bands of SWNTs blue shift upon being wrapped with PMMA. This is consistent with debundling of SWNTs, since SWNT van Hove transitions red shift upon bundling. From Raman spectroscopy, it was observed that all chiralities are debundled when processed with PMMA, ruling out wrapping selectivity for the SWNTs probed with 785 nm laser. Finally, the effect of PMMA wrapping on the porous structure and specific surface area of SWNTs was studied. PMMA processed buckypapers had a specific surface area of more than 1000 m^2/g, showing a 50% increase in specific surface than as sonicated SWNTs.

Altogether, all of the evidence such as increased suspendability, stability of suspensions, UV-vis and Raman spectroscopy analysis, X-ray diffraction pattern and simulation, and surface area analysis, support the PMMA wrapping of SWNTs. For the first time since the discovery of carbon nanotubes, a polymer has been found that wraps CNTs in this manner.

CHAPTER 3

HIGH SURFACE AREA CARBON NANOTUBE ELECTRODES OBTAINED FROM POLYMER WRAPPED CARBON NANOTUBES FOR SUPERCAPACITORS

3.1 Introduction

Porous conductive materials that have a high surface area, such as carbon nanotubes (CNTs), are suitable for supercapacitor applications. In the previous chapter, it was demonstrated that single wall carbon nanotubes (SWNTs) have a higher specific surface area (SSA) than few wall carbon nanotubes (FWNTs). Buckypapers made from poly(methyl methacrylate) (PMMA) wrapped SWNTs have 58% higher SSA after the PMMA is removed compared to as-sonicated SWNT buckypapers.

Energy is stored at the electrode-electrolyte interface in electric double layer capacitors (EDLCs) or supercapacitors. Since the energy is stored at the interface, increasing the interface results in improvement in energy storage performance of EDLCs. Energy storage is expected to increase linearly with SSA, however, other factors such as pore size and porous architecture can affect energy storage. In this chapter the effect of SSA on energy storage is studied. Also supercapacitors made from high surface area SWNT buckypapers are compared to recently reported CNT and graphene supercapacitors in literature.

3.2 Experimental

3.2.1 Materials

HiPCO^{TM} SWNTs (grade sp300, average diameter 0.9 nm, purity 98%) and few wall CNTs (grade XOC231U, average diameter 2.7 nm, mainly two and three walled, purity 98.8%) were obtained from Carbon Nanotechnologies, Inc. Dimethylformamide (DMF, ACS grade, 99.8% purity) and PMMA (M_w= 350,000 g/mol) polymer were obtained from Sigma Aldrich. PTFE membrane (Zefon International, FPTPT147) with 1 μm pore size was used for the filtration.

3.2.2 Sample Preparation

A suspension containing 8 mg SWNT in 100 mL DMF was homogenized (IKA ULTRA-TURRAX T18) for 30 minutes and then 80 mg PMMA (dissolved in 40 mL DMF) was added to this SWNT/DMF suspension. After vigorous shaking, this PMMA/SWNT/DMF suspension was sonicated for 24 hours (Branson 3510R-MT, 100 W, 42 kHz). The suspension was filtered using the PTFE membrane and washed with methanol to remove DMF. The PMMA/SWNT buckypaper was peeled from the PTFE membrane and dried in vacuum oven at 70 °C for 3 days. The PMMA was removed by heating to 400 °C at 10 °C/min under nitrogen and then by holding at 400 °C for 5 minutes. The resulting sample is referred to as high-surface SWNT (HS-SWNT) buckypaper. SWNT and FWNT buckypapers were also made without the aid of PMMA. For these buckypapers, SWNT was dispersed at 1.3 mg/100 mL in DMF and sonicated for 24 hours. FWNT was dispersed at 1.3 mg/100 mL in DMF and sonicated for 5

minutes. Both the SWNT and FWNT suspensions were filtered using the PTFE membrane, washed in methanol, and the dried in vacuum at 70 °C for three days.

3.2.3 Characterization

For surface area and pore size analysis, isothermal N_2 gas adsorption study was carried out on various buckypapers using ASAP 2020 (Micromeritics Inc.) at 77 Kelvin. BET and BJH theories were used to obtain the specific surface area and pore size distribution, respectively. Scanning electron microscopy (SEM) was performed on a Hitachi SU8010 at an accelerating voltage of 5 kV. SEM was done on buckypapers without any metal coating. X-ray photoelectron spectroscopy (XPS) (Thermal Scientific K-alpha XPS instrument) was employed to analyze the buckypaper chemical composition. Raman spectroscopy on the buckypapers was carried out using 785 nm laser HORIBA XploRA Raman Microscope System. Scanning electron microscopy (SEM) was performed on a Hitachi SU8010 at an accelerating voltage of 5 kV. SEM was done on buckypapers without any metal coating. X-ray photoelectron spectroscopy (XPS) (Thermal Scientific K-alpha XPS instrument) was employed to analyze the buckypaper chemical composition. Raman spectroscopy on the buckypapers was carried out using 785 nm laser HORIBA XploRA Raman Microscope System. Galvanostatic constant current (CC) charging-discharging and cyclic voltammetry (CV) measurements were carried out on Solartron 1470 at room temperature, using two film electrodes. Electrode diameter, thickness and mass were approximately 6.4 mm, 15 μm, and 0.3 mg, respectively. The electrode density was 0.63 ± 0.02 g/cm^3, and the electrodes were separated by Celgard 3400 microporous membrane and were sandwiched between stainless steel current collectors. KOH aqueous solution (6 M) with potential range of 0

to 1 V and 1-Ethyl-3-methylimidazolium tetrafluoroborate ($EMIMBF_4$) with a potential range of 0 to 3 V were used as the electrolytes. For the constant current measurements, the specific capacitance was obtained using $C_{sp} = \frac{I\Delta t}{\Delta V}(\frac{1}{m_1} + \frac{1}{m_2})$ where I is the current, m_1 and m_2 are the masses of the two electrodes, Δt is the discharge time, ΔV is the discharge voltage during that time. Determination of $\Delta t/\Delta V$ excludes the IR drop occurring at the beginning of the discharge. The energy density was calculated using $E = \frac{\int VIdt}{m_1+m_2}$, and power density is $P = \frac{E}{t_d}$, where t_d is the total discharge time. The specific capacitance of the cyclic voltammetry measurements of each electrode was obtained using $C_{sp} = \frac{\int IdV}{2R\Delta V}(\frac{1}{m_1} + \frac{1}{m_2})$, where the integral is the area enclosed in the *V-I* plot, R is the CV scan rate and ΔV is the potential window.

3.3 Results and Discussions

3.3.1 Porosity

The buckypaper made from FWNT had the SSA of 300 m^2/g, and the one made from SWNT without the aid of PMMA had the SSA of 650 m^2/g. The highest surface area SWNT buckypaper obtained with the aid of PMMA, exhibited the surface area of 950 m^2/g, and this buckypaper is denoted as HS-SWNT buckypaper (Figure 3-1). The SWNT has lower SSA than HS-SWNT, as in the absence of PMMA, nanotubes re-bundle after sonication. The increase of SSA for the PMMA processed SWNT buckypaper compared to the buckypaper without the use of PMMA, supports the hypothesis that PMMA wrapping results in smaller diameter SWNT bundles and hence higher specific surface area, after PMMA has been removed. HS-SWNT, not only shows higher surface

area than SWNT and FWNT buckypapers, but it also shows higher pore volume (Figure 3-2). The data presented in shows that the higher pore volume was mostly due to micro and mesopores, with sizes in the range of 1 to 11 nm.

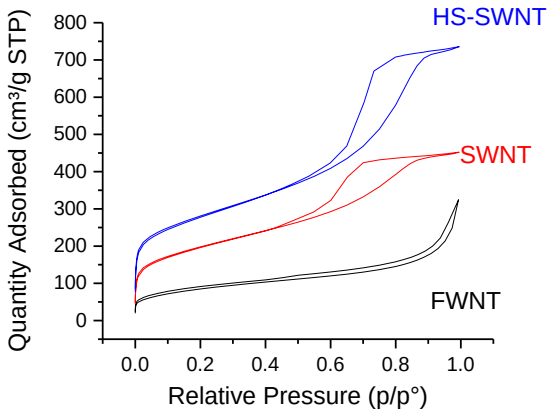

Figure 3-1. N_2 gas adsorption isotherms of FWNT, SWNT, and HS-SWNT buckypapers at 77 K.

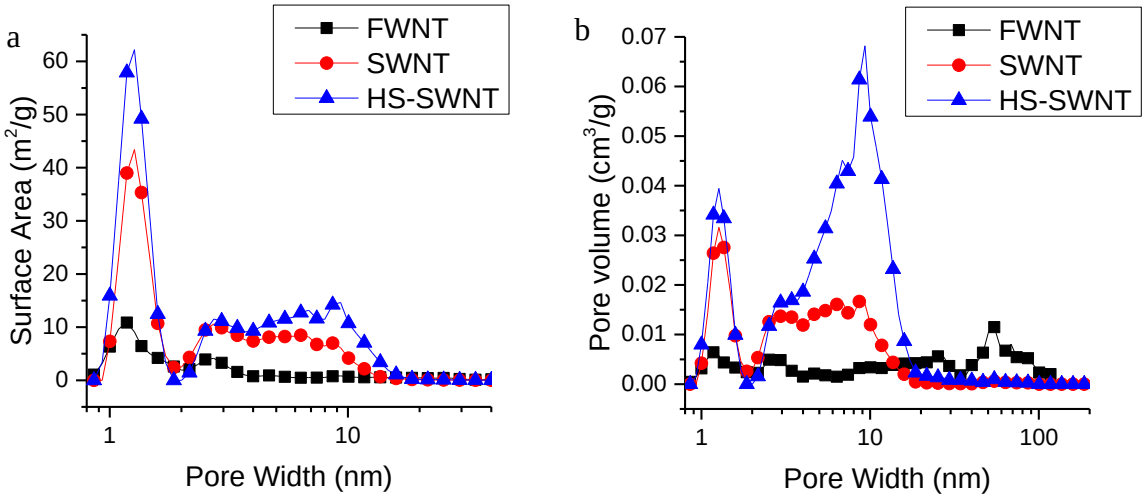

Figure 3-2. Pore size distribution obtained from BJH theory, (a) surface area and (b) pore volume at different pore size.

SEM images of the three buckypaper (FWNT, SWNT, and HS-SWNT) surfaces are given in Figure 3-3. The average CNT bundle diameters for FWNT, SWNT and HS-SWNT buckypapers measured from these images, using ImageJ software, are 22 ± 10 nm, 9 ± 4 nm, and 3 ± 2 nm respectively. These bundle diameters are qualitatively consistent with the surface area values measured from the nitrogen gas adsorption. In other words, as expected, buckypapers with low surface area have large bundle diameter and vice-versa.

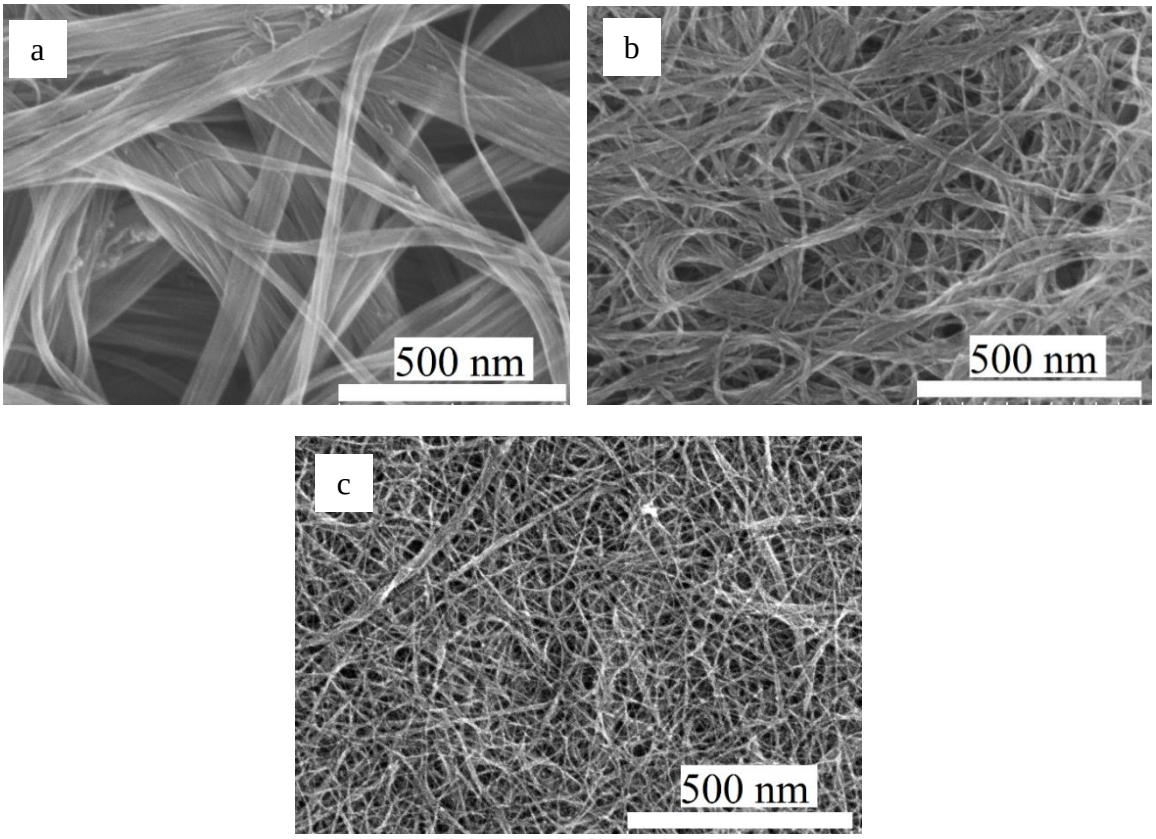

Figure 3-3. SEM images of (a) FWNT, (b) SWNT, and (c) HS-SWNT buckypapers.

3.3.2 Aqueous Electrolyte

The CC charge-discharge plots of the three different types of electrodes (FWNT, SWNT, and HS-SWNT) are shown in Figure 3-4. The specific capacitance and energy density values obtained from the CC measurements are given in Figure 3-5a and 5b. The capacitance and energy density decrease with increasing current densities. The energy density was calculated directly from current, voltage and discharge time, rather than from capacitance ($E = \frac{1}{2}CV^2$), as sometimes done. Thermogravimetric analysis in the previous chapter confirmed that PMMA is completely removed under the heat treatment conditions used for HS-SWNT processing, and there is no degradation and/or functionalization of SWNT. This has also been confirmed by Raman spectroscopy and XPS. Raman G/D ratio for both SWNT and HS-SWNT was ~11 (Figure 3-6). Presence of any amorphous carbon or SWNT functionalization would have resulted in a decreased G/D ratio, but this has not been observed. XPS data show that the C/O ratio in both SWNT and HS-SWNT buckypapers is also the same (Table 2-1). This confirms that the enhanced energy storage of HS-SWNT was only due to its higher surface area as compared to SWNT. Figure 3-5c shows the IR drop for each electrode as a function of current density, and shows that among the three types of electrodes studied in this work, at a given current density HS-SWNT shows much lower IR-drop, as compared to SWNT and FWNT electrodes. Lower internal resistance of the HS-SWNT capacitor suggests that the electrolyte is more readily accessible to various pores in HS-SWNT, as compared to SWNT and FWNTs, even at high current densities. The CV measurements do not show an oxidation peak, confirming the absence of pseudo capacitance (Figure 3-7a). HS-

SWNT electrode exhibited good rate capability, with a capacitance of 23 F/g at a high rate of 50 V/s (Figure 3-7b).

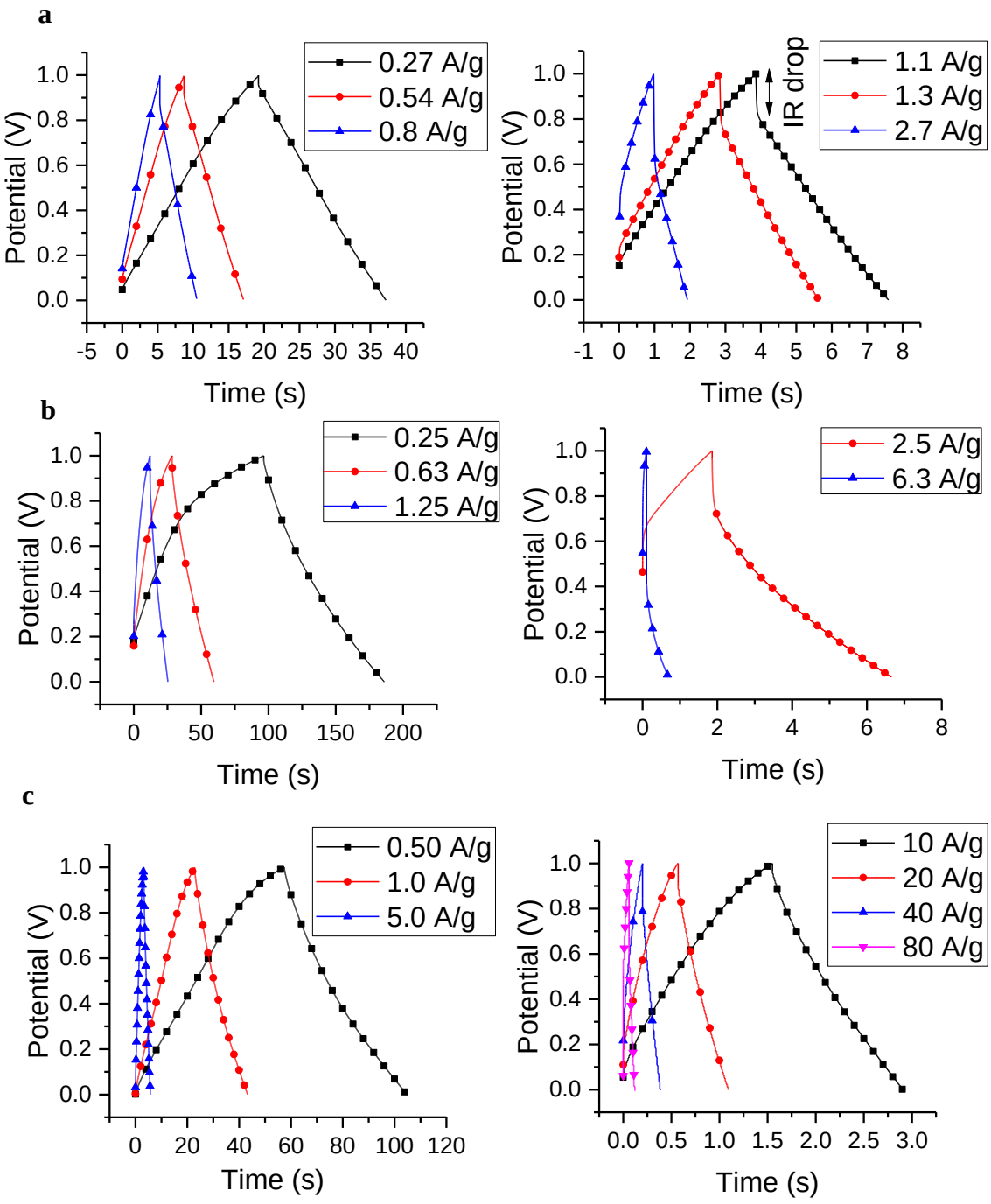

Figure 3-4. CC measurements of the three buckypaper electrodes with KOH electrolyte, a) FWNT, b) SWNT, c) HS-SWNT.

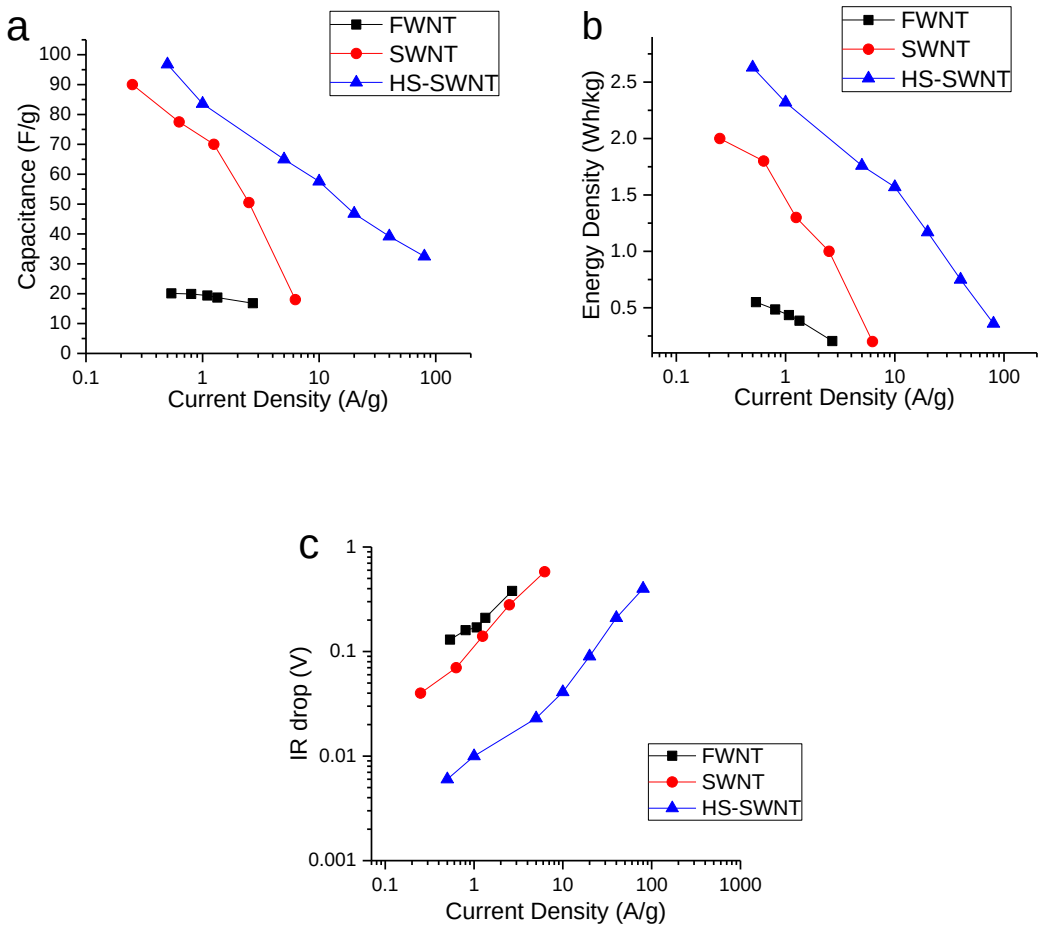

Figure 3-5. Evaluation of the electrochemical performance of FWNT, SWNT and HS-SWNT electrodes in KOH electrolyte. (a) Specific capacitance as a function of current density. (b) Energy density as a function of current density. (c) IR-drop of the electrodes as a function of current density.

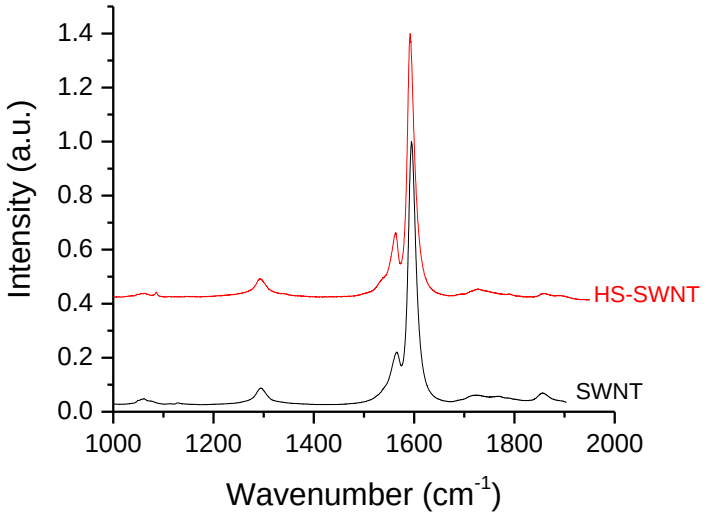

Figure 3-6. Raman spectra of SWNT and HS-SWNT. Normalized to G band intensity and shifted vertically for clarity. G/D ratio in both spectra is ~11.

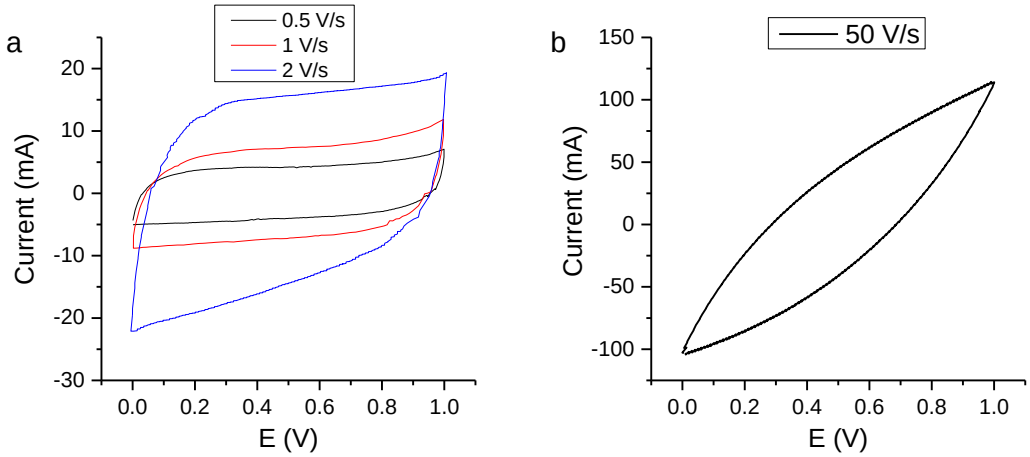

Figure 3-7. Cyclic voltammetry of HS-SWNT in KOH electrolyte at various scan rates.

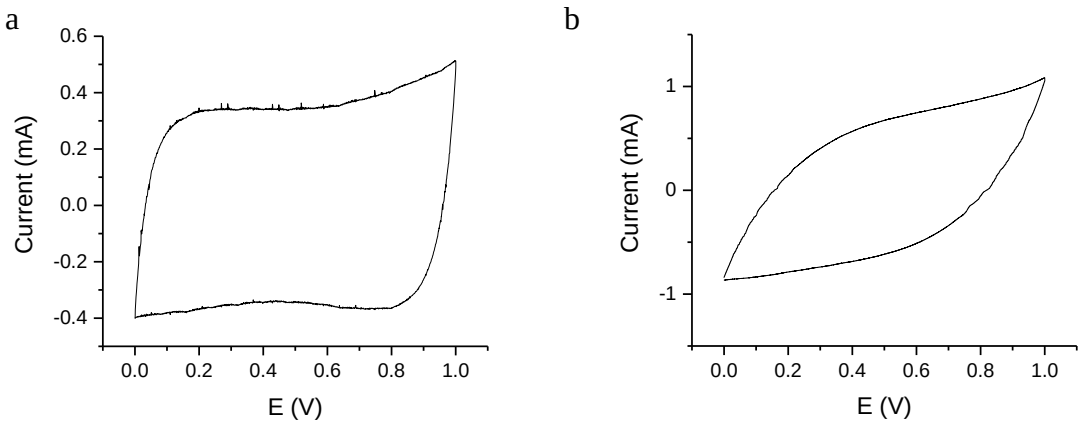

Figure 3-8. CV of (a) FWNT and (b) SWNT at 100 mV/s in KOH electrolyte.

For EDLCs, if the entire surface area is accessible, then capacitance should increase linearly with SSA. PMMA processing of SWNTs repeatedly produced buckypapers with specific surface area above 900 m^2/g. Measurements of 11 PMMA processed buckypapers yielded an average specific surface area of 943 ± 69 m^2/g. Two trials using PMMA, resulted in buckypapers with surface areas of 805 and 870 m^2/g, and these were also tested for their performance as supercapacitor electrode. Thus in total five electrodes were tested with surface area in the range of 300 to 950 m^2/g, and their specific capacitance as a function of specific surface area are plotted at 5 and 100 mV/s in Figure 3-9, showing reasonable correlation within experimental error. Typical of CNT electrodes, the HS-SWNT displayed excellent capacitance retention after 10000 charge-discharge cycles (Figure 3-10).

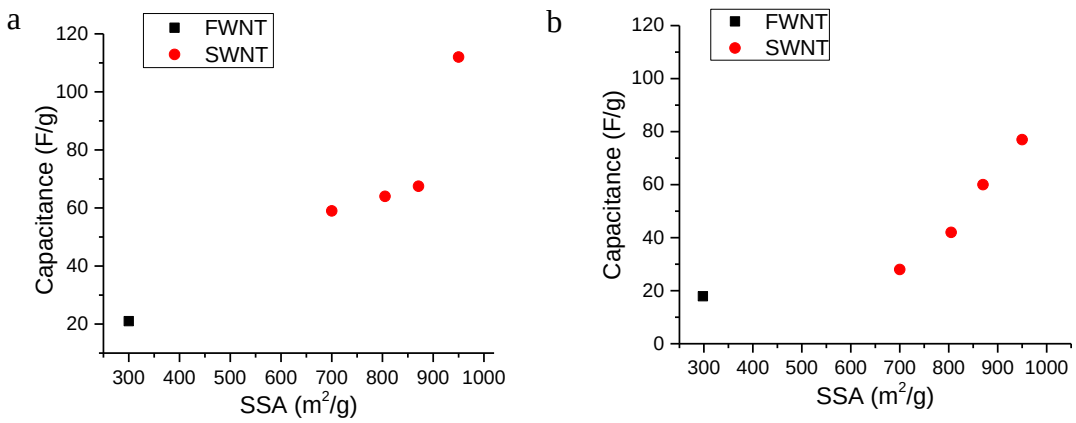

Figure 3-9. Buckypaper capacitance as a function of specific surface area (SSA) measured using 6 M KOH electrolyte at (a) 5 mV/s and (b) 100 mV/s.

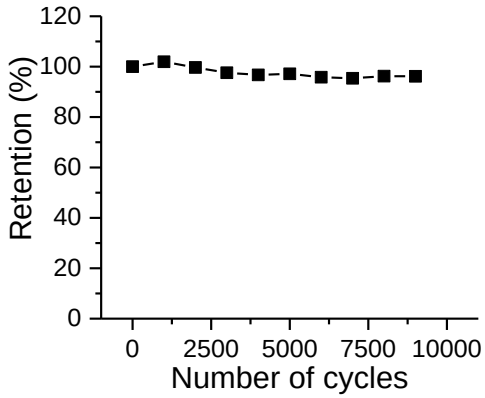

Figure 3-10. Capacitance retention of HS-SWNT electrode with 6 M KOH electrolyte for 10000 charge - discharge cycles. The cell was charged and discharged at a rate of 1 A/g.

3.3.3 Ionic Electrolyte

The HS-SWNT electrode was also tested using ionic liquid electrolyte, $EMIMBF_4$. Ionic liquids enable storage of more energy due to their higher operating potential window, since stored energy scales with square of voltage, $E \alpha V^2$. Constant current plots of HS-SWNT with ionic electrolyte are presented in Figure 3-11, in which the IR drop increases to 1.5 V at 100 A/g. No oxidation peaks are observed in the CV

plots (Figure 3-12). Cycling of the HS-SWNT in ionic electrolyte does not show a reduction in capacitance over 10000 cycles (Figure 3-13). The Ragone plots of the HS-SWNT electrodes based on ionic liquid and KOH electrolyte tests area given in Figure 3-14. As expected, due to large potential window, the energy density is ~9 times higher using the ionic liquid electrolyte than 6 molar KOH electrolyte.

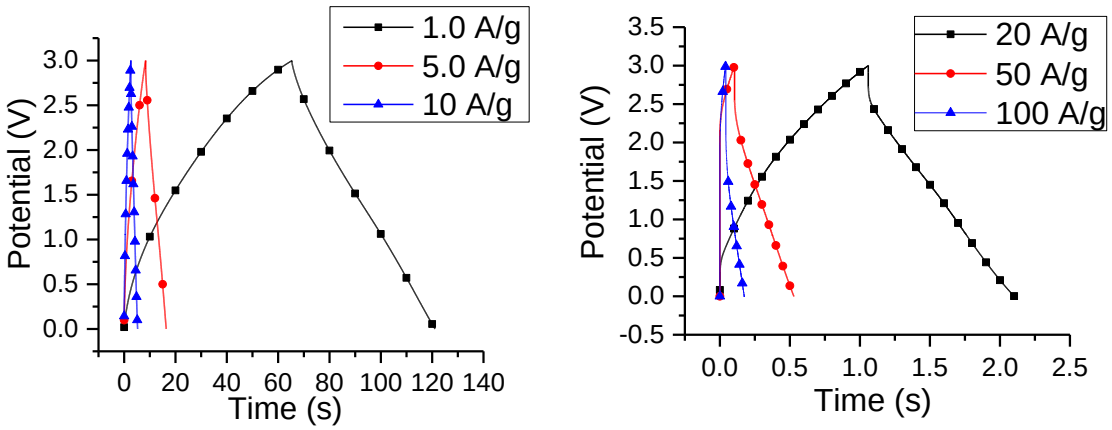

Figure 3-11. CC measurements of HS-SWNT at 1 to 100 A/g currents using ionic liquid electrolyte, $EMIMBF_4$.

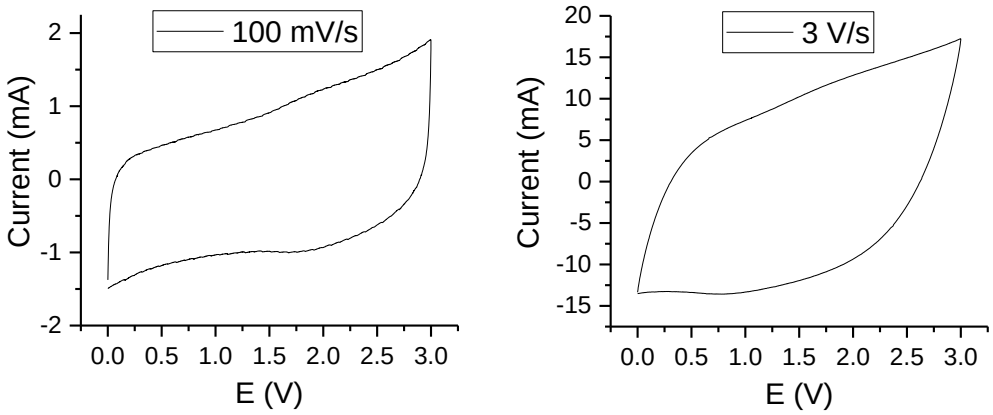

Figure 3-12. CV of HS-SWNT at 100 mV/s and 3 V/s rate in $EMIMBF_4$ electrolyte.

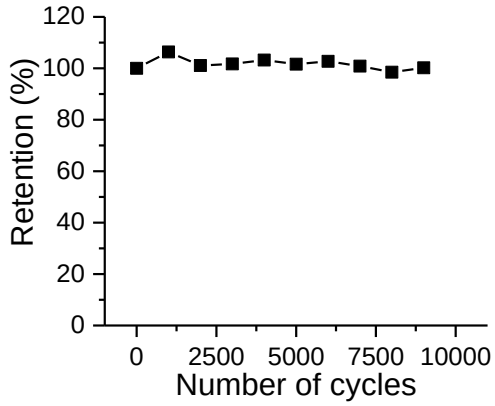

Figure 3-13. Capacitance retention of HS-SWNT electrode with $EMIMBF_4$ electrolyte.

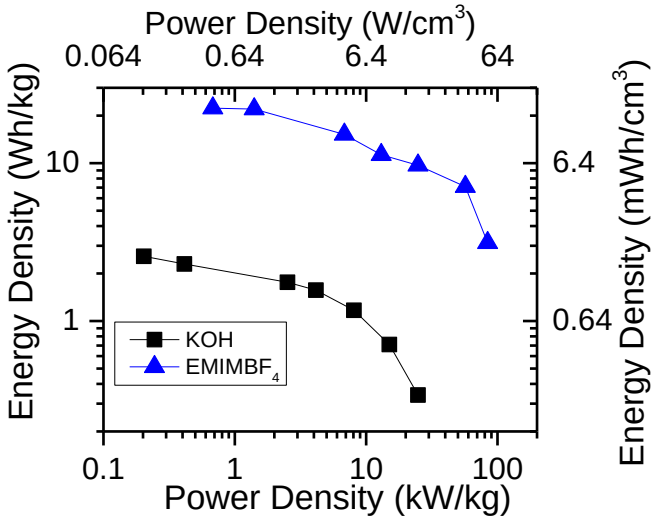

Figure 3-14. Ragone plots (in gravimetric and volumetric units) of HS-SWNT electrodes using 6M KOH and $EMIMBF_4$ electrolytes.

3.3.4 Comparison with Recent CNT and Graphene Supercapacitors

Packaging and size of the energy storage device are important factors. If the volumetric capacitance is too low, then a large electrode volume will be required for storing certain amount of charge. This may not always be practical. Therefore, along with high gravimetric capacitance, a high electrode density is often required. The Density of

the HS-SWNT film was 0.63±0.02 g/cm^3. Since supercapacitors are primarily used for high power applications, the HS-SWNT provides great performance.

In order to demonstrate the performance of the HS-SWNT, a Ragone plot is presented in Figure 3-15, comparing the performance of HS-SWNT with recent best literature data on SWNT and graphene electrodes. This includes a commercial 3.5 V/25 mF activated carbon supercapacitor, CNT/graphene [71] and laser scribed graphene [146] electrodes. The volumetric energy density of HS-SWNT electrode is more than 4 times higher than the previously reported highest energy density (CNT or graphene based supercapacitors with no pseudocapacitance) at the very high power density of 54 W/cm^3, and 6.5 times higher energy density at low power density.

Micro-supercapacitors have gained attention due to their application as power sources in micro-electrical systems. Micro-supercapacitors can also be made using the current technique, as the PMMA wrapped SWNTs can be deposited on any substrate. The simple processing method for achieving high surface area SWNT buckypapers with record high energy and power densities, makes this method an excellent candidate for future commercial applications.

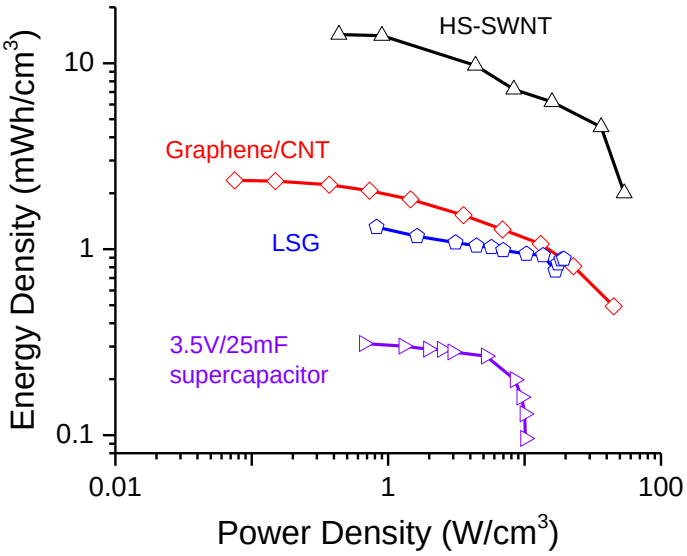

Figure 3-15. Energy and power density of HS-SWNT compared with that of a commercial 3.5 V/25 mF activated carbon supercapacitor (data from [147]), laser scribed graphene (LSG, ionic electrolyte) super capacitor [146], and Graphene/CNT (ionic electrolyte) [71] micro supercapacitor.

3.4 Conclusions

Carbon nanotube supercapacitor electrodes with specific surface area in the range of 300 to 950 m^2/g were fabricated to understand the influence of surface area on energy storage. This was achieved without introducing defects or functionalizing the nanotubes, and thus all the electrodes exhibited no pseudo capacitance. Capacitance exhibited good correlation with specific surface area at low CV rates, but the correlation was relatively poor at high CV rates. The SWNT buckypaper with a surface area of 950 m^2/g (referred to as HS-SWNT buckypaper) exhibited high energy density of 3.13 kWh/kg at a high power density of 84 kW/kg. At a given power density, this energy density is at least four

times higher than the best value reported in the literature to-date for the carbon nanotube electrodes.

CHAPTER 4

THE EFFECT OF POLYMER WRAPPING OF CARBON NANOTUBES ON THE PROPERTIES OF BUCKYPAPERS AND POLY (METHYL METHACRYLATE) COMPOSITE FILMS

4.1 Introduction

Carbon nanotubes (CNTs) have been studied as filler materials in composites for mechanical reinforcement and to introduce functional properties such as electrical conductivity and electromagnetic shielding in composites. Experimental measurements of individual SWNT bundles yielded a tensile modulus of 800-950 GPa and tensile strength of 52-100 GPa [130, 148-150]. While CNT mechanical properties are impressive, load transfer from the matrix to the nanotubes is required, otherwise, they can act as locations for stress concentration and crack formation without increasing modulus. The addition of CNTs to various polymers and its impact on mechanical, viscoelastic and electrical properties has been discussed in detail in literature [22, 49, 103, 151-155]. Different PMMA/CNT preparation methods have been proposed to improve reinforcement by CNTs in composite films [20, 48, 156]. One study suggested multiple melt mixing cycles of SWNTs in PMMA which resulted in better SWNT dispersion as evidenced by optical micrographs [20]. Melt spun fibers from this method resulted in a 150% increase in modulus at 8wt% SWNT content compared to PMMA fibers. Another study used coagulation bath to precipitate the PMMA/SWNT suspension [48]. Melt spun fibers from

the precipitant resulted in a 33 % and 88 % increase in modulus upon addition of 1 wt% and 2 wt% SWNT to PMMA, respectively. Another study pointed out the importance of the nanotube dispersion during in-situ polymerization of PMMA in the presence of CNTs [156]. The addition of surfactant to the MWNT suspension before polymerization led to a 16 % increase in modulus at 6 wt% CNT, while the mechanical properties of the composite without surfactant decreased upon addition of CNTs [156]. Jia et al. reported reduction of tensile strength and toughness of PMMA/CNT composites prepared by in-situ polymerization of PMMA in the presence of CNTs [22]. However, grinding the CNTs in a ball mill and then carrying out polymerization resulted in 30% higher tensile strength and 12% higher impact strength as compared to pure PMMA, which was attributed to improved dispersion upon ball milling of nanotubes.

Incorporation of CNTs in PMMA films has yielded composites with varying properties in previous studies. The increase (or decrease) of modulus and tensile strength of PMMA and composite films are shown in Table 4-1. The low tensile properties of PMMA in ref. [151] and [152] is due to the low molecular weight of PMMA which were even shorter than the nanotube lengths. The CNT reinforced composite films had even lower mechanical properties than neat PMMA films with a molecular weight of 350,000 g/mol. Another study which used dry blending and melt extrusion reported negligible improvement upon addition of unoriented MWNTs [153], while aligning the MWNTs led to a 38% and 25% higher modulus and tensile strength along the CNT direction, respectively. Ref. [154] reported a 130% increase in strain to failure, but no impact on modulus and strength upon addition of 1 wt% SWNTs. Using nitromethane as the solvent has also shown promise for dispersing SWNTs in PMMA [49]. Composite films were

made with two different SWNT purities, 65 wt% and 97.8 wt%, showing the detrimental effect of impurities on tensile strength.

Table 4-1. Mechanical properties and electrical conductivity of PMMA/CNT films in literature. The results of the current study are included for comparison. Values in parenthesis indicate improvement (or decrease) compared to the control samples without SWNT.

CNT (wt%)	Tensile Modulus (GPa)	Tensile Strength (MPa)	Conductivity (S/m)	Comments
10	1.78 (+70%)	23 (-5%)	100	MWNT <90% purity [151], solvent casting
0.25	1.38 (+90%)	37 (+363%)	-	MWNT, in situ polymerization [152]
10	3.7 GPa (+38%)	80 (+25%)	-	MWNT, dry blend and melt extrusion [153], oriented
1	N/A (0%)	44 (0%)	-	Hydroxylamine hydrochloric acid salt treated SWNTs [154]
10	4.4 (+144%)	63 (+26%)	854	SWNT (2.4 wt% impurity), sonicating and stirring [49]
	4.1 (+127%)	23 (-54%)	1430	SWNT (35 wt% impurity), sonicating and stirring [49]
10	3.2 (+100%)	48 (-11%)	26	**This work, SWNT (35 wt% impurity)**

Entangled carbon nanotubes form a freestanding film referred to as buckypaper. They have low tensile modulus (~ 1 GPa) and strength (~15 MPa) despite the high tensile properties of CNTs, due to weak van der Waals interaction at the CNT-CNT junctions, which results in slipping of CNTs during deformation. The challenge is to improve the inter-bundle interaction and prevent slippage of CNTs at low stresses. A summary of previous efforts to improve the mechanical properties of buckypapers is presented in Table 4-2. One study investigated the effect of several parameters, such as sonication time, type of surfactant or biopolymer, membrane filter material [157]. Buckypaper modulus increased by 94% when cellulose nitrate (CN) was used instead of polytetrafluoroethylene (PTFE) membrane, but no explanation was provided as to why the properties improve with the type of membrane. In another work, the buckypaper was

coated with polypyrrole (PPy) by potentioamperometric polymerization of pyrrole onto the CNT network [158]. The buckypaper was then immersed into cyanate ester (CE) resin and processed to make SWNT-PPy-CE buckypaper. The mechanical properties of the SWNT-PPy-CE improved significantly compared to the control buckypaper as shown in the table. While the mechanical properties of BP-CE and BP-PPy buckypapers was higher than the control SWNT buckypaper, the properties were lower than BP–PPy-CE. This enhancement was attributed to improved interactions between nanotubes in the intra-bundle as PPy chains wrap the bundles and individual nanotubes, although there was no discussion on how it improved inter-bundle strength. It was also argued that the PPy bridge between CNTs and CE improved the network strength. Infusing buckypapers with polycarbonate (PC) resulted in an increase in modulus and tensile strength [159, 160]. In another study, mechanical properties of the buckypaper improved as SWNTs were refluxed with stronger acids used up to 10 M nitric acid concentration [161]. SEM images indicate a reduction in bundle diameter at higher acid concentrations, as acid treatment of aqueous suspensions improves the dispersion of SWNTs.

Table 4-2. Properties of buckypapers reported in literature and the current study. Values in parenthesis indicate improvement compared to control SWNT buckypapers.

Buckypaper	CNT (wt%)	Modulus (GPa)	Strength (MPa)	Conductivity (S/m)	Comments
SWNT [157]	100	1.6	15.7	12700	5 µm PTFE, Triton X-100
SWNT [157]	100	3.1 (+94%)	35.0 (+123%)	10600 (-17%)	0.2 µm CN, Triton X-100
SWNT [158][1]	100	3.3	14.3	19600	Pristine SWNTs
SWNT-PPy-CE [158]	73	17.8 (+493%)	68.7 (+380%)	17100 (-13%)	PPy wrapped SWNTs
SWNT [159]	100	2.3	6.5	20410	Pristine SWNTs
SWNT/PC2 [159]	48	5.1 (+122%)	18.9 (+190%)	12350 (-40%)	Polycarbonate infiltrated BP
SWNT [161]	100	0.8	10	30000	Pristine SWNTs
10 M HNO_3 SWNT [161]	100	5.0 (+525%)	74 (+640%)	12000 (-60%)	Acid treated buckypapers
SWNT	100	1.1	16	10000	**This work**
SWNT/PMMA	65	6.5 (+490%)	59 (+269%)	1100 (-89%)	**This work**

[1] Tensile modulus is more than typically reported values for pristine buckypapers.

To gain better understanding of the reinforcement mechanism of CNTs in composites, CNT stress can be monitored during composite deformation. CNTs exhibit stress induced Raman band shifts [130, 162]. Stretching and weakening of the carbon-carbon bond of the nanotubes results in downshift of the D, G and G' bands, while G' band shows the most shift [163] and is typically used to monitor stress transfer from the polymer to the nanotubes [125].

In this study, using a technique described elsewhere [164] to helically wrap SWNTs with PMMA, films and buckypapers with and without PMMA wrapping were made and the effect of PMMA wrapping on the stress transfer from the matrix to the nanotubes was investigated. The PMMA wrapping greatly improved SWNT dispersion, and individualized SWNTs in buckypapers and composites films. The debundling and isolation of SWNTs improved stress transfer to the SWNTs, which in turn led to better mechanical properties.

4.2 Experimental

4.2.1 Materials

HiPCO^{TM} raw SWNTs (65 % purity) and purified SWNTs (grade sp300, average diameter 0.93 nm, purity 98%) were obtained from Carbon Nanotechnologies, Inc. Dimethylformamide (ACS grade, 99.8% purity) and PMMA (M_w= 350,000 g/mol) polymer was purchased from Sigma Aldrich. PTFE membrane (Zefon International, FPTPT147) with 1 μm pore size was used for the filtration.

4.2.2 Sample Preparation

Two types of PMMA/SWNT composite films were prepared, one set with PMMA wrapping and another set without PMMA wrapping, with 0.1 to 10 wt% SWNT content. The non-wrapped PMMA/SWNT was prepared by sonicating SWNTs (Branson 3510R-MT, 100 W, 42 kHz), 0.15 (0.1 wt%), 1.5 (1 wt%), 7.5 (5 wt%) and 15 mg (10 wt%), in 15 mL DMF for 24 hours, then adding PMMA to obtain a solid content of 150 mg and mixed by stirring for 12 hours. The wrapped PMMA/SWNT films were prepared by sonicating SWNTs in DMF in the presence of PMMA with a 1:1 PMMA to SWNT weight ratio for 24 hours. Then the remaining amount of PMMA is added to obtain a solid content of 150 mg and mixed by stirring for 12 hours. The suspensions were cast in a glass mold to form ~40 μm thick films. The films were dried at 65 ºC under vacuum for 24 hours. The SWNT buckypaper suspension was prepared by sonicating 12.3 mg of unpurified SWNTs (8 mg SWNTs) in 400 mL DMF for 24 hours. The PMMA-wrapped SWNT suspension was prepared by sonicating 12.3 mg of unpurified SWNTs with 8 mg of PMMA in 50 mL of DMF for 24 hours. Buckypapers were made by vacuum filtration of the suspensions, with subsequent wash with MeOH, and were then peeled off from the filter and dried. The purified tubes were used only for the 0.1 wt% SWNT film and the rest of the samples were made with the raw nanotubes.

4.2.3 Characterization

Scanning electron microscopy (SEM) was performed on a Hitachi SU8010 at an accelerating voltage of 5 kV. Tensile measurements and dynamic mechanical analysis (DMA) were carried out by RSA III (Rheometrics Scientific) solid analyzer equipped

with a linear tension clamp. The tensile test samples had a width of ~2 mm. The gauge length and the strain rate for the tensile tests were set at 10 mm and 0.50 %/s, respectively. The thickness of the films and buckypaper samples were ~40 μm and ~20 μm, respectively. Dynamic mechanical properties as a function of temperature were determined at 1 Hz frequency, with static force adjusted to be 20 % larger than dynamic force. Raman spectra were obtained using a 785 nm laser on a HORIBA XploRA Raman Microscope System. Raman spectra were collected during film deformation at a gauge length of 10 mm by straining 2 mm thin strips using a stretching rig. The Raman spectra were collected using parallel (VV) polarizers with the straining direction parallel to the polarizer and analyzer directions. Infrared spectra (IR) were collected with a Perkin Elmer Spectrum One infrared microscope. Electrical conductivity of various SWNT films was measured by a standard four-point probe configuration (Signatone).

4.3 Results and Discussions

4.3.1 Effect of PMMA Wrapping on SWNT Aggregation and Dispersion in Films and Buckypapers

Wrapping the SWNTs with PMMA greatly increases dispersion quality in DMF. Images (Figure 4-1) and optical micrographs (Figure 4-2) of the PMMA/SWNT films clearly show the effect of wrapping on film quality and SWNT aggregation. Non-wrapped SWNTs phase separate into distinct islands at 0.1 wt% SWNT content. Such phase separation was visible in the 1 wt% non-wrapped SWNT films (Figure 4-3), though they did not aggregate into separate islands as in the 0.1 wt% SWNT film. The 5 and 10 wt% non-wrapped SWNT films were completely opaque and PMMA rich regions were

not visible demonstrating better homogeneity than 0.1 and 1 wt% non-wrapped SWNT films. The addition of PMMA during sonication leads to wrapping, which prevents SWNT aggregation upon adding PMMA and stirring, while the non-wrapped SWNTs are free to aggregate upon stirring.

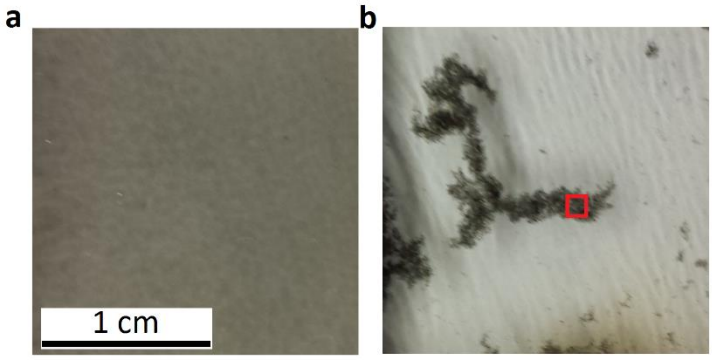

Figure 4-1. Photographs of 0.1 wt% SWNT films, with a) wrapped, and b) unwrapped SWNTs. SWNTs aggregate into small islands when they are not wrapped with the polymer. The scale bar applies to both images. The red box outlines the section from which the optical micrograph was taken in Figure 4-2b.

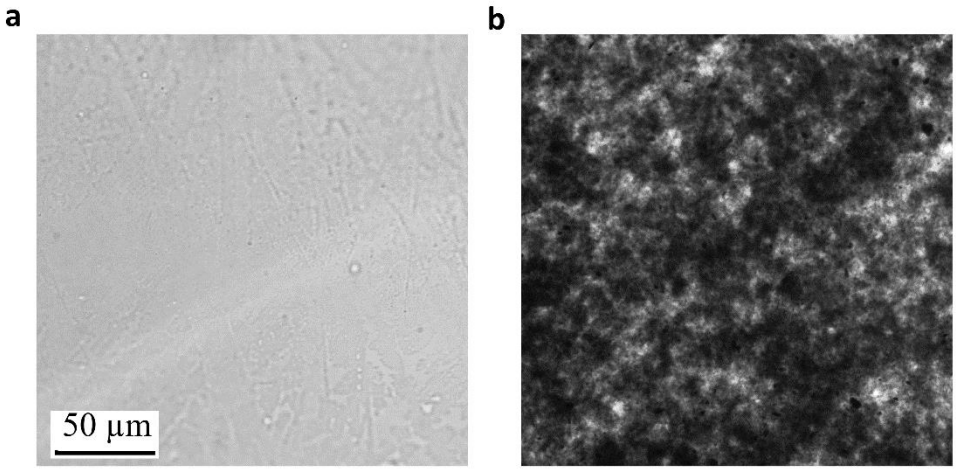

Figure 4-2. Optical micrographs of 0.1 wt% SWNT films, a) wrapped SWNTs b) non-wrapped SWNTs.

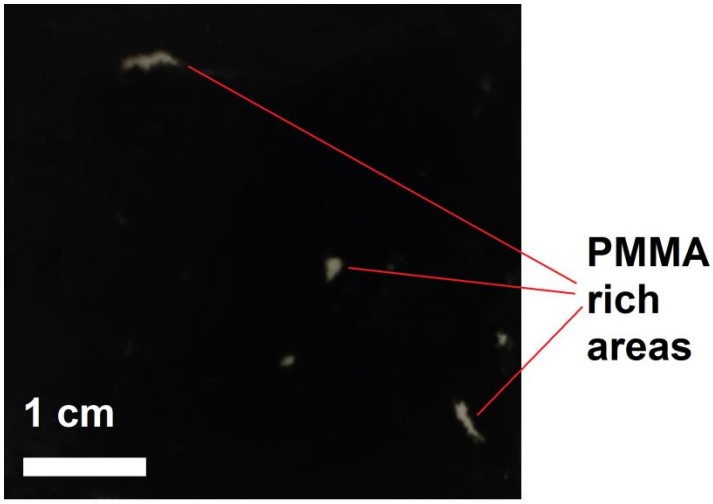

Figure 4-3. Non-wrapped 1 wt% PMMA/SWNT film, with numerous PMMA rich regions indicating phase separation.

Raman spectroscopy is a useful characterization tool for SWNTs. SWNTs that have bandgaps close to the exciting laser energy are probed. The resonance energy of carbon nanotubes red shifts upon bundling, causing the nanotubes to go in resonance or off resonance based on their band gap energy relative to the laser energy, making it a beneficial tool to monitor bundling [138, 140]. The Raman spectra of the wrapped SWNT films indicated debundled SWNTs from the radial breathing mode (RBM), while the RBM mode of the non-wrapped SWNTs indicates aggregated SWNTs (Figure 4-4). The RBM at 268 cm^{-1} corresponds to nanotube (10,2). Upon bundling (10,2) bandgap energy approaches the laser energy and the intensity of that RBM peak increases. The opposite happens for the three other RBM peaks as shown in Figure 4-4, because the band gap energies approach the laser energy when the SWNTs are individualized. Interestingly, all of the wrapped SWNT films and buckypapers followed this behavior, regardless of SWNT content, while the non-wrapped SWNTs in the films and buckypapers indicated

aggregation. This confirms that the state of aggregation or bundling is independent of CNT loading.

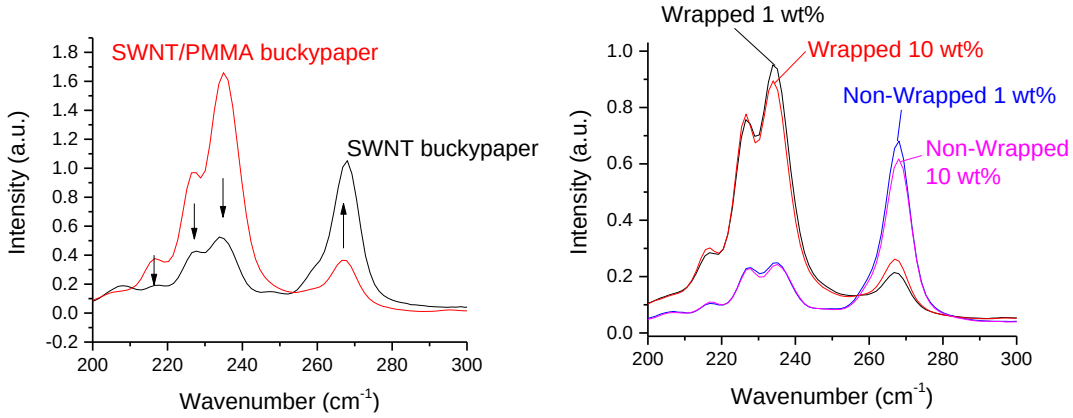

Figure 4-4. Raman spectra of SWNT and SWNT/PMMA (65 wt%/35 wt%) buckypapers and PMMA/SWNT films, normalized to G band intensity. The arrows show the direction of intensity upon bundling.

4.3.2 Effect of PMMA wrapping on the Mechanical Properties of Buckypapers and Films

Buckypapers and films are essentially different types of composite material from stress transfer point of view because of their structural architecture. In the films, the polymer matrix surrounds CNTs and stress is transferred from the matrix to the nanotubes at the CNT-polymer interface. In the buckypapers, stress is transferred through the entanglements or CNT junctions. PMMA wrapping, which consisted ~35 wt% of the SWNT/PMMA buckypaper, resulted in better mechanical properties in buckypapers (Table 4-3). The modulus and tensile strength of the SWNT/PMMA buckypaper was 5.9 and 3.7 times that of the SWNT buckypaper, respectively. The tensile properties of the

wrapped SWNT films were generally better than the non-wrapped films as shown in Table 4-4. The non-wrapped 1 wt% film had lower mechanical properties compared to the PMMA film due to visible inhomogeneities (Figure 4-3). The large mismatch between the stiffness of CNT rich areas compared to parts of the composite with less CNTs leads to larger deformation in parts of the composite with lower stiffness. This simply means that the effective cross section of deformation is smaller in a non-homogeneous structure. This causes an earlier onset of failure and lower tensile properties, which could explain the lower modulus and strength of 1 wt% non-wrapped SWNT film. While the SWNTs in the non-wrapped 5 and 10 wt% SWNT film are aggregated on a nanoscale similar to the aggregates formed in the 0.1 and 1 wt% non-wrapped SWNT films, the films are completely opaque with no PMMA rich regions visible. For the PMMA wrapped films, tensile strength peaks at 1% SWNT and decreases at higher SWNT loadings. For the non-wrapped SWNT films tensile strength is reduced by 45 percent at 1 wt% SWNT and increases at higher SWNT loadings but remains below the strength of neat PMMA film. The 1 wt% non-wrapped film has very low tensile properties due to its inhomogeneity coupled with the impurities. The high impurity of the SWNTs (35 wt%) may be the main reason of the reduction of tensile strength and elongation at break. The impurities which are ~4 nm, can be detrimental to the structure (Figure 4-5). Comparison of these results to those in Table 4-1 show that only the composites processed with nitromethane have higher improvement of mechanical properties [49]. In this work, non-wrapped carbon nanotubes aggregated and precipitated without exception during stirring, while no aggregation was observed in [49]. It is possible that the SWNTs may have also been wrapped with PMMA in [49]. The

specific modulus of SWNT/PMMA buckypapers with a specific density of ~0.74 gm/cm^3 (neglecting the mass of metallic impurities) is 8.8 GPa/g/cm^3. For comparison, an isotropic T300/N5208 carbon fiber epoxy composite laminate (E_1= 151, E_1= 10.3 GPa, density 1.52 g/cm^3), with a symmetric 0/45/-45/90 ° lay-up is ~40 GPa/g/cm^3. Mechanical reinforcement of PMMA fibers by MWNTs is presented in Appendix A.

Table 4-3. Tensile properties of buckypapers of SWNT and SWNT/PMMA (65 wt%/35 wt%) buckypapers.

Buckypaper	Modulus (GPa)	Tensile Strength (MPa)	Elongation at break (%)
SWNT	1.1 ± 0.2	16 ± 3	1.8 ± 0.9
SWNT/PMMA	6.5 ± 0.4	59 ± 12	1.4 ± 0.5

Table 4-4. Tensile properties and G' band shift of PMMA/SWNT films (stress-strain plots provided in Figure 4-6).

SWNT content	Modulus (GPa)		Tensile Strength (MPa)		Elongation at break (%)	
	wrapped*	non-wrapped	wrapped	non-wrapped	wrapped	non-wrapped
0 % (PMMA)	1.6 ± 0.1		54 ± 10		8.4 ± 3	
0.1 % *	1.8 ± 0.2	-	47 ± 3	-	9.7 ± 1.8	-
1 %	2.1 ± 0.2	1.2 ± 0.1	60 ± 3	30 ± 6	9.6 ± 2.2	3.4 ± 0.9
5 %	2.5 ± 0.2	1.9 ± 0.1	54 ±2	46 ± 8	5.3 ± 0.4	5.2 ± 1.2
10 %	3.2 ± 0.4	2.6 ± 0.3	48 ± 8	47 ± 7	1.9 ± 0.3	2.6 ± 0.7

* Purified SWNTs

* Wrapped: samples prepared with PMMA wrapping on CNT. Non-wrapped: samples prepared with no PMMA wrapping.

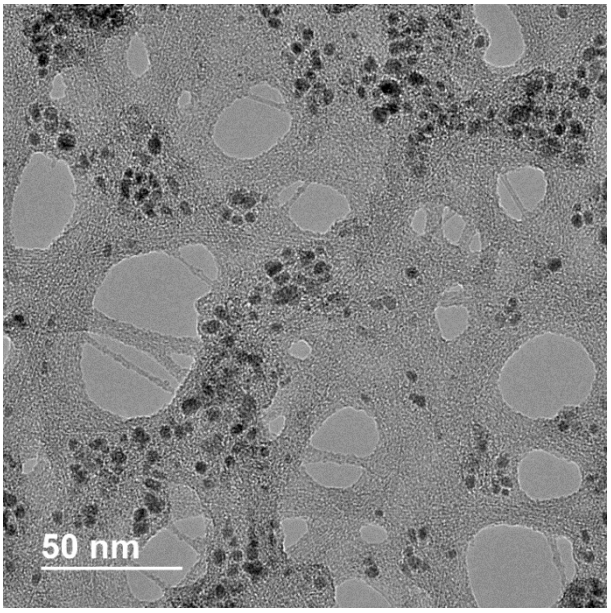

Figure 4-5. TEM image of SWNTs showing the size of impurities.

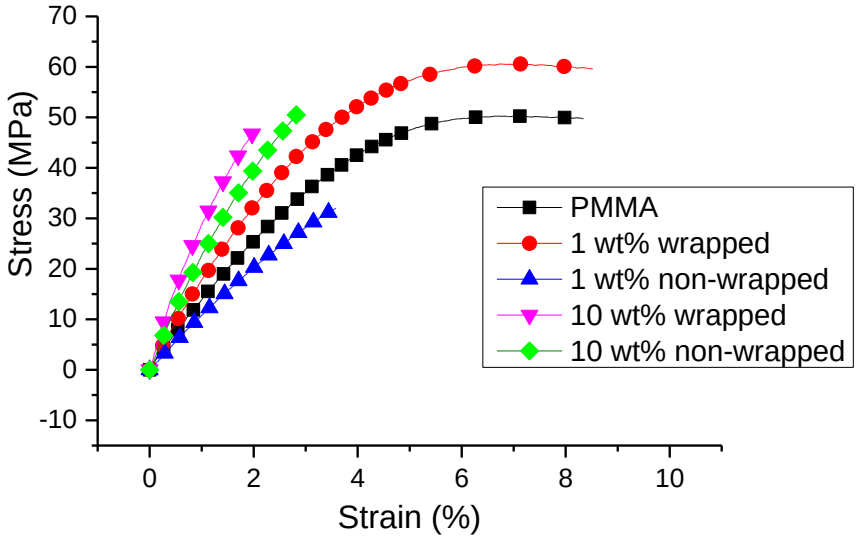

Figure 4-6. Stress-strain curves of PMMA composite films.

4.3.3 Micromechanical Model of SWNT Reinforcement

Halpin-Tsai [165] and shear-lag model [86] have been proposed to predict the mechanical properties of fiber reinforced composites. A modified Cox model is used to estimate the modulus of the composite, E_c, using the rule of mixtures [166-169]. This particular model is used because it captures the effect of length, waviness and random orientation of SWNTs in the composite:

$$E_{\mathrm{c}} = E_{\mathrm{CNT,eff}}.V_{\mathrm{CNT}} + E_{\mathrm{m}}.(1 - V_{\mathrm{CNT}})$$

$$E_{\mathrm{CNT,eff}} = E_{\mathrm{CNT}}.k_0.k_1.k_2$$

$$k_2 = 1 - \frac{\tanh\left(\beta\frac{l}{d}\right)}{\beta\frac{l}{d}}$$

$$\beta = \sqrt{\frac{E_{\mathrm{m}}}{E_{\mathrm{CNT}}.(1+v_{\mathrm{m}}).\ln\left(\sqrt{\frac{2.\pi}{V_{\mathrm{CNT}}.\sqrt{3}}}\right)}}$$

E_{CNT}, V_{CNT}, l, d are the CNT modulus, volume fraction, length and diameter respectively. E_{m}, v_{m} are the polymer matrix modulus and Poisson ratio ($v_{\mathrm{m}} = 0.33$), respectively. Assuming the SWNTs are mainly individualized upon polymer wrapping, d=0.93 nm and l/d =500 (approximate length from ref. [11]) and E_{CNT}= 760 GPA [170]. $E_{\mathrm{CNT,eff}}$ is the effective modulus of the CNT which takes into account CNT orientation factor, k_0, waviness, k_1, and length, k_2, factors. For randomly oriented three dimensionally isotropic CNTs in the matrix, k_0=0.2 [162]. Waviness can affect the

effective CNT length and modulus. CNT waviness can vary based on the type of nanotube and processing. Assuming an individualized SWNT state in the PMMA wrapped SWNT (*l/d* =500), the waviness factor is fitted using the data k_1=0.25 (Figure 4-7). Using the same k_1 value, the non-wrapped composite modulus is fitted to obtain *l/d* =85, indicating ~6 times larger bundle diameter in the non-wrapped films compared to the wrapped SWNT composite films.

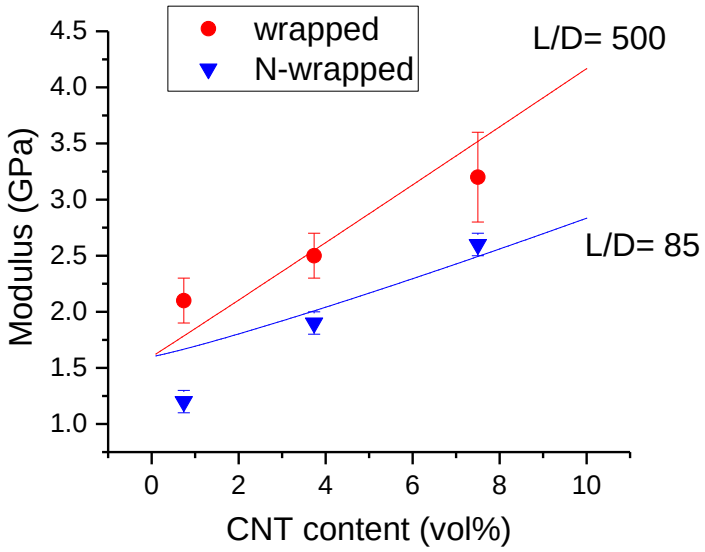

Figure 4-7. Experimental data (discrete data points) and the micromechanical model (fitted line).

4.3.4 Effect of PMMA Wrapping on Stress Transfer to SWNTs

By monitoring the G' band shift during straining of the buckypapers (Figure 4-10), no significant change in G' band position of the SWNT buckypaper was observed. The stress is transferred through van der Waals interaction between the nanotubes in the

buckypaper. In addition to the RBM Raman intensities, surface area measurements indicate larger bundles in the SWNT buckypaper compared to the SWNT/PMMA buckypaper [164]. This means that for the same amount of nanotubes there are less bundles and fewer discrete contact points in SWNT buckypaper compared to SWNT/PMMA buckypaper (Figure 4-11). The weakest component fails upon straining the buckypaper. In this case, slippage occurs at the nanotube-nanotube interface. Slippage is unlikely to occur between nanotubes in a bundle since the continuous nanotube interface between nanotubes in a bundle is much larger than discrete contact points, resulting in slippage occurring at CNT cross over points. To delay the onset of slipping, discrete contact points should be maximized, which can be achieved by complete individualization of the CNTs. When SWNT/PMMA buckypaper is strained, stress is transferred through the many crossover points in the entangled structure to individual SWNTs. This allows sufficient stress to be transferred to the nanotubes to induce measurable G' Raman band shift. However, when there are fewer crossover points, the bundles slip before adequate stress is experienced by the CNTs in the bundle, resulting in negligible G' Raman band shift.

Alternatively, the improved mechanical properties may be directly due to the polymer wrapping. This might be due to better adhesion between PMMA-PMMA side chains compared to SWNT-SWNT interaction, or the nano-ridges created by the helical wrapping on SWNTs (Figure 4-8). Another hypothesis is that individual PMMA chains are likely to wrap multiple SWNTs. This allows the polymer to link multiple SWNTs together and prevent their slipping at low stress (Figure 4-9).

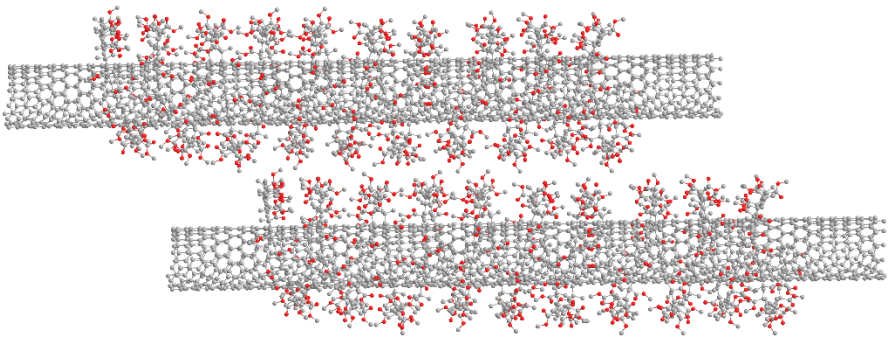

Figure 4-8. Schematic of two helically wrapped SWNTs. PMMA wrapping may improve mechanical properties due to improved interaction from the side chains of PMMA.

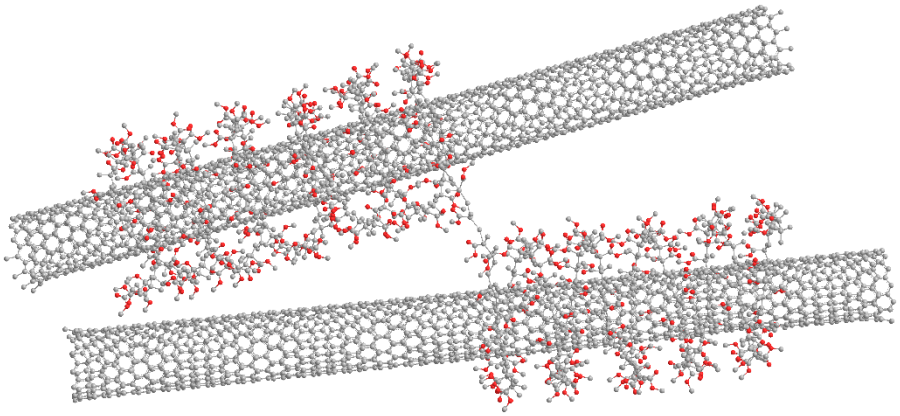

Figure 4-9. Schematic representation of a single PMMA chain wrapping two SWNTs and linking them together.

To measure the strain/stress of the nanotubes irrespective of the slippage that is occurring, the G' Raman band shift rate of individual semiconducting SWNTs of 37.3 cm^{-1}/% strain is used. This value has been determined by straining individual SWNTs using atomic force microscopy and measuring the G' Raman band shift [127]. The strain experienced by individual nanotubes can be expressed as $\varepsilon_i = S_m/37.3$ %, where S_m is the maximum G' band shift. For the SWNT/PMMA buckypaper when the buckypaper is strained at 0.77 %, S_m =5 cm^{-1} (Figure 4-10), so the strain on individual tubes is ε_i=0.14 % (corresponds to σ_i=1.06 GPa, considering SWNT modulus 760 GPa (from ref. [170]

considering an average SWNT diameter of 0.93 nm [171]). The rest of the strain comes from slipping of the nanotubes and straightening out of the curvatures.

The effect of straining on the G' band shift of 1 wt% wrapped SWNT film is shown in Figure 4-12. In addition to the downshifting of the G' band shift, upshift of a peak not previously observed in PMMA or SWNTs were observed. The improvement of modulus upon addition of CNTs in a polymer matrix requires stress transfer to CNTs. The higher the strain/stress transferred from the matrix to the nanotubes, the higher the composite modulus. Fortunately, Raman spectroscopy can also be used to monitor the G' band shift in the films during deformation as shown in Figure 4-13. The maximum band shift is related to the maximum amount of stress that can be transferred to the nanotubes. The nanotube-PMMA interface fails when the G' band shift plateaus; as the matrix is being strained the nanotubes are not further strained significantly. The 10 wt% wrapped film exhibits the highest Raman band shift S_m=15.4 cm^{-1}, which corresponds to a stress of σ_i=3.14 GPa in the SWNTs. This is contrary to the work on polyacrylonitrile/CNT fibers [125] where a larger Raman band shift was observed at lower SWNT concentrations which was attributed to dispersion quality. As supported by the Raman RBM intensity, increasing SWNT concentration does not negatively affect the SWNT dispersion or bundle size in the composite films. As long as the bundle size is similar in the composites, there is no reduction in stress transfer at higher SWNT concentrations, resulting in similar stress transfer to SWNTs. All of wrapped SWNT films have higher maximum band shift, S_m, compared to the non-wrapped SWNT films. This is likely due to better dispersion on the nanoscale supported by the RBM intensities (Figure 4-4).

The maximum G' Raman band shift is larger in the composite films compared to the buckypapers. This difference can be explained by distinguishing how stress is transferred to the nanotubes in the composite and the buckypapers. In the films, stress is transferred through the continuous PMMA-SWNT interface along the whole length of the nanotube (Figure 4-14). Meanwhile, stress is transferred through discrete nanotube-nanotube interface in the SWNT/PMMA buckypaper (Figure 4-11).

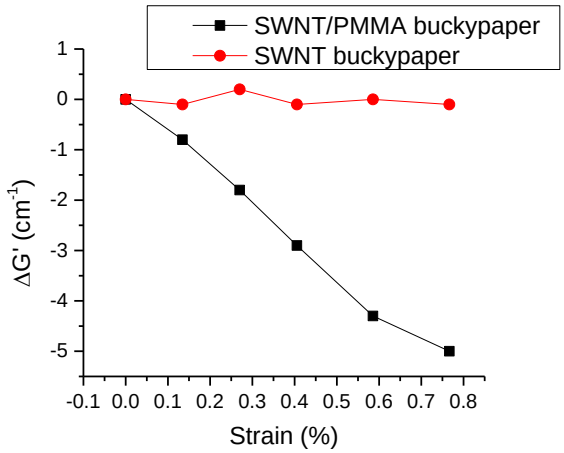

Figure 4-10. G' band peak position of the SWNT and SWNT/PMMA (65 wt%/35 wt%) buckypapers upon straining.

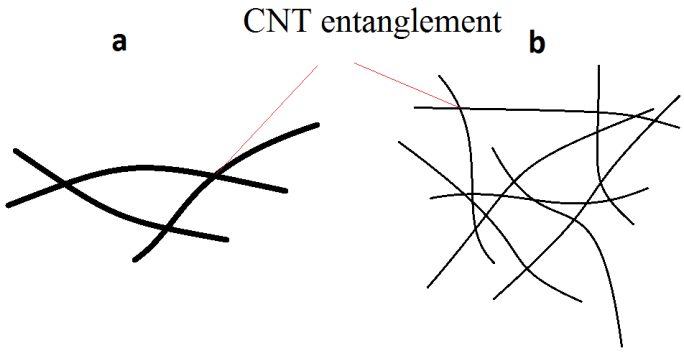

Figure 4-11. Nanotubes in a) bundled, and b) individualized state. There are more entanglements in the individualized state compared to the bundled state. The higher number of entanglement points improve stress transfer.

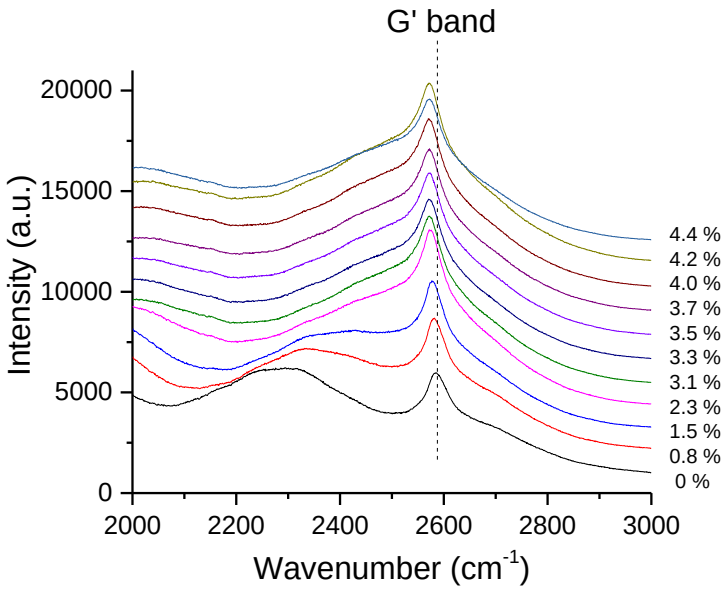

Figure 4-12. Raman spectra of 1 wt% wrapped PMMA/SWNT film at different strains. Plots have been shifted vertically for clarity. Vertical dotted line indicates position of G' band at 0% strain.

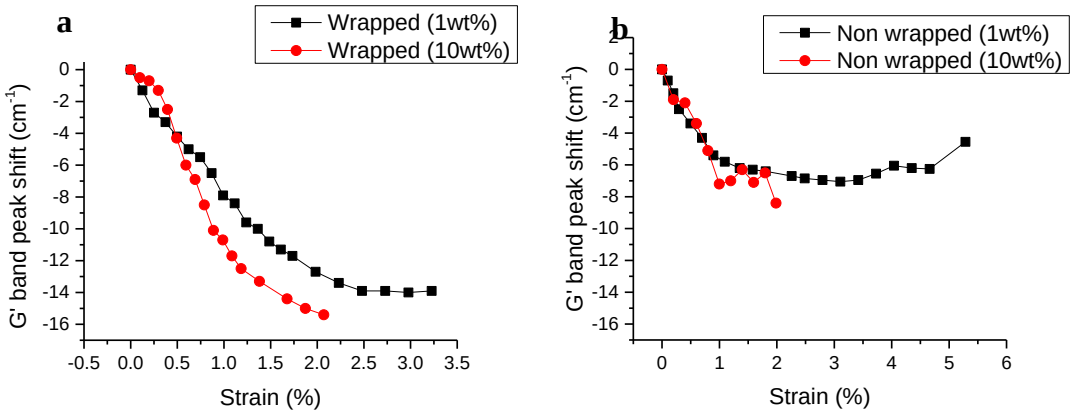

Figure 4-13. G' band shift of different films under straining conditions. a) wrapped PMMA/SWNT film, b) non-wrapped PMMA/SWNT films.

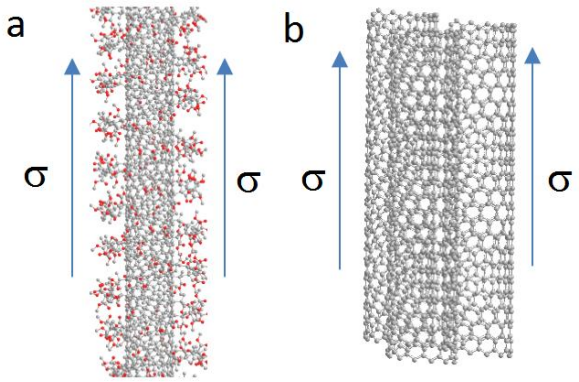

Figure 4-14. Stress transfer from the matrix to a) individual SWNT wrapped with PMMA, and b) SWNT bundle.

Apart from the influence of PMMA wrapping on the RBM, there are several additional distinct features which appear upon PMMA wrapping as shown in Figure 4-15. The first feature is a broad peak from 1000-3000 cm^{-1}, which can be seen in 1 wt% wrapped SWNT films and the SWNT/PMMA buckypaper. Another feature was an additional broad peak at 2276 cm^{-1}, which exist in all of the wrapped films, but not in the SWNT/PMMA buckypapers and non-wrapped films at this SWNT loading. The new peaks do not originate from PMMA (Figure 4-16). At 10 wt% SWNT loading, the peak still appears in the wrapped films (Figure 4-17), but it also appears in some of the non-wrapped composite films but not all of them (Figure 4-18) albeit at a smaller intensity. The peak also exists in 0.1 wt% wrapped film Raman spectrum, ruling out influence from impurities (Figure 4-19). From these observations there seems to be an interaction between amorphous and helical PMMA leading to the new peak. When the film is

strained the new peak at 2276 cm^{-1} upshifts (Figure 4-12) and the peak shift plateaus at 1.5% strain as shown in Figure 4-20.

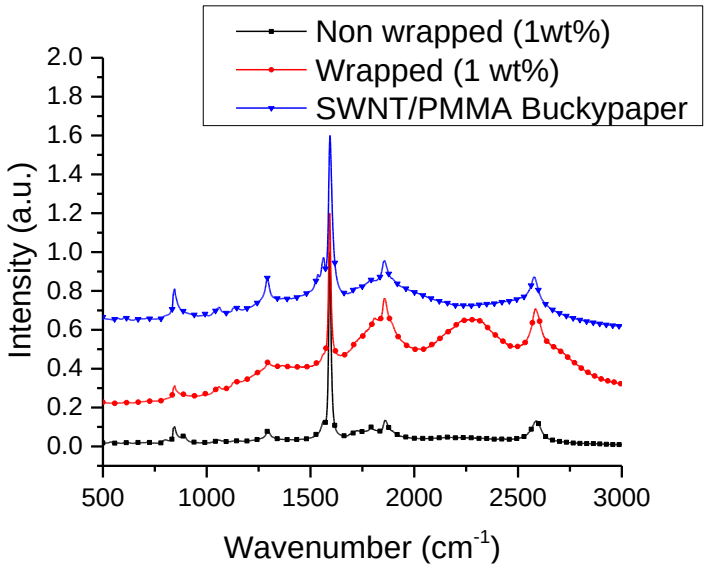

Figure 4-15. Raman spectra of PMMA/SWNT films and buckypapers at 785 nm. Spectra have been normalized to the G band and shifted vertically.

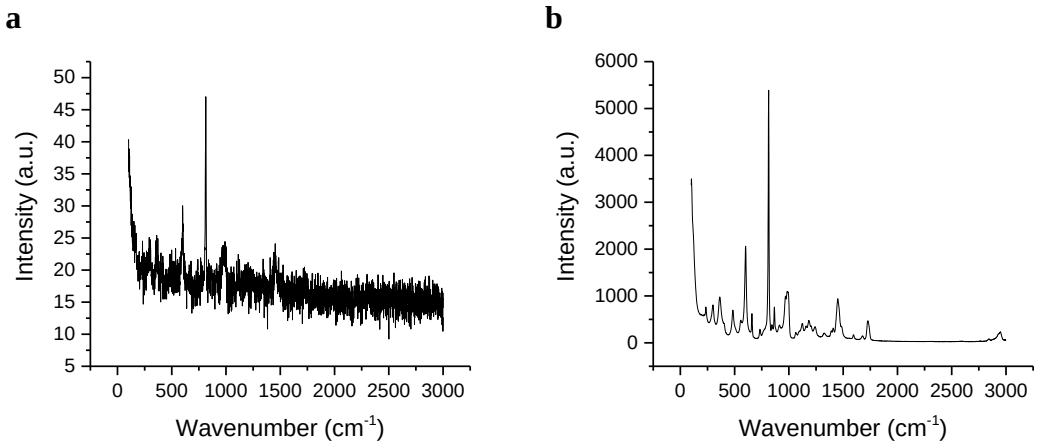

Figure 4-16. Raman spectra of PMMA film at different power and accumulation times: a) same power and accumulation time as the composite films, b) 100 times higher power and 20 times longer accumulation time than PMMA/SWNT film.

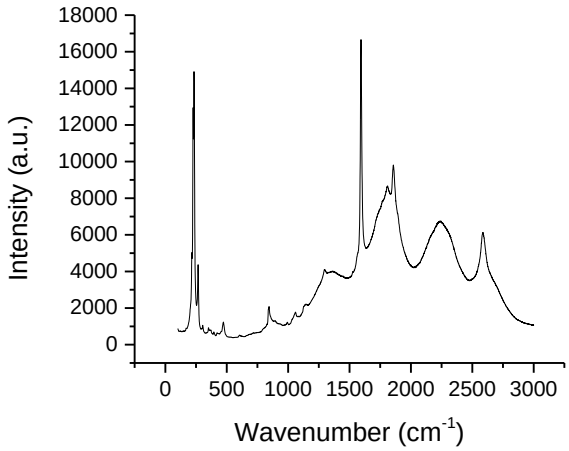

Figure 4-17. Raman spectrum of 10 wt% wrapped composite films.

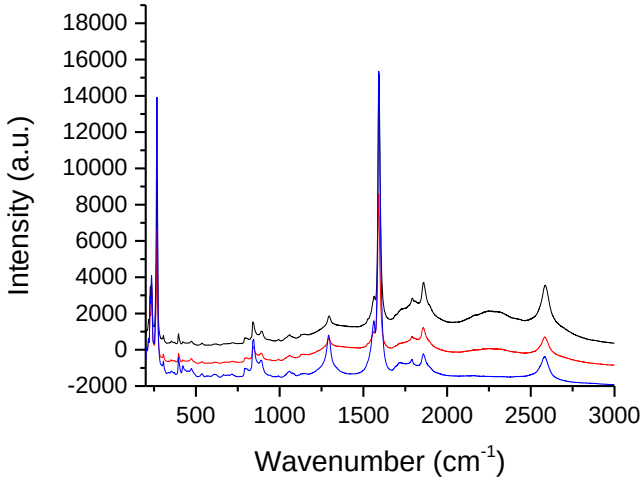

Figure 4-18. Raman spectra of 10 wt% non-wrapped composite films. Some spectra display the peak at ~2300 cm^{-1} while others do not. The new peak intensity is weaker than the G' band intensity in these plots. However, the intensity of this peak in PMMA wrapped SWNT composite films is stronger than the G' band intensity.

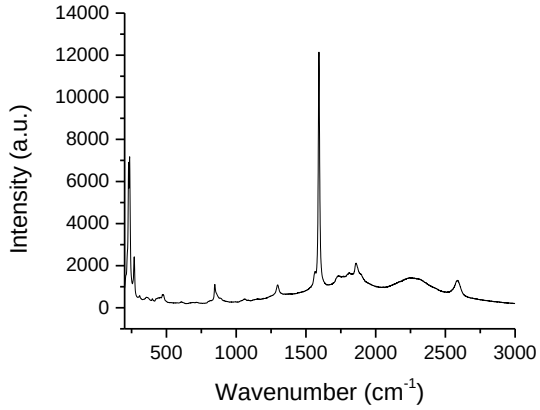

Figure 4-19. Raman spectrum of 0.1 wt% (purified) wrapped composite film.

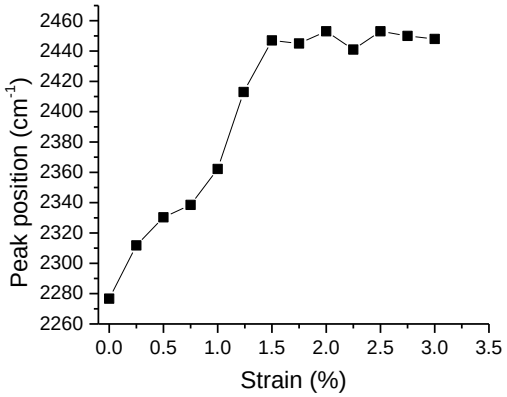

Figure 4-20. Upshift of the new peak at 2276 cm^{-1} upon straining the 1 wt% wrapped SWNT film.

4.3.5 Effect of PMMA wrapping on the Dynamic Mechanical Response of Films and Buckypapers

PMMA relaxation and glass transition was monitored by DMA. To maintain the static stress and prevent the sample from buckling the static stress was maintained at 20% higher than the dynamic stress, which results in creep during each DMA cycle. DMA of the PMMA film exhibited a shoulder around 100 °C and a scattered tan δ peak located

around 125 °C (Figure 4-21a). While the tan δ peak was attributed to the glass transition of PMMA, the shoulder was ascribed to the solvent-PMMA interactions, which could be removed after the first heat treatment [172]. This suggests that some residual DMF remains in the structure even after drying at 70 °C under vacuum for more than 24 hours. After complete removal of the solvent by repeating DMA measurements on the sample or by heating the film up to 110 °C under vacuum, DMA of PMMA film exhibited a more developed tan δ peak centered around 127 °C. Residual DMF was also detected from the IR spectrum of the PMMA film (Figure 4-22a). The band at 1680 cm^{-1} is attributed to the absorption of amide of DMF, and disappears upon heating the film up to 130 °C (Figure 4-22b). The residual solvent is also observed with the incorporation of SWNTs, in both 1 wt% wrapped (b) and non-wrapped (Figure Figure 4-21c) PMMA/SWNT films. For the PMMA film, the magnitude of the shoulder is 50 percent lower than the tan δ peak. Since the magnitude of the shoulder peak is comparable to the that of the SWNT composite tan δ peak, it seems to shift the tan δ rather than appear as a shoulder. After the first DMA heat treatment, significant increase of tan δ peak temperatures were observed from both 1 wt% wrapped and non-wrapped PMMA/SWNT films, owing to the removal of solvent-PMMA interactions (the DMF could also be removed by heating the film up to 120 °C). Marginal increase of tan δ peak temperatures was observed after the 3^{rd} and 4^{th} DMA heat treatments which can be attributed to the alignment of SWNTs arising from slight elongation during subsequent DMA cycles. Figure 4-23 shows the tan δ peaks for the PMMA and 1 wt% composite films after the first heating cycle. The tan δ peaks are at 127° C, 131° C and 134° C for the PMMA film, 1 wt% non-wrapped SWNT and 1 wt% wrapped SWNT films, respectively. Previous study on PMMA and MWNTs showed that

T_g increased with increased MWNT loading since the nanotubes hindered the segmental motions of PMMA chains [173]. While the polymer molecule segments in proximity of CNTs are more constrained and have a higher T_g, the unconstrained polymer segments would exhibit the T_g of bulk polymer matrix, resulting in broadening of the tan δ peaks (30% higher full width half maximum of wrapped SWNT film compared to non-wrapped film) as previous studies indicated [173-175]. Interestingly, tan δ peak of 1 wt% wrapped film in the current study showed a further reduced tan δ magnitude and a broadened tan δ width when compared to that of 1 wt% non-wrapped film. We know from the Raman study that the bundles are smaller in the PMMA wrapped SWNTs, which will result in a larger polymer-SWNT interface compared to the non-wrapped SWNTs which has larger bundles. A larger PMMA-SWNT interface results in more polymer chains that have hindered motion, increasing the fraction of the constrained polymer, leading to shifting of tan δ to higher temperature and suppressing its magnitude. The helical PMMA wrapping around the SWNTs is constrained to further increase in T_g. It is possible that the helical PMMA facilitates the packing of the amorphous chains in the interphase region. The dynamic mechanical data also show confinement of the polymer chains upon addition of the SWNT and restricts polymer chain movement at higher temperatures for both wrapped and non-wrapped films (Figure 4-23b). At 60 °C the 1 wt% non-wrapped SWNT has the lowest storage modulus. At 150 °C the storage modulus of PMMA decreases the most, with storage modulus of 1 wt% wrapped and non-wrapped SWNTs being 12.5 times and 4.2 times that of PMMA, respectively.

The SWNT/PMMA (65 wt%/35 wt%) buckypaper did not show any glass transition (Figure 4-24), since the PMMA chains were in helical form and the chain

segments were immobilized. The small tan δ value suggests near elastic response in this temperature range. The storage modulus steadily decreases as temperature increases. The buckypaper elongates up to 4.5 % percent at 180 °C during DMA. The reduction in storage modulus, and increase in tan δ, could be due to slipping of nanotubes resulting in fewer nanotube-nanotube junctions.

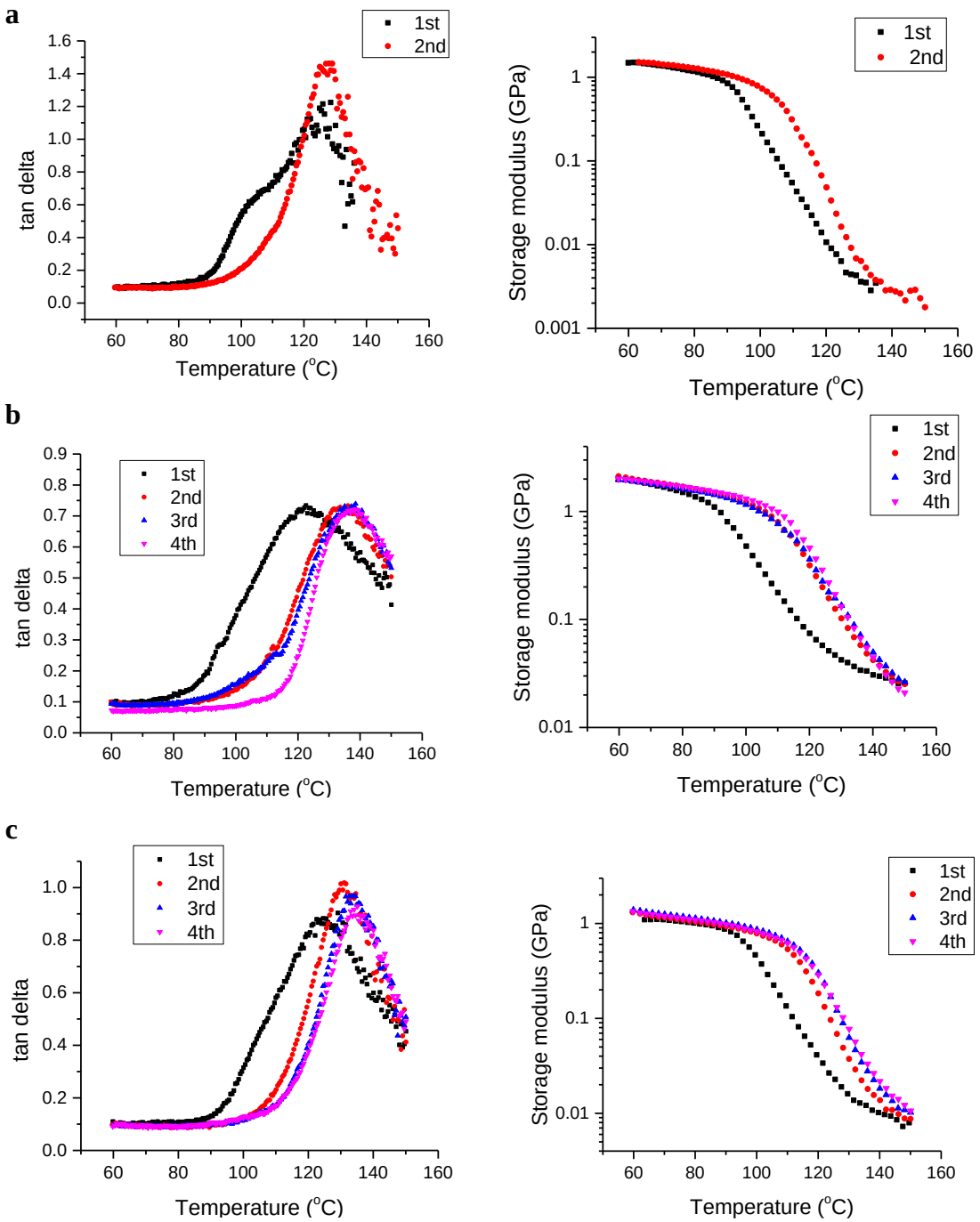

Figure 4-21. DMA of PMMA and PMMA/SWNT composites repeated on the same sample a) PMMA, b) 1 wt% wrapped, c) 1 wt% non-wrapped.

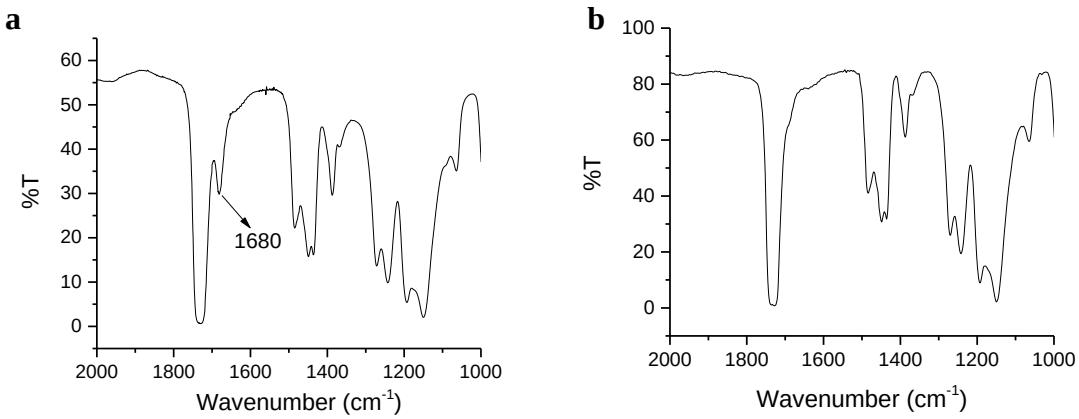

Figure 4-22. FTIR spectrum of dry cast PMMA film (a) before, and (b) after heat treatment. (a) The 1680 cm^{-1} absorption band is attributed to amide C=O bond in DMF. (b) This absorption band disappears upon heating the film at 130 °C for 10 minutes.

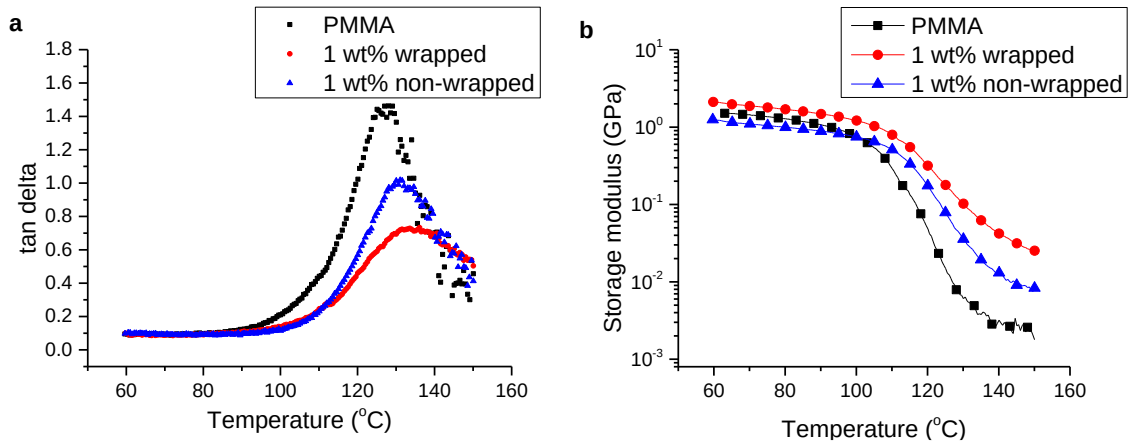

Figure 4-23. DMA of PMMA and PMMA/SWNT composites. The results are for samples with no residual DMF.

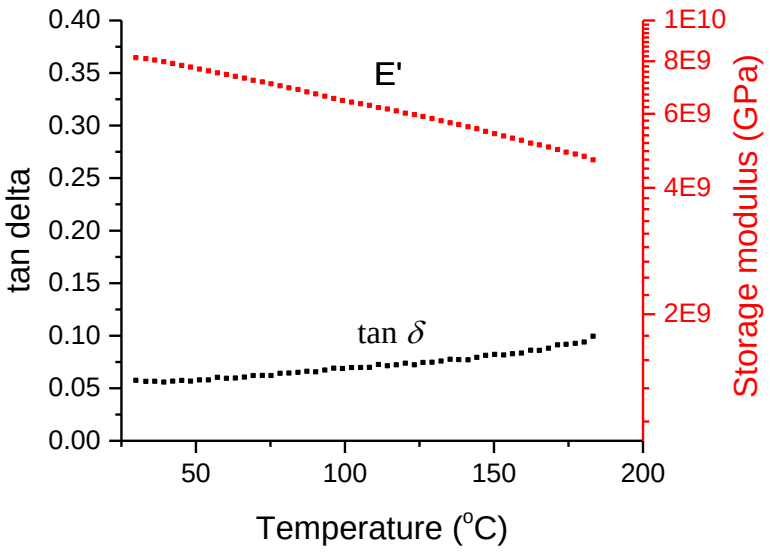

Figure 4-24. DMA of SWNT/PMMA (65 wt%/35 wt%) buckypaper.

4.3.6 Effect of PMMA Wrapping on the Electrical Conductivity of Films and Buckypapers

While PMMA wrapped SWNTs were superior to non-wrapped SWNTs in terms of improving the mechanical properties of buckypapers and composite films, the PMMA wrapping reduced the electrical conductivity of the samples. The conductivity of the pristine buckypaper was an order of magnitude higher than that of SWNT/PMMA (65 wt%/35 wt%) buckypaper (Table 4-5). The PMMA wrapped SWNTs are no longer directly in contact with each other due to the insulating polymer layer separating them at SWNT junctions. Electrons have to pass through two monolayers of polymer coating SWNTs. The conductivity of the wrapped SWNT film was very low at 1 wt% SWNT content. This has been attributed to the good dispersion of the PMMA wrapped SWNTs which prevents electrical percolation of the nanotubes coupled with the PMMA coating

which further prevents SWNT-SWNT contact. However, the 1 wt% non-wrapped SWNT film had conductivity several orders of magnitude higher than that of the wrapped SWNT film. The aggregation of SWNTs leads to a lower percolation threshold as compared to well dispersed SWNTs at 1 wt% (Figure 4-25). The aggregation of the 0.1 wt% non-wrapped SWNT films in Figure 4-1 shows that the nanotubes phase separate until they form islands of connected nanotubes in the film. At 1 wt%, phase separation leads to a non-homogenous structure throughout the whole film as shown in Figure 4-3 (not islands), resulting in a percolated network in the film. At higher CNT content the conductivity of the PMMA wrapped SWNTs and non-wrapped SWNT films become similar. At higher SWNT concentration, as SWNT-SWNT overlaps increases the conductivity of the films increases.

Table 4-5- Electrical conductivity of the SWNT and SWNT/PMMA (65 wt%/35 wt%) buckypapers and composite films with and without PMMA wrapping.

	PMMA wrapped Conductivity (S/m)	Non-wrapped Conductivity (S/m)
SWNT/PMMA buckypaper	1100 ± 100	-
SWNT buckypaper	-	10000 ± 500
1 wt%	$1.785\times10^{-5} \pm 3\times10^{-7}$	0.978 ± 0.06
5 wt%	0.17 ± 0.01	12.7 ± 0.5
10 wt%	26.5 ± 3.5	24.8 ± 2.6

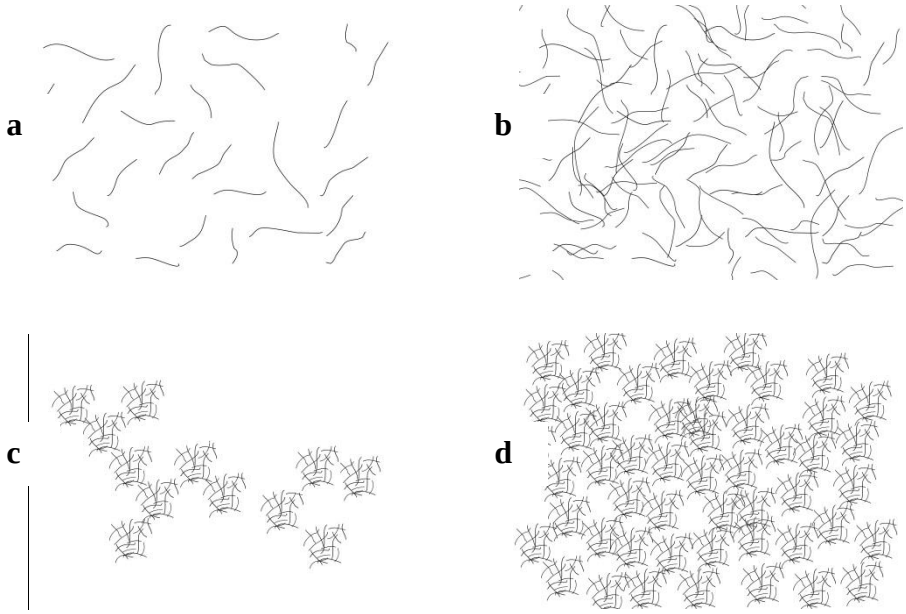

Figure 4-25. Schematic of PMMA wrapped SWNTs films a) 1wt% and b) 10 wt%, and non-wrapped SWNT films c) 1 wt% and d) 10 wt%.

4.4 Conclusions

Wrapping SWNTs with PMMA in buckypaper increases the modulus and tensile strength 5.9 and 3.7 times, respectively, compared to pristine SWNT buckypaper. This increase is attributed to the debundling effect of the helical PMMA around SWNTs. The debundled SWNTs form a network of individual SWNTs that are more effective in transferring stress to the nanotubes in the buckypaper compared to bundled SWNTs in the pristine buckypaper. While SWNTs in the PMMA wrapped buckypaper experience 1 GPa stress, corresponding to 5 cm^{-1} shift of the G' Raman band, the SWNTs in the pristine buckypaper do not exhibit any shift of the G' Raman band. In composite films, stress is transferred from the matrix to SWNTs, hence higher stress transfer can be achieved by maximizing the SWNT-PMMA interface by debundling the SWNTs. SWNTs in the PMMA wrapped SWNT composite experience 3.1 GPa stress, twice as

much stress as the SWNTs in the non-wrapped SWNT film. This results in up to 75% higher modulus in wrapped SWNT films compared to non-wrapped SWNT films. The T_g of the composite with the wrapped SWNTs is 3° C higher compared to non-wrapped SWNT film, suggesting higher fraction of constrained polymer chains due to better dispersion in the PMMA wrapped SWNTs. Helically wrapped PMMA has negligible chain mobility due its strong interaction with SWNTs and does not exhibit a glass transition temperature. Wrapping the SWNTs in the buckypaper with the insulating PMMA reduces the electrical conductivity of the buckypaper by an order of magnitude.

CHAPTER 5

CARBON NANOTUBE REINFORCEMENT OF POLYACRYLONITRILE PRECURSOR AND CARBON FIBERS

5.1 Introduction

Polyacrylonitrile (PAN) is a synthetic semi-crystalline polymer made from polymerization of acrylonitrile. It has a melting temperature of +300 °C, but degrades before melting. PAN films and fibers can be processed from polymer solution to avoid degradation, where PAN is dissolved in solvents such as dimethylformamide (DMF) and dimethylacetamide. Fiber spinning from polymer solutions is carried out with a variety of techniques such as wet spinning, dry spinning and gel spinning. In dry spinning, the solvent is removed from the fiber by stream of air or inert gas. In wet and gel spinning the dissolved polymer is coagulated in a non-solvent bath. Gel spinning enables production of highly oriented fibers with high strength and modulus. PAN is the predominant precursor material for the production of carbon fiber. Commercial high performance PAN based carbon fibers possess great tensile properties (tensile strength 3-7 GPa and tensile modulus 230-590 GPa). PAN fibers with different fillers, such as lignin and carbon nanotubes (CNTs), have been made for renewability, cost and improved properties. Lignin which is a biorenewable byproduct of pulp and paper industry has been incorporated in PAN to reduce cost of fiber precursor, and can also decrease time and energy cost of carbon fiber production [176, 177]. CNTs have been proposed as fillers to improve the mechanical properties of carbon fibers [132]. The improvement of carbon

fiber properties upon addition of CNTs may be attributed to the templating effect of CNTs on the graphitic structure of carbon fibers [133] or on the load bearing capability of CNTs. Nonetheless, well dispersed CNTs are necessary to maximize their effect.

Aggregation of CNTs was addressed in detail in chapter 2. We obtained individual or near individual single wall CNTs (SWNTs) in poly(methyl methacrylate) (PMMA) polymer. The SWNTs were individualized by wrapping them with PMMA. PMMA wrapping prevented SWNT aggregation and exfoliated them in buckypapers and PMMA composite films.

Gel spun PAN fibers are drawn in one or more stages to extend and align the PAN chains in the fibers. Fiber drawing is essential to obtain high modulus and strength precursor fibers. The modulus and tensile strength increases by several factors upon drawing. It has been suggested that CNTs are exfoliated upon fiber drawing [178]. CNT exfoliation was evidence by sharpness of van Hove transition using UV-vis spectroscopy [178]. However, a more accurate method to determine debundling is by comparison of the radial breathing mode (RBM) intensities as discussed in chapter 2 and Ref. [164, 179, 180].

CNTs can be dispersed in solvents and polymers that have good interaction with CNTs. Polymers with stiffer backbones are reported to interact favorably with CNTs [181]. Molecular dynamics simulations have suggested that polymers with stiffer backbones, such as conjugated polymers, have a better interaction with SWNTs compared to flexible chain polymers [182]. Wrapping of rigid chain conjugated polymers around SWNTs has been reported and evidenced by SEM [40]. The favorable interaction

between conjugated polymer and CNTs has been attributed π-π stacking [183]. Using molecular dynamics approach, Yang et al. [184] reported that in comparison to polystyrene, poly(phenyl-acetylene) which has conjugated chain structure in the backbone, exhibits better interaction with SWNT.

Among the class of flexible chain polymers, PAN is unique polymer, containing strongly polar nitrile group. Being a precursor to manufacture high strength carbon fiber, thermal oxidative stabilization of PAN has been extensively studied. Oxidative stabilization involves three steps; dehydrogenation, cyclization and oxidation (Figure 5-1). Dehydrogenation of PAN leads to conjugated nitrile structure. Conley et al. [185] studied oxidative degradation of PAN at temperatures between 100 °C to 200 °C, which is lower than typically used temperatures during oxidation of PAN precursor to manufacture carbon fibers. It has been reported that strong infra-red (IR) absorbance peak corresponding to -C=C- (at wavenumber of 1600 cm^{-1}) appears within first hour of heat treatment at 150 °C in air atmosphere. When the heat treatment is carried at 160 °C in vacuum or nitrogen atmosphere, no significant change is observed in the IR spectrum. When studied at 200 °C, continual increase in the absorbance peak corresponding to -C=C- was reported until 150 minutes (Figure 5-2**)**. During this time, no change in absorbance was observed corresponding to -C≡N. The lack of change in the nitrile peak demonstrates that the process is dehydrogenation and not cyclization. Based on the Arrhenius equation, it was calculated that to attain the same spectral state of degradation on identical PAN samples, heat treatment time required at 100 °C, 150 °C and 200 °C is 550 hours, 11 hours and 2 hours, respectively.

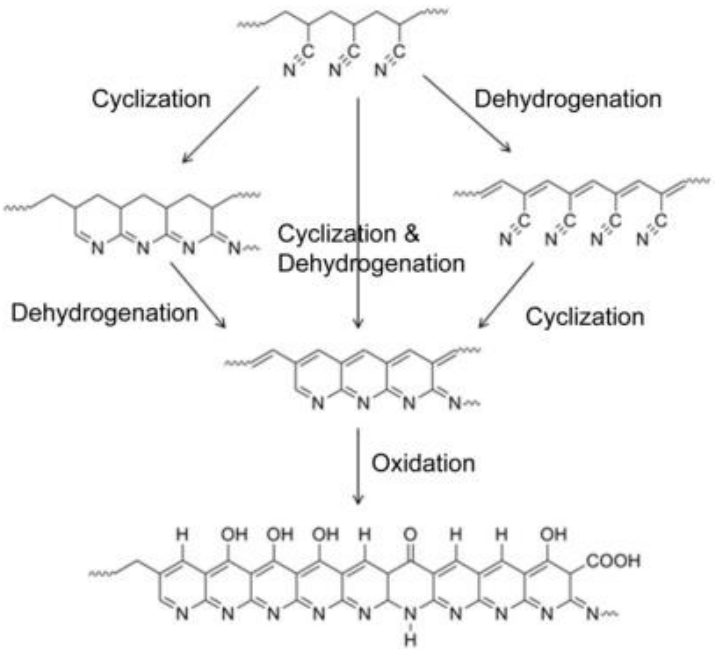

Figure 5-1. Chemical reaction schemes occurring during stabilization of PAN [186].

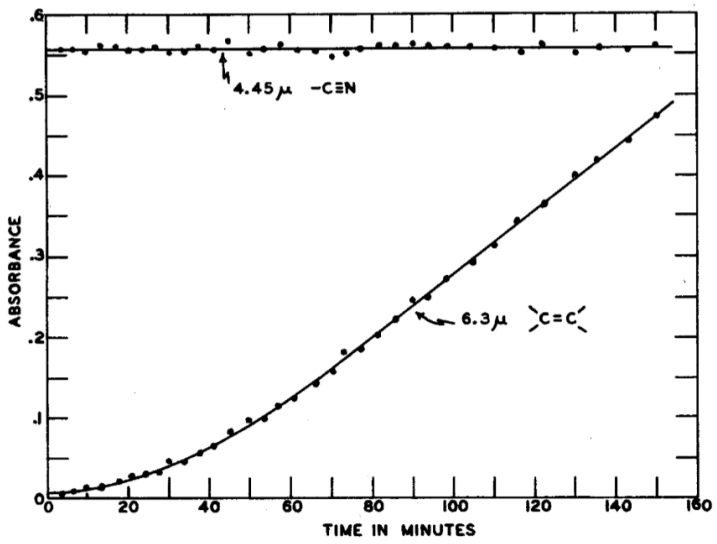

Figure 5-2. IR intensity of nitrile and C=C bonds monitored during PAN oxidation in air at 200 °C [185].

Chae et al. reported that upon incorporation of 1 wt% SWNT in PAN, carbonized PAN/SWNT fibers possessed 49% higher tensile modulus and 64% higher tensile strength as compared to carbonized PAN fibers [187]. Such an enhancement in carbon fiber properties was attributed to the differences between the fracture mechanics between the two fibers. The fracture surface of carbonized PAN/SWNT fibers showed numerous fibrils embedded in the brittle carbon matrix as shown in the scanning electron microscopy (SEM) images (Figure 5-3a), whereas carbonized PAN fibers did not show such fibrils (Figure 5-3b). Fibrils in the case of carbonized PAN/SWNT fibers have been shown to be consisted of CNTs surrounded by highly ordered graphitic regions of carbonized PAN (Figure 5-4a-f). Such a graphitic region was absent and only turbostratic structure was present in the case of carbonized PAN fibers (Figure 5-4g).

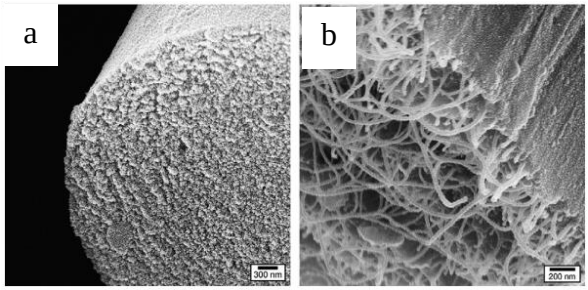

Figure 5-3. SEM micrographs of carbonized a) PAN and b) PAN/SWNT fibers [187].

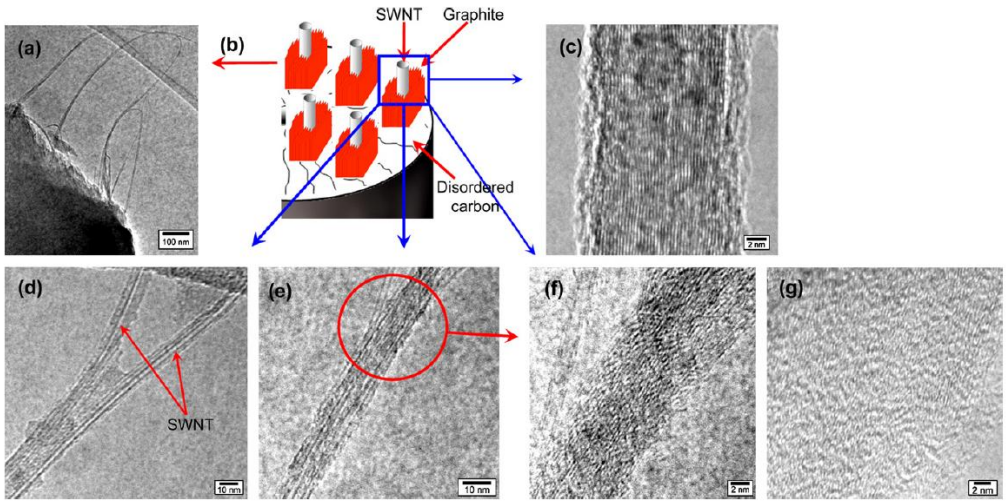

Figure 5-4. (a-f) High resolution transmission electron microscopy (TEM) images and schematic representation of PAN/SWNT carbon fiber. (g) TEM image of carbonized PAN fiber [187].

In this chapter, two hypotheses regarding improving SWNT-PAN interaction are studied. Improved SWNT-PAN interaction may lead to better precursor and carbon fiber properties. The first hypothesis relates to the PMMA wrapping of SWNTs. The second hypothesis relates to the conjugation of PAN structure in the solution.

We have observed that PMMA helically wraps around SWNTs. PMMA wrapping is expected to prevent the aggregation of SWNTs in PAN and improve SWNT dispersion in the fiber. PMMA degradation during stabilization and carbonization may lead to voids in the carbon fiber structure. PMMA completely degrades and burns out in both air and nitrogen. However, PMMA carbonization and graphitization has been reported by electron beam stabilization [188, 189]. Some fillers such as polysulfide polymers [190] and ZnO [191] have been shown to stabilize PMMA. Incorporation of hydroxyapatite nanorods in PMMA have been shown to induce PMMA carbonization [192].

The main mechanism of PMMA degradation is main chain scission of the C-C bonds. Two main processes of decomposition of PMMA are terminal C=C bond scission and random main chain C-C scission [193, 194]. The first stage of PMMA degradation is initiated by terminal C=C bonds, starting at ~220° C. The second stage is initiated by C-C scission at ~300° C. The intermediate products decompose and generate MMA monomer. There is a possibility that the PAN matrix surrounding the helical PMMA can stabilize the MMA monomers. If the PMMA degrades during stabilization, we would expect minimal stress transfer to SWNTs, due to structure discontinuity around SWNTs in the stabilized fiber. Electron microscopy may also reveal the graphitic structure surrounding the SWNTs and the effect of PMMA wrapping on the graphitic structure. The effect of PMMA wrapping on SWNTs in polyacrylonitrile (PAN) fibers is investigated. This will be done by incorporating PMMA wrapped and non-wrapped SWNTs in the PAN solution and processing fibers from these solutions. Structure and properties of the precursor and carbon fibers are studied.

Several researchers have reported that polymer/CNT interaction is stronger in conjugated polymers than in non-conjugated polymers. If conjugated PAN can be formed during solution preparation for processing PAN/CNT based precursor fiber, stronger interaction between CNT and conjugated PAN may be possible. Such an enhanced PAN/CNT interaction would then lead to templating of PAN in the presence of CNT causing enhancement of ordered chain confirmation of PAN surrounding CNTs. Upon stabilization and carbonization, enhanced order of PAN molecules in PAN/CNT precursor fibers would then result in highly ordered graphitic region in the vicinity of CNTs that will ultimately play a crucial role in enhancing the tensile strength and tensile

modulus of resulting carbon fibers. It has been reported that oxidative atmosphere is necessary to form C=C double bonds in PAN structure at lower temperatures [185]. To understand the effect of oxidative atmosphere during solution preparation, PAN/SWNT solutions under air and nitrogen atmosphere are prepared, and changes in the chemical structure is analyzed from IR spectroscopy. The SWNT dispersion quality is investigated using Raman spectroscopy. The effect of air processing on precursor and carbon fiber is also studied.

To understand the role of PMMA wrapping and air processing, PAN/SWNT fibers with and without PMMA wrapping and PAN/SWNT fibers processed under air and nitrogen are made and their mechanical properties are compared.

5.2 Experimental

5.2.1 Materials

HiPco^{TM} SWNTs (grade SP0300, average diameter 0.9 nm, purity 98%, Carbon Nanotechnologies Inc.) were used in this study. Dimethylformamide (DMF, ACS grade, 99.8% purity) and PMMA (MW= 350,000 g/mol) polymer were obtained from Sigma Aldrich. Polyacrylonitrile-co-methacrylic acid copolymer, (PAN-co-MAA) (96/4 by weight) with a viscosity average molecular weight of 247,000 g/mol was purchased from Exlan, Co. (Japan).

5.2.2 Solution Preparation and Fiber Processing

15 g of PAN-co-MAA was added to 100 mL DMF at room temperature while stirring inside a 1 L reactor. The reactor was transferred to an ice bath and stirring was

started immediately at 300 RPM under nitrogen purge (30 SCFH). After three hours the chilled water bath was replaced with silicone oil bath and the bath temperature was increased gradually from 25 to 80 °C. This initial preparation stage was the same for all trials. The PAN solution was stirred at 90 °C for 4 hours and control fiber was spun (T1).

Master batch SWNT suspensions were prepared by adding 150 mg SWNTs to 300 mL DMF, and homogenized for 10 minutes. 30 mL of this suspension (containing 15 mg SWNT) was added to 300 mL DMF and sonicated for 24 hours. The first sonicated SWNT dispersion was transferred to the reactor containing the dissolved PAN and vacuum distillation was started. Ten bottles containing DMF/SWNT were added to the reactor and distillation was carried out during day time over the period of 1 week. The solution was kept under stirring condition (300 RPM) overnight with bath temperature of 75-80 °C under nitrogen flow of 30 SCFH (T2).

The PMMA wrapped SWNT solution was prepared by adding 15 mg PMMA along with 15 mg SWNTs in DMF and sonicating for 24 hours. Ten bottles containing DMF/SWNT/PMMA were added to the reactor and distillation was carried out during day time over the period of 1 week. The solution was kept under stirring condition (300 RPM) overnight with bath temperature of 75-80 °C under nitrogen flow of 30 SCFH (T3).

To study the effect of air atmosphere the purge gas was switched to air during the night. PAN/SWNT (T4) and PAN/SWNT/PMMA (T5) fibers were prepared from solution which were kept under stirring condition (300 RPM) overnight with bath temperature of 85-90 °C under air flow of 30 SCFH.

For spinning, the solutions were transferred to the barrel of a spinning system designed by Hills, Inc. and a spinnerette with a 200 µm diameter hole was used for fiber spinning. The barrel temperature was kept at ~56 °C and the spinneret temperature at ~75 °C. All fibers were spun into methanol coagulation bath at about -40 °C with an air gap of ~ 3 cm. As-spun fibers were stored in a methanol bath at −30 °C for over 20 hours and subsequently drawn at room temperature followed by drawing in a glycerol bath at ~160 °C. The solutions and fiber spinning trials are summarized in Table 5-1.

Table 5-1. Summary of solutions that were prepared and characterized.

Trial	Composition	SWNT/PMMA (wt% / wt%)	Solid cont. (wt%)	SDR	CDR	HDR	Draw ratio
T1	PAN-N	0 / 0	14	3	1.5	6	27
T2	PAN/SWNT-N†	1 / 0	13.8	3	1.5	6	27
T3	PAN/SWNT/PMM-N	1 / 1	16.7‡	3	1.5	5.4	24.5
T4*	PAN/SWNT-A†	1 / 0	-	-	-	-	-
T5	PAN/SWNT/PMMA-A	1 / 1	14.5	3	1.5	5.9	26.5

SDR: spin draw ratio, CDR: cold draw ratio, HDR: hot draw ratio
* T4 Fiber was not spun due to failure of stirring mechanism during solution preparation, but the solution was characterized using Raman and FTIR spectroscopy.
† Atmospheric gas; A: Air, N: Nitrogen
‡ Solid content inadvertently higher than target.

Stabilization and carbonization was done in an MHI tube furnace. A dual mount setup was used to process two set up fibers simultaneously. A temperature ramp rate of 5 °C/min was used for all steps. Carbonization scheme was carried out at 1300 °C and held at that temperature for 5 minutes and allowed to cool down under nitrogen purge.

5.2.3 Characterization

Single filament PAN precursor and carbon fiber tensile testing was performed on a FAVIMAT+ (Measured Solutions, Inc.). A gauge length of 25.4 mm was used for testing. The strain rates for tensile testing for precursors and carbon fibers were 1%/s and 0.1%/s, respectively. The linear density of each filament tested was measured by inline vibroscope. Raman spectra were obtained using a 785 nm laser on a HORIBA XploRA Raman Microscope System. Raman spectra were collected during fiber deformation at a gauge length of 25 mm by straining individual fiber filaments strips using a stretching rig. The Raman spectra were collected using parallel (VV) polarizers with the straining direction parallel to the polarizer and analyzer directions. Infrared spectra (IR) were collected with a Perkin Elmer Spectrum One infrared microscope. Wide-angle X-ray diffraction (WAXD) data were obtained in transmission mode on a Rigaku Micromax-002 (λ=0.15418 nm) system. Scanning electron microscopy (SEM) was performed on a Hitachi SU8010 at an accelerating voltage of 5 kV.

5.3 Results and Discussion

5.3.1 Effect of Atmosphere During Solution Preparation on the Chemical Structure of PAN

To study the chemical structure of PAN, the PAN/SWNT solution (T4) processed under air atmosphere was sampled at different times during solution preparation. The samples were collected at 0, 6 and 72 hours after the reactor was purged with air. The samples were used to cast a thin film, which was dried in vacuum at 65 °C for 1 day. These films were used to collect IR spectra. The strong peak at ~1675 cm^{-1} belongs to

amide group of DMF. The intensity of 1675 cm^{-1} varies slightly from one sample to another and is due to residual DMF which was also observed in PMMA films. The peaks at ~1730 cm^{-1} and 2240 are attributed to the methacrylic acid and the nitrile group, respectively. Conjugation is mainly identified by monitoring an increase in intensity of C=C and C=N absorption bands and suppression of the nitrile, C≡N, absorption band. The C=C peak is at ~1600 cm^{-1} and the C=N peak is around 1660 cm^{-1}. The IR spectra of the PAN/SWNT film did not show any evolution with increased processing time that would suggest dehydrogenation or conjugation (Figure 5-5). Since a previous study showed that at 100 °C PAN stabilizes after 550 hours [185], higher processing temperature/time is necessary to achieve dehydrogenation. The effect of stabilization on the IR spectra has been demonstrated in PAN and PAN/CNT fibers stabilized for various times (Figure 5-6) [195], in which during stabilization, absorbance increases over a broad range, from 1100 to 1750 cm^{-1}.

Comparison of the solutions processed under air and nitrogen atmosphere is shown in Figure 5-7, and demonstrates no change in the chemical structure of PAN indicating dehydrogenation or formation of C=C bonds. There are some subtle differences in peak intensities between the nitrogen and air treated PAN/SWNT films, such as the peak at 1390 cm^{-1}, which is attributed to CH_3 bending.

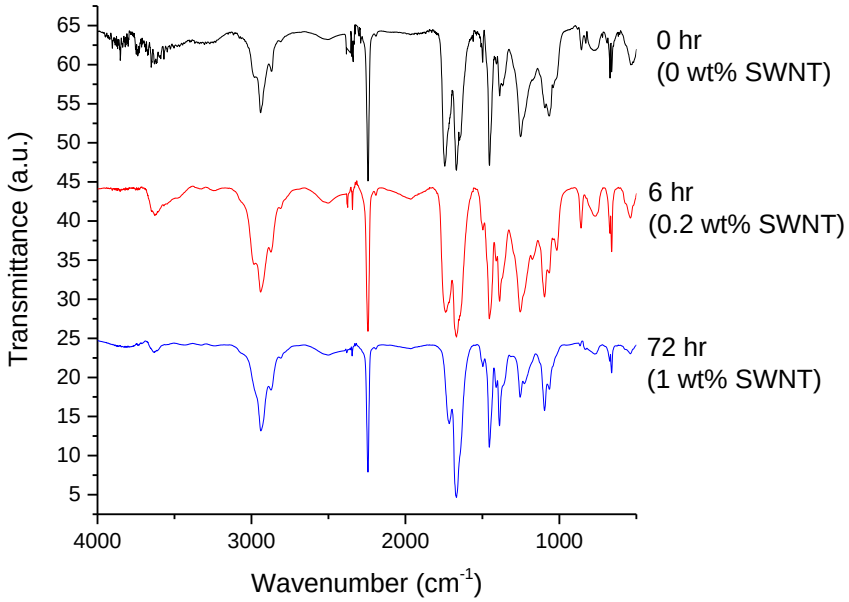

Figure 5-5. IR of PAN and PAN/SWNT solution stirred under air purge for increasing durations at 90 °C. The first sample was collected before adding SWNTs to the PAN solution. Stabilization is not supported by FTIR spectroscopy. The spectra were collected from thin film samples. The spectra have been shifted vertically for clarity.

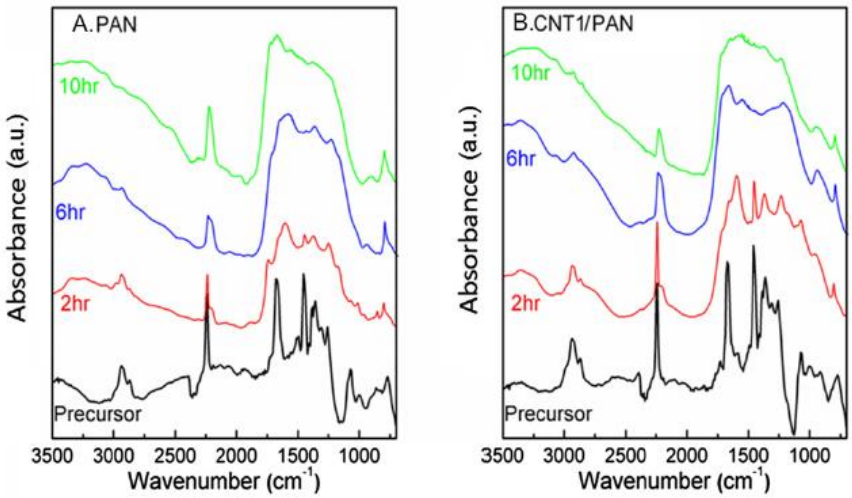

Figure 5-6. FTIR spectra of precursor and stabilized PAN and PAN/CNT fibers. Fibers were stabilized at 267° C for 2, 6 or 10 hours [195].

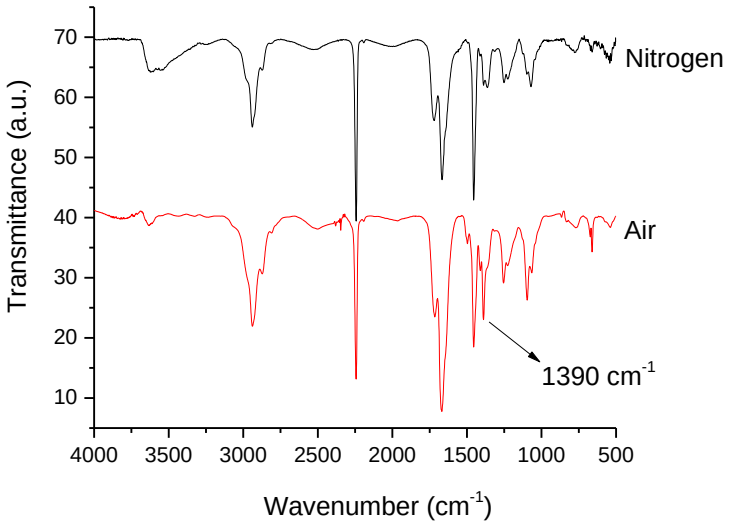

Figure 5-7. IR spectra of PAN/SWNT films processed under nitrogen and air after 72 hours. Air spectrum shifted vertically for clarity.

The effect of air processing on the mechanical degradation and chain length of PAN is unknown in this study. Mechanical degradation and reduction in molecular weight of various polymers solution under shear stress has been reported [196, 197]. One study found polymer degradation is faster under oxygen compared to argon [198], reporting that even one percent oxygen content is enough to accelerate rate of degradation. During mechanical degradation, radicals are formed when the bonds are ruptured. These radicals can recombine and causing the polymer chain to heal and prevent mechanical degradation. When oxygen is present, oxygen can react with the radicals and terminate the broken chain segments while under nitrogen the chains can recombine and prevent reduction of the molecular weight of the polymer.

5.3.2 Carbon Nanotube Dispersion in Polymer Matrix

The SWNT state of aggregation can be determined by investigating the RBM peak intensities in Raman spectra. Upon debundling the intensity of some RBM peaks decrease while the intensity of other peaks increase. The change in intensity depends on the excitation energy of the chiralities and where it lies relative to the laser wavelength. The excitation energy of SWNTs red shift upon bundling, so if the excitation energy of the SWNT approaches the Raman laser energy, upon bundling the nanotube goes off resonance and the intensity of that specific RBM chirality decreases. If the excitation energy is slightly higher than the laser energy, upon bundling the excitation energy approaches the laser energy and the RBM intensity of that chirality increases (Figure 5-8). For this purpose, two chiralities are chosen to study SWNT exfoliation, (11,3) and (10,2) labelled as RBM1 and RBM2 (Figure 5-8a), respectively. One important feature is the ratio of RBM1 intensity compared to RBM2 intensity. When SWNTs are individualized, the intensity of RBM2 is much lower than that of RBM1, RBM1:RBM2 > 1. In a bundled state, the intensity of RBM2 surpasses the intensity of RBM1, hence RBM1:RBM2 < 1 [179, 180].

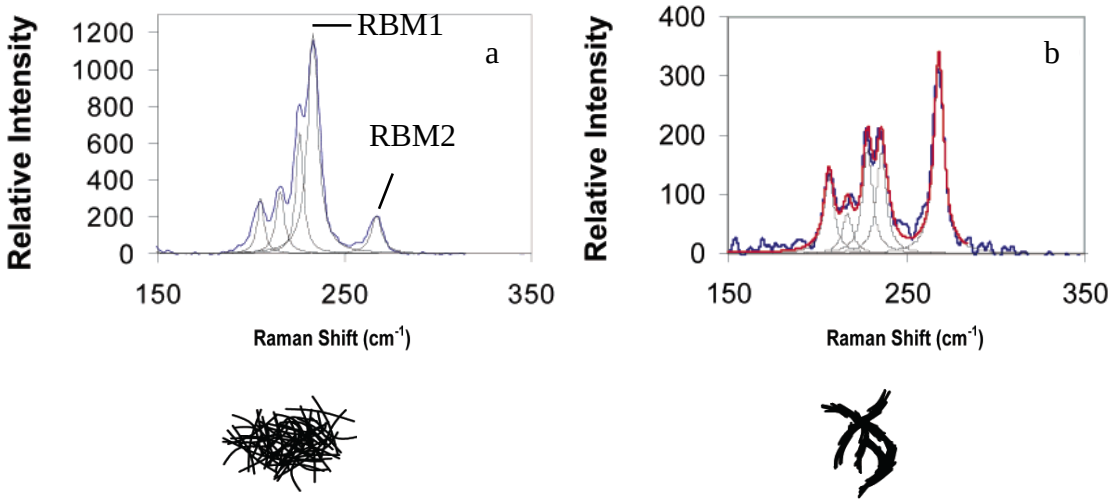

Figure 5-8. Raman spectra and schematic representation of a) individualized, and b) bundled SNWTs. The effect of dispersion on the RBM intensities of the Raman spectra using a 785 nm laser. Two peaks are chosen to show the effect of bundling on the RBM intensities, peaks RBM1 and RBM2. As the nanotubes start bundling, RBM2 intensity increases, exceeding RBM1 intensity. The RBM1 intensity decreases upon bundling [140].

5.3.2.1 Effect of Atmosphere During Solution Preparation on SWNT Dispersion

The Raman spectra of nitrogen and air processed PAN/SWNT solution is shown in Figure 5-9. The ratio of RBM1:RBM2 intensity is 0.41 for air processed solution and 0.7 for nitrogen processed solution. While the RBM1:RBM2 intensity is higher in the nitrogen processed, the SWNTs are aggregated in both systems since RBM1:RBM2<1.

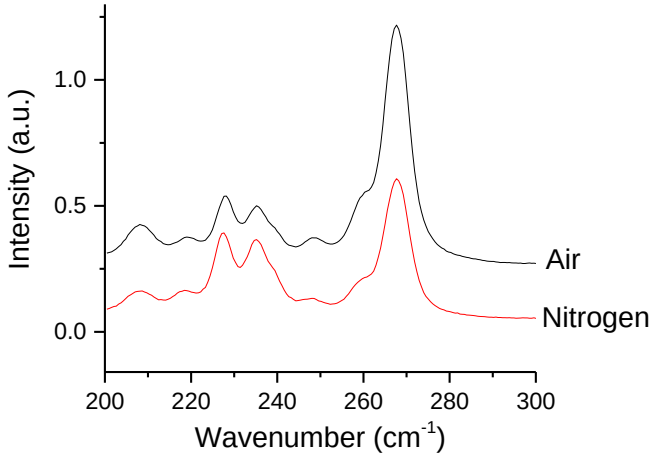

Figure 5-9. Raman spectra of air (T4) and nitrogen (T2) processed PAN/SWNT solutions. The RBM intensities move to a more aggregated state in the air processed solution. Intensities are normalized to G band and shifted vertically for clarity.

5.3.2.2 Effect of PMMA Wrapping on the Exfoliation and Debundling of SWNTs

The RBM intensities in Figure 5-10 demonstrate the effect of PMMA wrapping on SWNT bundling. The RBM1:RBM2 intensity ratio is 0.5 and 2.5 for the non-wrapped and PMMA wrapped SWNT fibers respectively. This clearly demonstrates that PMMA wrapping individualizes SWNTs, while the non-wrapped SWNTs are bundled.

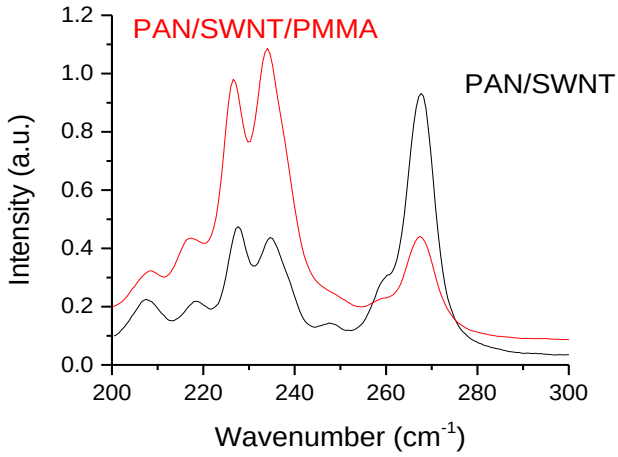

Figure 5-10. Raman spectra of PAN/SWNT (T2) and PAN/SWNT/PMMA (T3) fibers before hot drawing, normalized to G band intensity.

5.3.2.3 Effect of Fiber Drawing on the Exfoliation and Debundling of SWNTs

Raman spectra of the fibers were collected before and after hot drawing. After hot drawing the PAN/SWNT fibers, all RBM intensities decrease (Figure 5-11). This could be attributed to the different environment around SWNTs upon drawing PAN chains, resulting in suppression of all RBM intensities. The ratio of RBM1:RBM2 intensities is 0.5 and 0.70 before and after hot drawing, respectively. The increase in RBM intensity ratio is not enough to support complete exfoliation of SWNTs. It is possible that drawing exfoliates bundles, but the stress is not enough to separate the bundles into individual nanotubes.

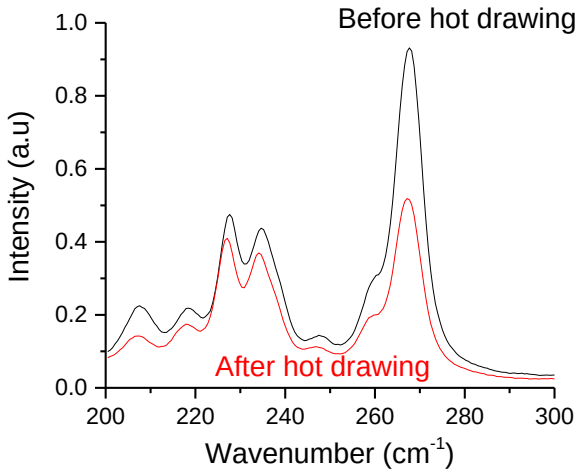

Figure 5-11. Raman spectra of T2 (PAN/SWNT) fibers before and after hot drawing normalized to the G band.

Suppression of the RBM intensities after hot drawing is also observed in the PAN/SWNT/PMMA fibers as shown in Figure 5-12. The RBM1:RBM2 peak intensity ratio decreased from 2.5 before hot drawing to 1.9 after hot drawing. The PMMA wrapped SWNTs experience the opposite trend of non-wrapped SWNT fibers. This indicates an increase in SWNT-SWNT interaction upon hot drawing of PAN/SWNT/PMMA fibers. The RBM1 intensity is still higher than RBM2 peak, RBM1:RBM2 >1, indicating that the nanotubes are individualized.

The Raman spectra of individualized and isolated SWNTs display negligible intensity of the RBM2 peak, 267 cm^{-1} (Figure 5-13). At 1 wt %, if the PMMA wrapped SWNTs are completely individualized, negligible RBM2 intensity is expected, similar to what is observed in Figure 5-13. But that is not the case for the PMMA wrapped SWNTs. The RBM2 intensity in the 1 wt% PMMA wrapped SWNT fibers can be justified with either of the following explanations:

1. If all SWNTs are not debundled and wrapped with PMMA during sonication, they can contribute to the increase in RBM2 intensity.
2. If PMMA chains wrap two or more SWNTs together, they will link them together resulting in some SWNT-SWNT interaction from neighboring connected SWNTs. This also justifies the increase in RBM2 intensity upon hot drawing of the SWNTs (Figure 5-14). Upon hot drawing, the SWNTs become oriented along the fiber direction and PMMA linked SWNTs approach each other, resulting in higher SWNT-SWNT interaction.

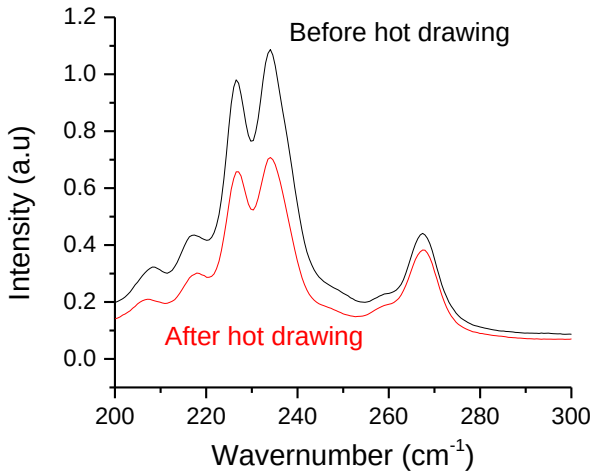

Figure 5-12. Raman spectra of T3 (PAN/SWNT/PMMA) fibers before and after hot drawing, normalized to G band intensity.

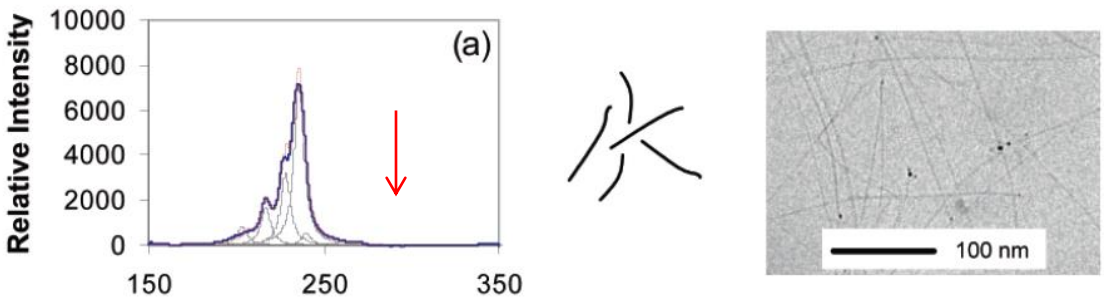

Figure 5-13. Raman spectrum of individual and isolated SWNTs taken at 785 nm along with their SEM micrographs. Note the negligible RBM intensity at ~267 cm^{-1} (RBM2) denoted with the red arrow [197].

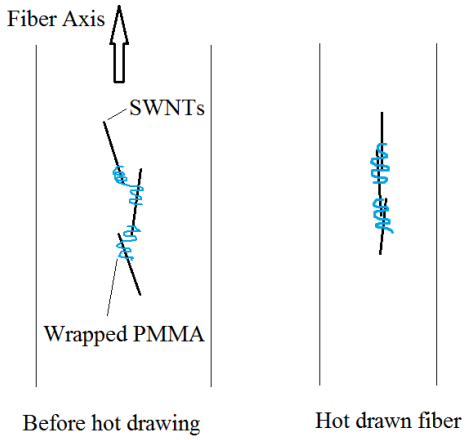

Figure 5-14. The PMMA wrapping may link the SWNTs together resulting in increased SWNT-SWNT interaction upon drawing.

5.3.3 Rheological Behavior of PAN/SWNT Solutions

The solid content and rheological properties of the spinning dope was characterized. The solid content of T1, T2, T3, and T5 solutions were 14 wt%, 13.8 wt%, 16.7 wt%, and 14.5 wt%, respectively, as determined by thermogravimetric analysis (TGA). TGA was carried out by heating the sample up to 160 °C and holding at that temperature for 20 minutes. The variation in solid content was due to experimental

aspects of solution preparation. At low shear rate the neat PAN solution behaves as Newtonian fluid up to ~1 rad/s, and exhibits shear thinning at higher frequencies (Figure 5-15). The PAN/SWNT solutions, either with or without PMMA wrapping, both exhibit shear thinning at low as well as high frequencies, likely due to alignment of carbon nanotubes or breakage of the carbon nanotube network [199]. Quality of dispersion and aspect ratio have considerable effect on the viscosity of CNT containing solutions, with the former being more important [199]. T5 has a lower viscosity compared to T2, despite its better dispersion and higher solid content. Better nanoparticle dispersion is expected to lead to higher viscosity. The lower viscosity supports the hypothesis that mechanical degradation and shortening of PAN chains could be accelerated in an oxygen containing atmosphere compared to nitrogen atmosphere [198]. T3 had a very high viscosity due to higher solid content.

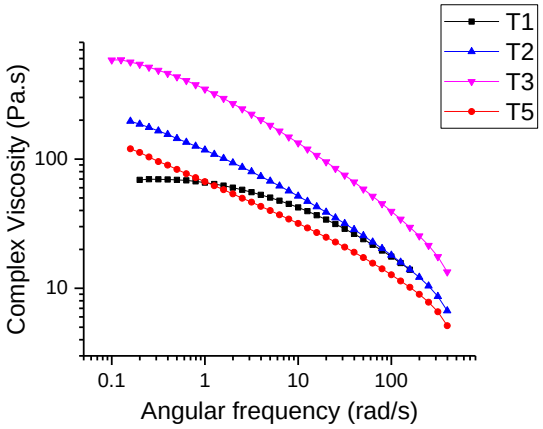

Figure 5-15. Complex viscosity of T5 (PAN/SWNT/PMMA), T2 (PAN/SWNT), T1 (PAN) and T3 (PAN/SWNT/PMMA) solutions as a function of angular frequency.

The loss tangent (tan δ) of polymer and polymer/CNT solutions typically decrease at higher frequencies, indicating an elastic behavior at higher frequencies. However, T5 and T3 solutions (PAN/SWNT/PMMA) exhibits a peak at 2.5 and 100 rad/s (Figure 5-16), respectively. The change in viscoelastic properties of the solution is likely due to polymer wrapping of SWNTs. The shear storage and loss modulus of T5 was lower than T2, despite slightly higher solid content. The storage and loss modulus plots in Figure 5-17 shows that the tan δ peak is mainly from an increase in slope of the storage modulus, rather than a change in the loss modulus trend. This may suggest some sort of phase or domain change at that frequency. Alignment of SWNTs during rheology is possible if the SWNTs are well dispersed. On the other hand, the shear may not be sufficient to align aggregated SWNTs in the PAN/SWNT suspension. If it is assumed that the PMMA wrapped SWNTs create percolated network due to improved dispersion, higher shear storage modulus and viscosity is expected, while this is not the case. Formation of a network and hydrodynamic interactions between the carbon nanotubes has been typically reported at much larger CNT volume content, at least an order magnitude higher [200, 201]. At higher frequencies, 2.5 rad/s, the slope of the shear storage modulus increases, possibly due to the elastic response of PAN at higher frequencies dominating the response of the solution.

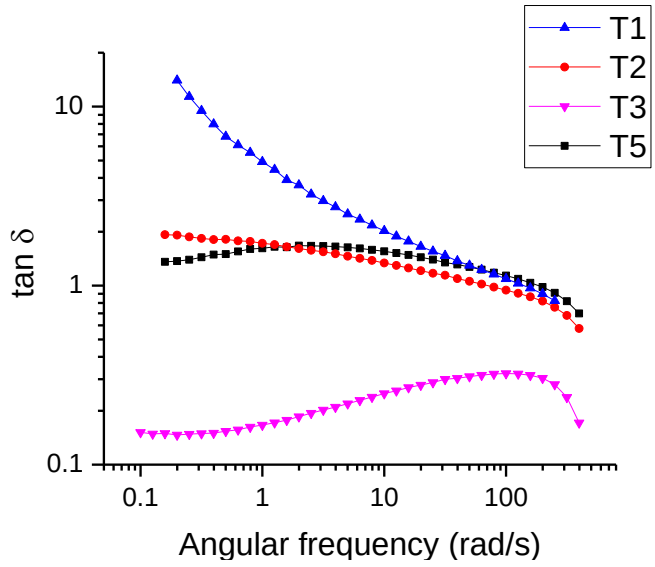

Figure 5-16. Shear loss factor of T5 (PAN/SWNT/PMMA) and T2 (PAN/SWNT), T1 (PAN) and T3(PAN/SWNT/PMMA) as a function of angular frequency.

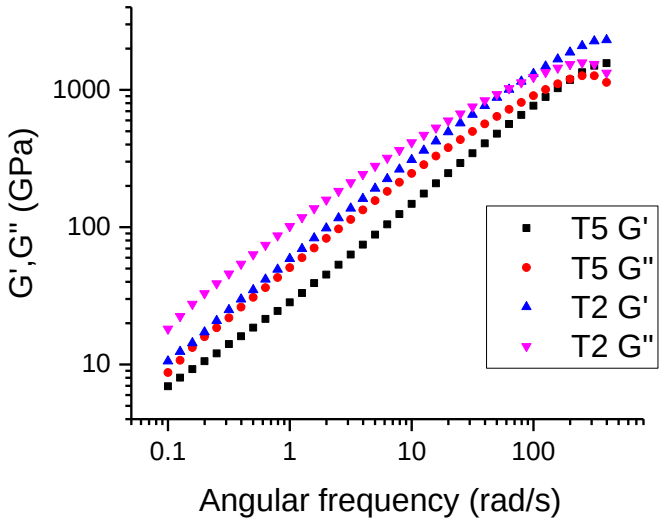

Figure 5-17. Shear storage and loss modulus of T5 (PAN/SWNT/PMMA) and T2 (PAN/SWNT) as a function of angular frequency.

5.3.4 Stress Transfer to Carbon Nanotubes

The G' Raman band shift can be used to determine the strain in the carbon nanotubes. This has been enabled by previous studies that measured the Raman band shift of individual single carbon nanotubes under strain [127]. The G' Raman band shift of three samples were measured for precursor fibers with SWNTs (Figure 5-20 to Figure 5-19). The average G' Raman band shift indicates a maximum band shift, S_m, of -9 ± 0.7, -12.5 ± 0.9, and -11.9 ±0.3 cm^{-1} for T2, T3 and T5, respectively. The PMMA wrapped SWNTs have higher G' Raman band shift compared to the non-wrapped SWNTs. The higher Raman band shift indicates more strain in the carbon nanotubes. This means that the SWNTs in T3 experience 39% higher strain/stress, than the SWNTs in T2.

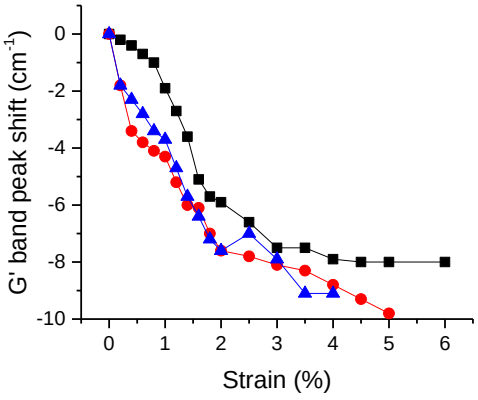

Figure 5-18. G' Raman band shift of T2 (PAN/SWNT) fiber during fiber straining.

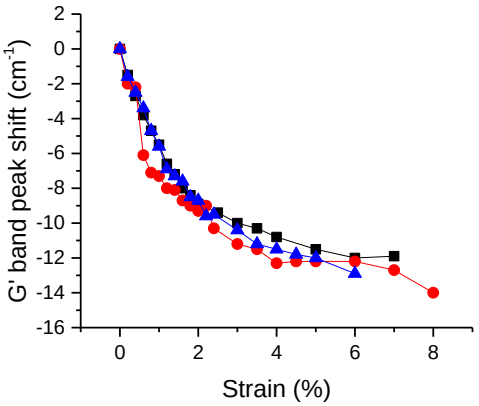

Figure 5-19. G' Raman band shift of T3 (PAN/SWNT/PMMA) fiber during fiber straining.

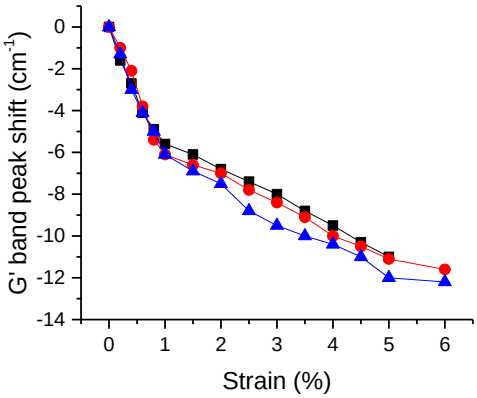

Figure 5-20. G' Raman band shift of T5 (PAN/SWNT/PMMA) fiber during fiber straining.

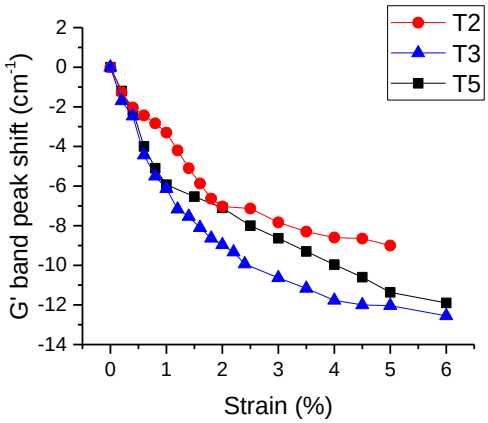

Figure 5-21. Average G' Raman band shift of SWNT containing precursor fibers.

5.3.5 Interfacial Shear Strength

The G' Raman band shift can be used to determine the strain in the carbon nanotubes. The strain can be used to calculate the interfacial shear strength of SWNT-PMMA interface. The interfacial shear strength, τ_i, can be calculated using the modified shear lag equation [86] in a uniaxially aligned carbon nanotube reinforced composite:

$$\tau_i = \frac{nE_{CNT}\varepsilon_i}{2}\tanh(ns) \quad (1)$$

where $n^2 = \frac{2G}{\ln(R/r)E_{CNT}}$, E_{CNT} is the SWNT modulus, E_{CNT} =760 GPa, ε_i is the elongation at PAN-SWNT interface or the SWNT strain. G is the PAN shear modulus and it is estimated to be ~1.5 GPa [202]. *s* is defined as *L/r*, where L is the CNT length and *r* is the CNT radius, and the ratio *R/r* is the geometrical spacing of CNTs, where *R* is the distance between closest CNTs. The geometrical spacing, *R/r*=20.9, was calculated by assuming a square lattice for the CNTs. $\tanh(ns)$ is approximated as ~1, since as *ns*

approaches a value of 3, $\tanh(ns)$ approaches unity. The diameter of the single wall carbon nanotubes used in this work ~0.93 nm and the length is ~500 nm. In this case $n \approx 0.03$ and due to the high aspect ratio of SWNTs, *L/r*>1000. To measure the microscopic strain in the SWNTs, ε_i, we used the G' Raman band shift rate of -37.3 cm^{-1}/% strain of individual SWNTs [127]. The maximum G' Raman band shift, S_m, of each fiber is used to calculate the average strain of SWNTs in that fiber using $\varepsilon_i = \frac{S_m}{-37.3} \frac{\%}{cm^{-1}}$. Using this equation, ε_i is calculated as 0.24 %, 0.34 % and 0.32 %, strain for T2, T3 and T5, respectively. The interfacial shear strength is calculated as 32.9 ± 2.7 MPa, 47.5 ± 3.2 MPa and 43.3 ± 1.1 MPa for T2, T3 and T5, respectively. While the calculated interfacial shear strength for T3 and T5 are higher than T2, the interfacial shear strength difference of T3 and T5 are not statistically different based on current measurements (t-test, P=0.05).

5.3.6 Stress Transfer in Stabilized Fibers

Stress transfer to the SWNTs was studied on T5 before and after stabilization. After stabilization the Raman spectra of the fiber was changed to the extent that the G' band was swamped by the stabilized PAN structure (Figure 5-22) but the G band of SWNTs were visible. For this reason, the shift of the G band was used (Figure 5-23). The G band shift of the stabilized fiber was more than G band shift of the drawn fiber. Therefore, we can conclude that the wrapped PMMA has not degraded at this temperature. In case of PMMA degradation, we would have expected decay in stress transfer to the nanotubes, resulting in smaller G band shift.

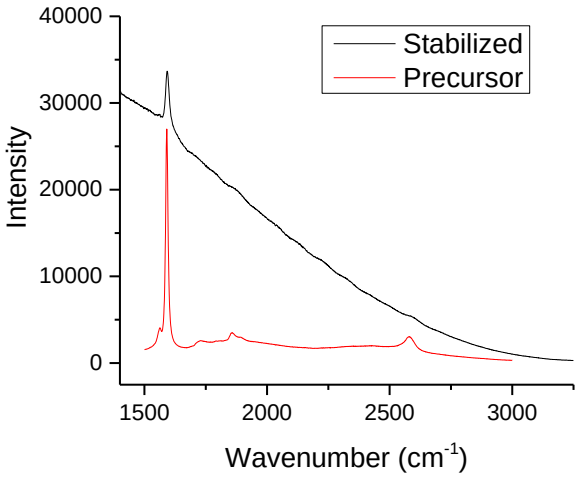

Figure 5-22. Raman spectra of T5 before and after stabilization.

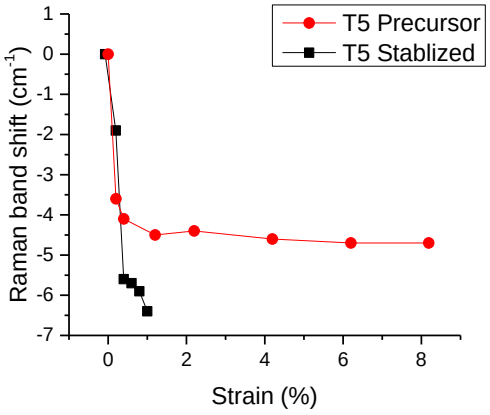

Figure 5-23. Raman G Band shift of T5 before and after stabilization.

5.3.7 Mechanical Properties

5.3.7.1 Precursor Fiber

The tensile properties of the precursor fibers are shown in Table 5-2. T3 has the lowest mechanical properties. The diameter of T5 is smaller than T3 due to higher solid content of the fiber T3. Higher solid content leads to more entanglements of polymer

chains in the solvent. Increased entanglements prevent the chains from being drawn and aligned as effectively as compared to less entangled polymer chains. To compare the tensile properties of T1, T2 and T5, *t*-test with a confidence threshold of 0.05 is implemented. Using this statistical analysis, the modulus and strength of T5 is higher than T2 and T1. The difference between the tensile properties of T2 and T1 is not statistically significant.

Table 5-2. Tensile properties of precursor fibers.

	Diameter (μm)	Modulus (GPa)	Strength (MPa)	Elongation (%)	Comments
T1	12.1 ± 0.6	19.3 ± 0.8	867 ± 44	7.1 ± 0.3	PAN - Nitrogen
T2	12.4 ± 0.6	19.4 ± 0.5	858 ± 47	7.2 ± 0.4	PAN/SWNT - Nitrogen
T3	14.7 ± 1.1	14.9 ± 0.9	710 ± 41	8.0 ± 0.6	PAN/SWNT/PMMA - nitrogen
T5	12.3 ± 0.8	21.9 ± 0.9	931 ± 51	9.1 ± 0.7	PAN/SWNT/PMMA - air

While the total draw ratio of T3, 24.5, and is comparable to the draw ratio of other trials, ~27, the modulus and tensile strength are 20-25% lower than other fibers. Despite the small difference in draw ratio, PAN chain alignment is less in T3, compared to other trials, which could explain the lower mechanical properties of T3. To calculate PAN chain orientation, X-ray diffraction of the fiber was collected. For the X-ray diffraction pattern, a fiber bundle was aligned perpendicular to the X-ray beam and the diffraction pattern was obtained. The orientation is calculated using Herman's orientation factor. Herman's orientation factor can be calculated from the Azimuthal scan (Figure 5-24) of (100) and (210) diffraction peaks (at $2\theta=16.9°$) using the following equations:

$$\langle \cos^2 \chi \rangle = \frac{\int_{-\pi/2}^{\pi/2} I(\chi) \cos^2(\chi) \sin \chi \, d\chi}{\int_{-\pi/2}^{\pi/2} I(\chi) \sin \chi \, d\chi}$$

$$f = \frac{3\langle \cos^2 \chi \rangle - 1}{2}$$

where χ is off angle axis, I is the X-ray diffraction intensity, and f is the Herman's orientation factor. The Herman's orientation of T5 is 0.91 while it is 0.83 for T3, which explains the lower mechanical properties of T3. While the stress transfer to the SWNTs are similar in T5 and T3, due to lower PAN crystal orientation in T3, the PAN matrix tensile properties are lower.

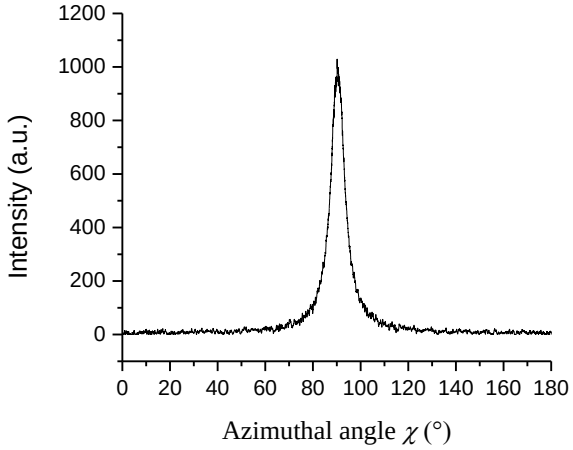

Figure 5-24. Azimuthal scan of (100) and (210) diffraction peak of T3 fiber.

5.3.7.2 Carbon Fiber

The mechanical properties of the carbon fibers from various trials are given in Table 5-3. It was found that dipping the fibers in spin finish prior to stabilization improved fiber separation for single filament testing. T-test with a confidence threshold of 0.05 was carried out to determine statistically significant trends in the data. The only trend confirmed from the t-test was the higher modulus, ~4 %, of all SWNT containing samples compared to control PAN. The average tensile strength of all samples was in the range of 2.4-2.8 GPa. Even though the precursor T3 fiber had lower mechanical properties compared to other fibers, due to less oriented PAN crystals, it had comparable carbon fiber properties. Various experimental variations complicate the comparison. Previous studies have concluded that mechanical degradation of the polymer under oxygen atmosphere is faster than under nitrogen purge [198]. There is a possibility that T5 solution had a lower molecular weight due to degradation. Mechanical degradation was also supported by lower viscosity of T5. Carbonization results of fibers from multi-filament spinning is presented in Appendix B. PAN fibers with molecular weight of 247,000 and 500,000 g/mol were batch carbonized. It can be concluded from Table B-1 that higher molecular weight PAN results in carbon fiber with better tensile strength.

The higher solid content of T3 resulted in lower PAN crystal alignment and larger diameter of the resulting fiber and precursor fiber. A larger fiber diameter/cross section translates to more defects at similar defect densities. Carbon fibers have a skin-core structure [203] which have different degree of graphitization [204] and likely different mechanical properties. Larger fiber diameter results in higher core to skin ratio. SEM images of T3 fiber which underwent similar stabilization scheme shows formation of

voids in the core of T3 carbon fiber (Figure 5-25), which is due to under-stabilization of the core. Further stabilization time to stabilize the core may lead to over-stabilization of the skin. The gradient in stabilization always exists, but is aggravated for larger diameters. Comparable mechanical properties of these various trials could be due to these competing factors (reduction in tensile strength of T5 carbon fiber due to broken PAN chains from mechanical degradation; reduction in tensile strength of T3 carbon fiber due to larger fiber diameter and less oriented crystal structure of precursor fiber). Considering the aforementioned issues, it is possible that higher mechanical properties could be achieved if PAN/SWNT/PMMA solution processed under nitrogen with 13 wt% solid content is used to make the fiber.

Table 5-3. Carbonization trials and tensile properties of PAN, PAN/SWNT and PAN/SWNT/PMMA fibers. Fiber was carbonized at 1300 °C for 5 minutes.

#	Temp. (°C)	RT* (min)	σ_1* (MPa)	σ_2* (MPa)	Diameter (μm)	Modulus (GPa)	Strength (GPa)	Elongation (%)
T1	266/305	120/10	40	40	7.3 ± 0.3	270 ± 6	2.7 ± 0.6	1.0 ± 0.3
T1	266/305	120/10	38	38	7.1 ± 0.4	269 ± 9	2.5 ± 0.3	0.9 ± 0.1
T2	266/305	120/10	40	40	7.1 ± 0.2	286 ± 6	2.6 ± 0.4	0.9 ± 0.1
T2	266/305	120/10	38	38	7.2 ± 0.2	281 ± 10	2.4 ± 0.3	0.9 ± 0.1
T3	266/305	180/10	41	41	8.4 ± 0.5	280 ± 6	2.6 ± 0.3	0.9 ± 0.2
T3	266/305	120/10	38	38	8.3 ± 0.6	283 ± 4	2.4 ± 0.2	0.9 ± 0.1
T5	266/305	120/10	40	40	6.9 ± 0.5	287 ±9	2.5 ± 0.5	0.8 ± 0.2
T5	266/305	120/10	39	39	7.2 ± 0.4	282 ± 7	2.7 ± 0.4	1.0 ± 0.1

* RT: residence time, σ_1: stabilization stress, σ_2: Carbonization stress

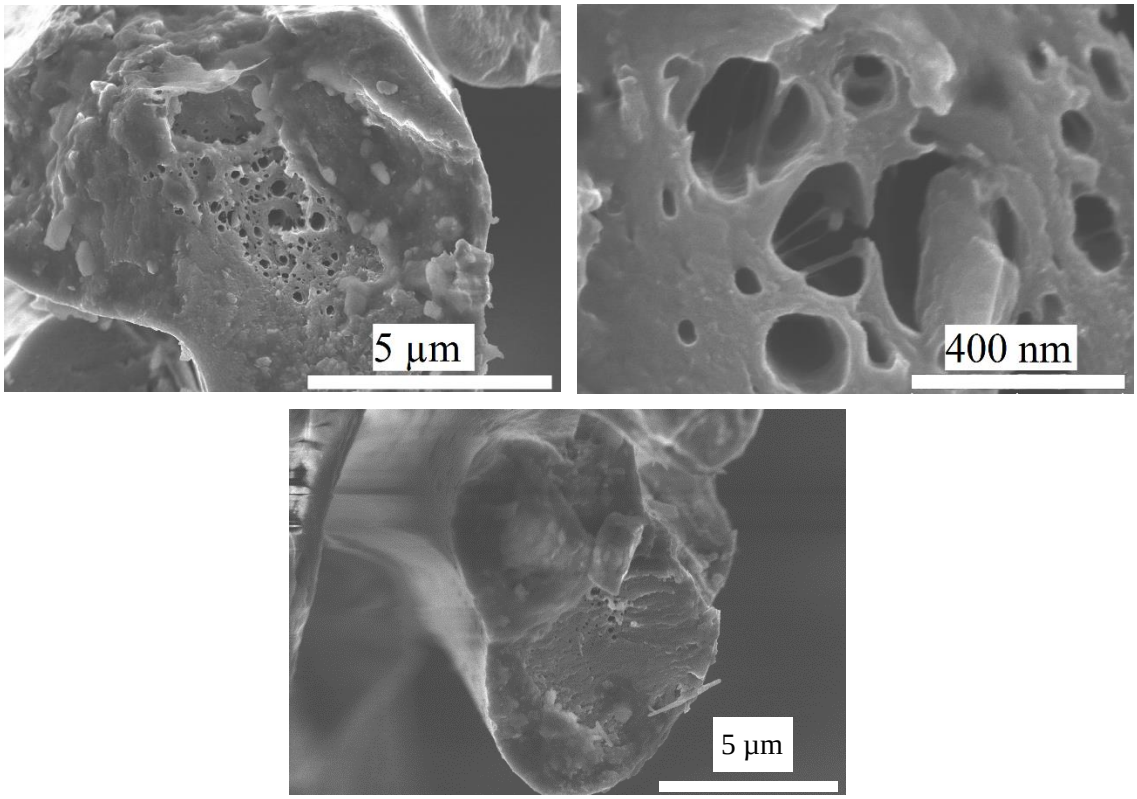

Figure 5-25. Carbon fiber cross section of trial T3. Stabilized at 266/305 °C for 120/10 minutes. Note a portion of the core has voids from incomplete stabilization.

5.3.8 Effect of Polymer Wrapping on Fibril Size

In the previous sections, we used RBM intensity analysis to deduce exfoliation of PMMA wrapped SWNTs, and bundling of non-wrapped SWNTs. Debundling of SWNTs reduces the bundle diameter. The carbon nanotubes form a fibrillar structure at the fracture surface of carbon nanotubes (Figure 5-26). For additional evidence regarding SWNT debundling, fibril diameter in the carbon fiber fracture surface was measured for the PMMA wrapped and non-wrapped carbon fibers (Figure 5-28 and Figure 5-27). The average fibril diameter was 12 ± 4 nm and 29 ± 6 nm for T5 and T2, respectively. The bundle diameter cannot be determined from SEM since the thickness of the graphitic

structure on SWNTs is unknown. Nonetheless, it is likely that the bundle diameter is smaller in the PMMA wrapped SWNTs (Figure 5-29). The bundle size can be determined by TEM.

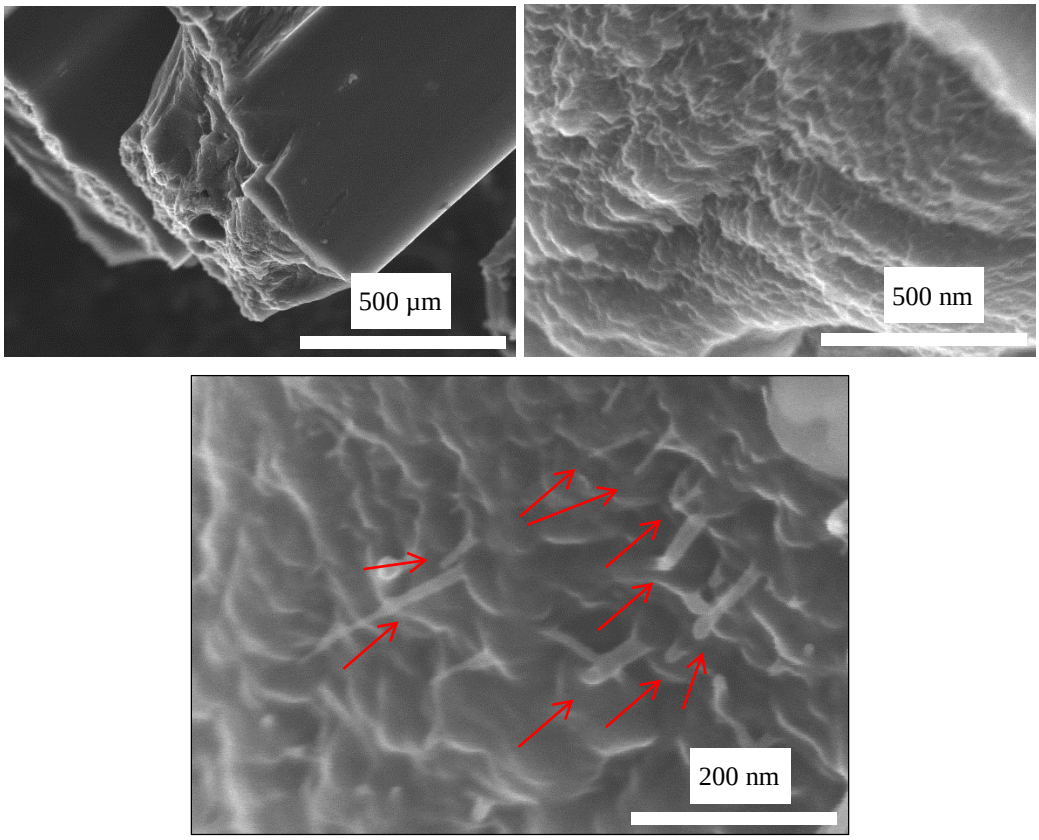

Figure 5-26. SEM image of T5 carbon fiber fracture surface. Fibrils are shown with red arrows.

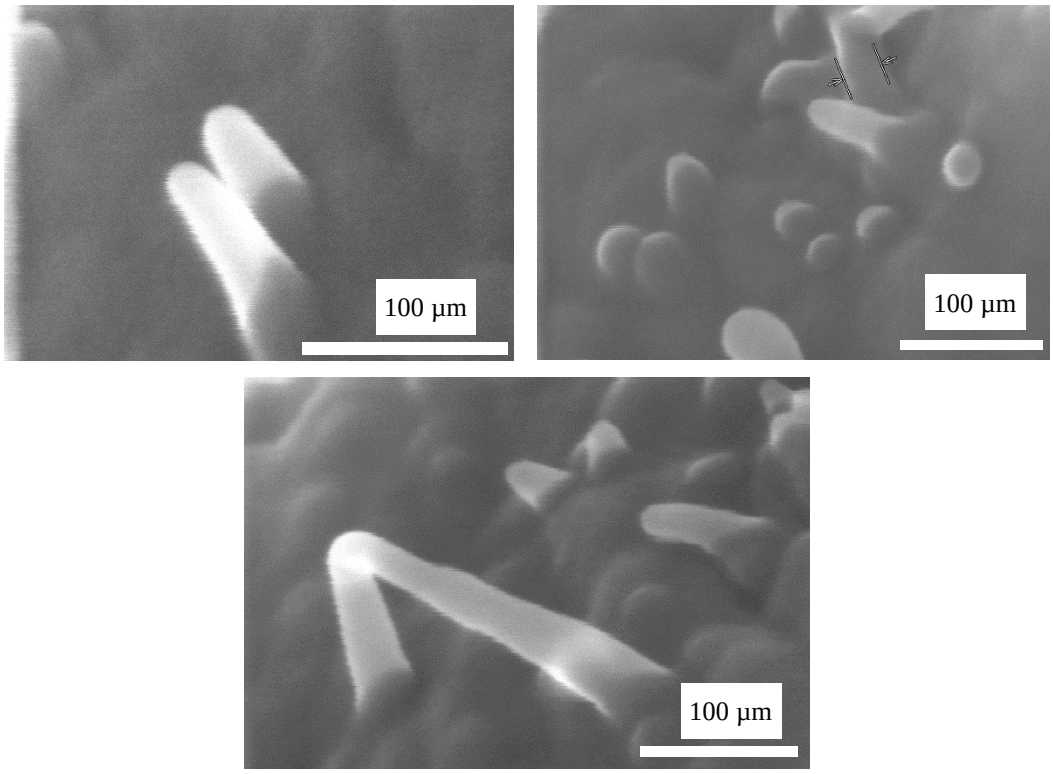

Figure 5-27. SEM images of T2 (PAN/SWNT) carbon fiber demonstrating fibril size.

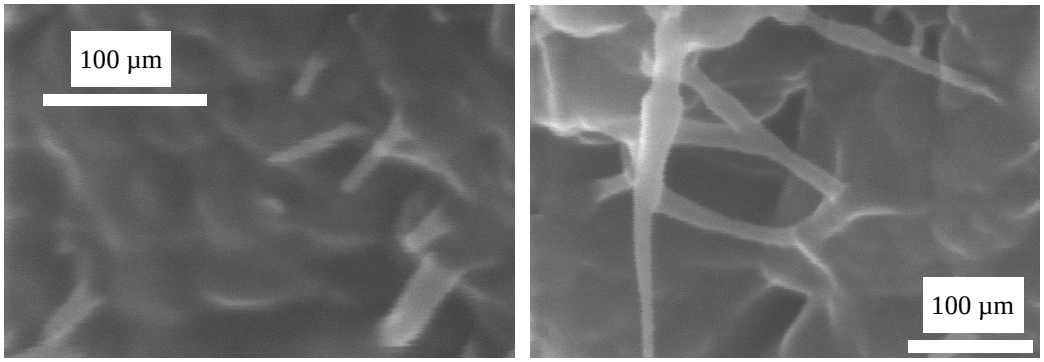

Figure 5-28. SEM images of T5 (PAN/SWNT/PMMA) carbon fiber demonstrating fibril size.

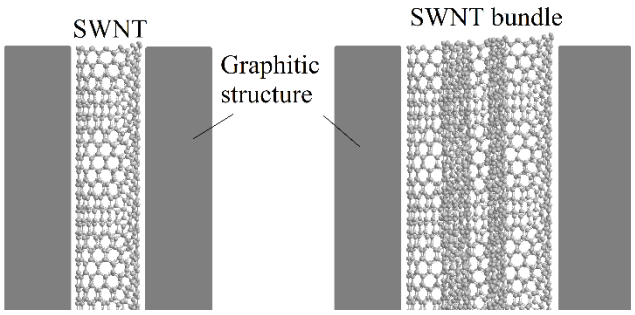

Figure 5-29. Schematic representation of fibril size from individual and bundled SWNTs.

5.4 Conclusions

Solutions and fibers with wrapped and non-wrapped SWNTs were prepared to study the effect of PMMA wrapping. PMMA wrapping resulted in better SWNT dispersion in PAN solutions and fibers as compared to SWNTs without PMMA wrapping. RBM analysis of the solution and precursor fiber confirms exfoliation of PMMA wrapped SWNTs while non-wrapped SWNTs are aggregated. The fibril size at the carbon fiber fracture surface were 60 % smaller when PMMA wrapped SWNTs were used compared to non-wrapped SWNTs. PMMA wrapped SWNTs also experienced higher stress compared to non-wrapped SWNTs in the precursor fiber. Based on the stress transfer analysis on the precursor fibers, the interfacial shear strength of the PMMA wrapped SWNTs with PAN was 48 ± 3 MPa compared to 33 ± 3 MPa for the non-wrapped SWNTs. So the interfacial shear strength increases 45 % upon wrapping the SWNTs with PMMA.

Drawing the fiber provided some interesting insight into the wrapping behavior. SWNT-SWNT interaction was studied by looking at the evolution of RBM peaks upon drawing. Upon drawing the PMMA wrapped SWNT containing PAN precursor fiber, SWNT-SWNT interaction increased. This increase can be explained by the hypothesis that PMMA chains linked several SWNTs together. Hence, while PMMA wrapping leads to debundled SWNTs, the SWNTs are kept in close proximity by PMMA chains. The non-wrapped SWNT containing PAN precursor fiber, exhibited a reduction in SWNT-SWNT interaction. Reduction of SWNT interaction is attributed to separation of aggregated bundles into smaller bundles, but the reduction was not indicative of debundling and exfoliation to near individual SWNTs.

The modulus and strength of precursor fiber with PMMA wrapped SWNTs were ~14 % and 8 %, respectively, higher than control PAN and PAN/SWNT fiber, which was attributed to improved stress transfer to PMMA wrapped SWNTs, while the control PAN and PAN/SWNT precursor fiber had comparable properties. The mechanical properties of the carbon fibers from various trials were comparable.

Processing PAN copolymer solution under air atmosphere did not lead to dehydrogenation of PAN or formation of C=C bonds at 90 °C after 72 hours. The IR spectra of the solution prepared under air at 90 °C was similar to that of solution prepared under nitrogen at 80 °C after 72 hours.

CHAPTER 6

CONCLUSIONS AND RECOMMENDATIONS

6.1 Conclusions

Carbon nanotubes tend to bundle due to the collective van der Waals interaction along the length of CNTs. We reported a technique to wrap SWNTs with PMMA. The wrapping only takes place around CNTs with a diameter of ~1 nm, and it does not occur with FWNTs or MWNTs. This has been attributed to the bond angles of the PMMA backbone which provide a hole sized for SWNTs, and favorable interaction between the CH_2 side chains of PMMA with SWNT and the polymer-solvent interactions. PMMA wraps in an ordered helical manner around SWNTs. This ordered PMMA results in a sharp peak in the X-ray diffraction. This peak was attributed to the spacing between adjacent PMMA chains of the helical structure; i.e. the pitch of the PMMA helix. The helical morphology of PMMA was confirmed by simulating the diffraction pattern of the proposed model, which was a good match with the experimental diffraction pattern.

The PMMA wrapping not only increases the suspendability of SWNTs in solvents from 0.014 mg/mL to more than 1 mg/mL, but also improves the suspension stability over the period of several months as compared to days for as sonicated SWNTs without PMMA wrapping. From UV-vis spectroscopy, we observed that all excitation bands of SWNTs blue shift upon being wrapped with PMMA. This is consistent with debundling of SWNTs, since SWNT van Hove singularities red shift upon bundling. From Raman

spectroscopy, it was observed that all chiralities are debundled when processed with PMMA, ruling out wrapping selectivity for the SWNTs probed with 785 nm laser. The effect of PMMA wrapping on the porous structure and specific surface area of SWNTs was studied. PMMA processed buckypapers had a specific surface area of more than 950 m^2/g, exhibiting a 50% increase in specific surface area than as sonicated SWNTs.

Altogether, all of the evidence such as increased suspendability, stability of suspensions, UV-vis and Raman spectroscopy analysis, X-ray diffraction pattern and simulation, and surface area analysis, support the PMMA wrapping of SWNTs. For the first time since the discovery of carbon nanotubes, a polymer has been found that wraps CNTs in an ordered manner.

The PMMA processed high surface area SWNT buckypapers were used as electrode for supercapacitors. In electrical double layer capacitors, energy is stored at the electrode-electrolyte interface. Therefore, by increasing specific surface area (SSA) higher energy density and power density should be delivered by the electrode. The PMMA processed SWNT buckypaper with a surface area of 950 m^2/g (referred to as HS-SWNT buckypaper) exhibited high energy density of 3.13 kWh/kg at a high power density of 84 kW/kg. At this high power density, the energy density is at least four times higher than the best value reported in the literature to-date for the carbon nanotube electrodes without pseudocapacitance. Carbon nanotube supercapacitor electrodes with specific surface area in the range of 300 to 950 m^2/g were fabricated to understand the influence of surface area on energy storage. This was achieved without introducing defects or functionalizing the nanotubes, and thus all the electrodes exhibited no pseudo capacitance. Capacitance exhibited good correlation with specific surface area,

Wrapping SWNTs with PMMA in buckypaper increases the modulus and tensile strength by a factor of 5.9 and 3.7 times, respectively, compared to pristine SWNT buckypaper. This increase is attributed to the debundling effect of the helical PMMA around SWNTs. The debundled SWNTs form a network of individual SWNTs that are more effective in transferring stress to the nanotubes in the buckypaper compared to bundled SWNTs in the pristine buckypaper. While SWNTs in the PMMA wrapped buckypaper experience 1 GPa stress, corresponding to 5 cm^{-1} shift of the G' Raman band, the SWNTs in the pristine buckypaper do not exhibit any shift of the G' Raman band. In composite films, stress is transferred from the matrix to SWNTs, hence higher stress transfer can be achieved by maximizing the SWNT-PMMA interface by debundling the SWNTs. SWNTs in the PMMA wrapped SWNT composite experience 3.1 GPa stress, twice as much stress as the SWNTs in the non-wrapped SWNT film, which results in up to 75% higher modulus in wrapped SWNT films compared to non-wrapped SWNT films.

Solutions and fibers with wrapped and non-wrapped SWNTs were prepared to study the effect of PMMA wrapping. PMMA wrapping resulted in better SWNT dispersion in PAN solutions and fibers as compared to SWNTs without PMMA wrapping. RBM analysis of the solution and precursor fiber confirms exfoliation of PMMA wrapped SWNTs while non-wrapped SWNTs are aggregated. The fibril size at the carbon fiber fracture surface were 60 % smaller when PMMA wrapped SWNTs were used compared to non-wrapped SWNTs. PMMA wrapped SWNTs also experienced higher stress compared to non-wrapped SWNTs in the precursor fiber. Based on the stress transfer analysis on the precursor fibers, the interfacial shear strength of the PMMA

wrapped SWNTs was 48 MPa while the non-wrapped SWNTs were 33 MPa; 45 % higher interfacial shear strength upon wrapping the SWNTs with PMMA.

Drawing the fiber provided some interesting insight into the wrapping behavior. SWNT-SWNT interaction was studied by looking at the evolution of RBM peaks upon drawing. Upon drawing the PMMA wrapped SWNT fiber, SWNT-SWNT interaction increased. This increase can be explained by the hypothesis that PMMA chains linked several SWNTs together. Hence, while PMMA wrapping leads to debundled SWNTs, the SWNTs are kept in close proximity by PMMA chains. The non-wrapped SWNT fiber, exhibited a reduction in SWNT-SWNT interaction. Reduction of SWNT interaction is attributed to separation of aggregated bundles into smaller bundles, but the reduction was not indicative of debundling and exfoliation to near individual SWNTs.

The modulus and strength of precursor fiber with PMMA wrapped SWNTs were ~14 % and 8 %, respectively, higher than control PAN and PAN/SWNT fiber, which was attributed to improved stress transfer to PMMA wrapped SWNTs, while the control PAN and PAN/SWNT precursor fiber had comparable properties. The tensile modulus of SWNT containing carbon fibers was ~5 % higher than control PAN carbon fiber.

Processing PAN copolymer solution under air atmosphere did not lead to dehydrogenation of PAN or formation of C=C bonds at 90 °C after 72 hours. The IR spectra of the solution prepared under air at 90 °C was similar to that of solution prepared under nitrogen at 80 °C after 72 hours. The viscosity of the PAN/SWNT/PMMA solution prepared under air atmosphere (T5) was 40 % lower than the viscosity of the

PAN/SWNT solution (T2) prepared under nitrogen, despite 5 % higher solid content in T5 solution.

6.2 Recommendations for Future Study

1. High surface area buckypapers can be used as a platform for other energy storage devices. After removing the PMMA, the SWNTs can be coated with metal-oxides that have very high capacitance, such as vanadium oxide. If the coating does not block the porous structure, the high specific surface area and electrical conductivity of the PMMA processed SWNT buckypaper coupled with the high capacitance of the metal oxide can provide very high power and energy density. If the pores become blocked by depositing a layer of metal oxides, polyacrylates with larger side chains, such as poly(butyl methacrylate), can be used to wrap the SWNTs. The advantage of larger side chains is that it will leave larger pores after removal of the polymer.
2. Evidence suggests that a single PMMA chain may wrap several SWNTs and link them together, similar to an interconnected sausage link. Under the right conditions, it may be possible to form an interconnected network of SWNTs that have been linked by PMMA chains. Parameters such as PMMA molecular weight, SWNT and PMMA concentration and sonication time should be optimized to ensure a 3D network of SWNTs connected by PMMA. This interconnected network may have interesting applications, such as a scaffold for medical use. In addition, it may be possible to spin fibers from such a SWNT network.
3. Covalent functionalization of SWNTs and multi walled CNTs have been studied in detail in literature. However, mechanical properties do not greatly improve by the covalent bonds. To enhance the integrity of the SWNT/PMMA buckypaper, cross

linking of helical PMMA may provide a route to stronger buckypapers. The PMMA wrapping will transfer the load effectively to SWNTs, while preventing the SWNTs from participating in the functionalization so SWNTs retain their mechanical integrity.

APPENDIX A

PMMA/MWNT FIBER

Poly(methyl methacrylate) (PMMA) solution was prepared by dissolving 31 g PMMA (MW= 350,000 g/mol) in 100 mL DMF. PMMA/multi wall nanotubes (MWNT) solution was prepared by dissolving 30 g PMMA to 100 mL DMF. 55 mg MWNT (average diameter 25 nm, purity 95 %, Cheaptubes Inc.) was sonicated in 300 mL DMF and added to the reactor. Distillation was carried out under vacuum at 80 °C. 300 mg MWNT in total was added to the PMMA solution, resulting in 1 wt% MWNT PAN fiber. All fibers were spun with a 200 μm spinneret into methanol coagulation bath at room temperature with an air gap of ~ 5 cm and a spin draw ratio of 8. MWNT aggregates are visible from optical micrographs (Figure A-1). MWNT reinforced PMMA fiber has 5 % and 19 % higher modulus and strength, respectively, compared to the neat PMMA fiber (Table A-1). The increase in modulus upon addition of CNTs is small considering that the CNTs are oriented along the fiber length.

.

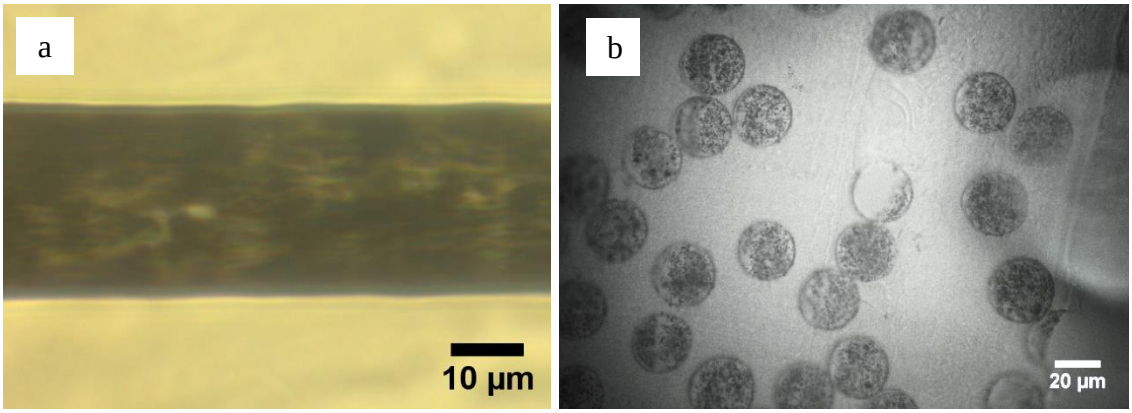

Figure A-1. Optical micrographs of PMMA/MWNT fiber, a) side view, and b) cross section. Inhomogeneity of MWNT dispersion can be seen as changes in transmission in the fiber side view, and aggregates in the cross section.

Table A-1. Mechanical properties of PMMA and PMMA/MWNT fibers.

Fiber	MWNT (wt %)	Diameter (µm)	Modulus (GPa)	Strength (MPa)	Elongation at break (%)
PMMA	0	25.5 ± 1	3.5 ± 0.2	86.5 ± 2.2	23.6 ± 2.4
PMMA/MWNT	1	25.9 ± 2.2	3.7 ± 0.2	103.1 ± 5.5	13.5 ± 1.5

APPENDIX B

MECHANICAL PROPERTIES OF FIBERS FROM MULTI-FILAMENT SPINNING

Fibers from multi-filament spinning were carbonized using the batch process. Precursor PAN fibers spun from PAN with molecular weight of 247,000 (247k) and 500,000 (500k) g/mol were used. The tensile strength of the 500k carbon fiber was 17 % higher than the 247k carbon fiber, while the modulus was similar (Table B-1). Tensile strength and modulus of carbon fiber from continuous carbonization of the 500k fiber was 62 % and 17 % higher, respectively, than the same fiber carbonized using the batch process (Table B-2).

Table B-1. Mechanical properties of carbon fibers from multi-filament spinning by batch carbonization. Two fibers with molecular weights of 247,000 and 500,000 g/mol were carbonized. Carbonization carried out at 1300 and held at that temperature for 5 minutes.

MW (g/mol)	Temp. (°C)	RT* (min)	σ_1* (MPa)	σ_2* (MPa)	Diameter (μm)	Modulus (GPa)	Strength (GPa)	Elongation (%)
247,000	270/310	120/9	38	38	6.8 ± 0.4	284 ± 15	2.9 ± 0.7	1.1 ± 0.4
500,000	275/320	120/20	34.5	18	6.3 ± 0.6	283 ± 8	3.4 ± 0.8	1.2 ± 0.3

* RT: residence time, σ_1: stabilization stress, σ_2: Carbonization stress

Table B-2. Mechanical properties of carbon fiber from multi-filament spinning by continuous carbonization (Trial number 140S3D1-c).

MW (g/mol)	Diameter (μm)	Modulus (GPa)	Strength (GPa)	Elongation (%)
500,000	5.2 ± 0.3	330 ± 9	5.5 ± 1.8	1.65 ± 0.52

REFERENCES

1. Bauhofer, W. and J.Z. Kovacs, *A review and analysis of electrical percolation in carbon nanotube polymer composites.* Composites Science and Technology, 2009. **69**(10): p. 1486-1498.

2. Kroto, H.W., J.R. Heath, S.C. O'Brien, R.F. Curl, and R.E. Smalley, *C60: Buckminsterfullerene.* Nature, 1985. **318**(6042): p. 162-163.

3. Iijima, S., *Helical microtubules of graphitic carbon.* Nature, 1991. **354**(6348): p. 56-58.

4. Ebbesen, T.W. and P.M. Ajayan, *Large-scale synthesis of carbon nanotubes.* Nature, 1992. **358**(6383): p. 220-222.

5. Guo, T., P. Nikolaev, A. Thess, D.T. Colbert, and R.E. Smalley, *Catalytic growth of single-walled manotubes by laser vaporization.* Chemical Physics Letters, 1995. **243**(1–2): p. 49-54.

6. José-Yacamán, M., M. Miki-Yoshida, L. Rendón, and J.G. Santiesteban, *Catalytic growth of carbon microtubules with fullerene structure.* Applied Physics Letters, 1993. **62**(6): p. 657-659.

7. Yang, F., X. Wang, D. Zhang, J. Yang, LuoDa, Z. Xu, J. Wei, J.-Q. Wang, Z. Xu, F. Peng, X. Li, R. Li, Y. Li, M. Li, X. Bai, F. Ding, and Y. Li, *Chirality-specific growth of single-walled carbon nanotubes on solid alloy catalysts.* Nature, 2014. **510**(7506): p. 522-524.

8. Wang, H., Y. Yuan, L. Wei, K. Goh, D. Yu, and Y. Chen, *Catalysts for chirality selective synthesis of single-walled carbon nanotubes.* Carbon, 2015. **81**: p. 1-19.

9. *http://teachers.yale.edu/curriculum/viewer/initiative_10.05.07_u*. 2015].

10. Liu, J., T. Liu, and S. Kumar, *Effect of solvent solubility parameter on SWNT dispersion in PMMA.* Polymer, 2005. **46**(10): p. 3419-3424.

11. Luo, S., T. Liu, and B. Wang, *Comparison of ultrasonication and microfluidization for high throughput and large-scale processing of SWCNT dispersions.* Carbon, 2010. **48**(10): p. 2992-2994.

12. Badaire, S., P. Poulin, M. Maugey, and C. Zakri, *In Situ Measurements of Nanotube Dimensions in Suspensions by Depolarized Dynamic Light Scattering.* Langmuir, 2004. **20**(24): p. 10367-10370.

13. Rastogi, R., R. Kaushal, S.K. Tripathi, A.L. Sharma, I. Kaur, and L.M. Bharadwaj, *Comparative study of carbon nanotube dispersion using surfactants.* Journal of Colloid and Interface Science, 2008. **328**(2): p. 421-428.

14. Matarredona, O., H. Rhoads, Z. Li, J.H. Harwell, L. Balzano, and D.E. Resasco, *Dispersion of Single-Walled Carbon Nanotubes in Aqueous Solutions of the Anionic Surfactant NaDDBS.* The Journal of Physical Chemistry B, 2003. **107**(48): p. 13357-13367.

15. Ma, P.-C., N.A. Siddiqui, G. Marom, and J.-K. Kim, *Dispersion and functionalization of carbon nanotubes for polymer-based nanocomposites: A review.* Composites Part A: Applied Science and Manufacturing, 2010. **41**(10): p. 1345-1367.

16. Zhu, J., J. Kim, H. Peng, J.L. Margrave, V.N. Khabashesku, and E.V. Barrera, *Improving the Dispersion and Integration of Single-Walled Carbon Nanotubes in Epoxy Composites through Functionalization.* Nano Letters, 2003. **3**(8): p. 1107-1113.

17. Worsley, K.A., I. Kalinina, E. Bekyarova, and R.C. Haddon, *Functionalization and Dissolution of Nitric Acid Treated Single-Walled Carbon Nanotubes.* Journal of the American Chemical Society, 2009. **131**(50): p. 18153-18158.

18. Dyke, C.A. and J.M. Tour, *Overcoming the Insolubility of Carbon Nanotubes Through High Degrees of Sidewall Functionalization.* Chemistry – A European Journal, 2004. **10**(4): p. 812-817.

19. Star, A., J.F. Stoddart, D. Steuerman, M. Diehl, A. Boukai, E.W. Wong, X. Yang, S.-W. Chung, H. Choi, and J.R. Heath, *Preparation and Properties of Polymer-Wrapped Single-Walled Carbon Nanotubes.* Angewandte Chemie International Edition, 2001. **40**(9): p. 1721-1725.

20. Haggenmueller, R., H.H. Gommans, A.G. Rinzler, J.E. Fischer, and K.I. Winey, *Aligned single-wall carbon nanotubes in composites by melt processing methods.* Chemical Physics Letters, 2000. **330**(3–4): p. 219-225.

21. McClory, C., T. McNally, M. Baxendale, P. Pötschke, W. Blau, and M. Ruether, *Electrical and rheological percolation of PMMA/MWCNT nanocomposites as a function of CNT geometry and functionality.* European Polymer Journal, 2010. **46**(5): p. 854-868.

22. Jia, Z., Z. Wang, C. Xu, J. Liang, B. Wei, D. Wu, and S. Zhu, *Study on poly(methyl methacrylate)/carbon nanotube composites.* Materials Science and Engineering: A, 1999. **271**(1–2): p. 395-400.

23. Wu, H.-X., X.-Q. Qiu, W.-M. Cao, Y.-H. Lin, R.-F. Cai, and S.-X. Qian, *Polymer-wrapped multiwalled carbon nanotubes synthesized via microwave-*

assisted in situ emulsion polymerization and their optical limiting properties. Carbon, 2007. **45**(15): p. 2866-2872.

24. Clayton, L.M., A.K. Sikder, A. Kumar, M. Cinke, M. Meyyappan, T.G. Gerasimov, and J.P. Harmon, *Transparent Poly(methyl methacrylate)/Single-Walled Carbon Nanotube (PMMA/SWNT) Composite Films with Increased Dielectric Constants.* Advanced Functional Materials, 2005. **15**(1): p. 101-106.

25. Patole, A.S., S.P. Patole, J.-B. Yoo, J.-H. An, and T.-H. Kim, *Fabrication of polystyrene/multiwalled carbon nanotube composite films synthesized by in situ microemulsion polymerization.* Polymer Engineering & Science, 2013. **53**(6): p. 1327-1336.

26. Jain, R., Y.H. Choi, Y. Liu, M.L. Minus, H.G. Chae, S. Kumar, and J.-B. Baek, *Processing, structure and properties of poly(ether ketone) grafted few wall carbon nanotube composite fibers.* Polymer, 2010. **51**(17): p. 3940-3947.

27. Peigney, A., C. Laurent, E. Flahaut, R.R. Bacsa, and A. Rousset, *Specific surface area of carbon nanotubes and bundles of carbon nanotubes.* Carbon, 2001. **39**(4): p. 507-514.

28. Bacsa, R.R., C. Laurent, A. Peigney, W.S. Bacsa, T. Vaugien, and A. Rousset, *High specific surface area carbon nanotubes from catalytic chemical vapor deposition process.* Chemical Physics Letters, 2000. **323**(5–6): p. 566-571.

29. Hernadi, K., A. Fonseca, J.B. Nagy, D. Bemaerts, A. Fudala, and A.A. Lucas, *Catalytic synthesis of carbon nanotubes using zeolite support.* Zeolites, 1996. **17**(5–6): p. 416-423.

30. Izadi-Najafabadi, A., T. Yamada, D.N. Futaba, M. Yudasaka, H. Takagi, H. Hatori, S. Iijima, and K. Hata, *High-Power Supercapacitor Electrodes from Single-Walled Carbon Nanohorn/Nanotube Composite.* ACS Nano, 2011. **5**(2): p. 811-819.

31. Futaba, D.N., K. Hata, T. Yamada, T. Hiraoka, Y. Hayamizu, Y. Kakudate, O. Tanaike, H. Hatori, M. Yumura, and S. Iijima, *Shape-engineerable and highly densely packed single-walled carbon nanotubes and their application as super-capacitor electrodes.* Nat Mater, 2006. **5**(12): p. 987-994.

32. Muramatsu, H., T. Hayashi, Y.A. Kim, D. Shimamoto, Y.J. Kim, K. Tantrakarn, M. Endo, M. Terrones, and M.S. Dresselhaus, *Pore structure and oxidation stability of double-walled carbon nanotube-derived bucky paper.* Chemical Physics Letters, 2005. **414**(4–6): p. 444-448.

33. Gerstel, P., S. Klumpp, F. Hennrich, A. Poschlad, V. Meded, E. Blasco, W. Wenzel, M.M. Kappes, and C. Barner-Kowollik, *Highly Selective Dispersion of Single-Walled Carbon Nanotubes via Polymer Wrapping: A Combinatorial Study via Modular Conjugation.* ACS Macro Letters, 2013. **3**(1): p. 10-15.

34. Xu, W., J. Zhao, L. Qian, X. Han, L. Wu, W. Wu, M. Song, L. Zhou, W. Su, C. Wang, S. Nie, and Z. Cui, *Sorting of large-diameter semiconducting carbon nanotube and printed flexible driving circuit for organic light emitting diode (OLED).* Nanoscale, 2014. **6**(3): p. 1589-1595.

35. Nish, A., J.-Y. Hwang, J. Doig, and R.J. Nicholas, *Highly selective dispersion of single-walled carbon nanotubes using aromatic polymers.* Nat Nano, 2007. **2**(10): p. 640-646.

36. Joo, Y., G.J. Brady, M.S. Arnold, and P. Gopalan, *Dose-Controlled, Floating Evaporative Self-assembly and Alignment of Semiconducting Carbon Nanotubes from Organic Solvents.* Langmuir, 2014. **30**(12): p. 3460-3466.

37. Tang, B.Z. and H. Xu, *Preparation, Alignment, and Optical Properties of Soluble Poly(phenylacetylene)-Wrapped Carbon Nanotubes.* Macromolecules, 1999. **32**(8): p. 2569-2576.

38. O'Connell, M.J., P. Boul, L.M. Ericson, C. Huffman, Y. Wang, E. Haroz, C. Kuper, J. Tour, K.D. Ausman, and R.E. Smalley, *Reversible water-solubilization of single-walled carbon nanotubes by polymer wrapping.* Chemical Physics Letters, 2001. **342**(3–4): p. 265-271.

39. Kang, Y.K., O.-S. Lee, P. Deria, S.H. Kim, T.-H. Park, D.A. Bonnell, J.G. Saven, and M.J. Therien, *Helical Wrapping of Single-Walled Carbon Nanotubes by Water Soluble Poly(p-phenyleneethynylene).* Nano Letters, 2009. **9**(4): p. 1414-1418.

40. Deria, P., C.D. Von Bargen, J.-H. Olivier, A.S. Kumbhar, J.G. Saven, and M.J. Therien, *Single-Handed Helical Wrapping of Single-Walled Carbon Nanotubes by Chiral, Ionic, Semiconducting Polymers.* Journal of the American Chemical Society, 2013. **135**(43): p. 16220-16234.

41. Zheng, M., A. Jagota, E.D. Semke, B.A. Diner, R.S. McLean, S.R. Lustig, R.E. Richardson, and N.G. Tassi, *DNA-assisted dispersion and separation of carbon nanotubes.* Nat Mater, 2003. **2**(5): p. 338-342.

42. Zheng, M., A. Jagota, M.S. Strano, A.P. Santos, P. Barone, S.G. Chou, B.A. Diner, M.S. Dresselhaus, R.S. Mclean, G.B. Onoa, G.G. Samsonidze, E.D. Semke, M. Usrey, and D.J. Walls, *Structure-Based Carbon Nanotube Sorting by Sequence-Dependent DNA Assembly.* Science, 2003. **302**(5650): p. 1545-1548.

43. Fujigaya, T., M. Okamoto, and N. Nakashima, *Design of an assembly of pyridine-containing polybenzimidazole, carbon nanotubes and Pt nanoparticles for a fuel cell electrocatalyst with a high electrochemically active surface area.* Carbon, 2009. **47**(14): p. 3227-3232.

44. Shigeta, M., M. Komatsu, and N. Nakashima, *Individual solubilization of single-walled carbon nanotubes using totally aromatic polyimide.* Chemical Physics Letters, 2006. **418**(1–3): p. 115-118.

45. Yi, W., A. Malkovskiy, Q. Chu, A.P. Sokolov, M.L. Colon, M. Meador, and Y. Pang, *Wrapping of Single-Walled Carbon Nanotubes by a π-Conjugated Polymer: The Role of Polymer Conformation-Controlled Size Selectivity.* The Journal of Physical Chemistry B, 2008. **112**(39): p. 12263-12269.

46. Lee, H.W., Y. Yoon, S. Park, J.H. Oh, S. Hong, L.S. Liyanage, H. Wang, S. Morishita, N. Patil, Y.J. Park, J.J. Park, A. Spakowitz, G. Galli, F. Gygi, P.H.S. Wong, J.B.H. Tok, J.M. Kim, and Z. Bao, *Selective dispersion of high purity semiconducting single-walled carbon nanotubes with regioregular poly(3-alkylthiophene)s.* Nat Commun, 2011. **2**: p. 541.

47. Chen, F., B. Wang, Y. Chen, and L.-J. Li, *Toward the Extraction of Single Species of Single-Walled Carbon Nanotubes Using Fluorene-Based Polymers.* Nano Letters, 2007. **7**(10): p. 3013-3017.

48. Du, F., J.E. Fischer, and K.I. Winey, *Coagulation method for preparing single-walled carbon nanotube/poly(methyl methacrylate) composites and their modulus, electrical conductivity, and thermal stability.* Journal of Polymer Science Part B: Polymer Physics, 2003. **41**(24): p. 3333-3338.

49. Liu, J., A. Rasheed, M.L. Minus, and S. Kumar, *Processing and properties of carbon nanotube/poly(methyl methacrylate) composite films.* Journal of Applied Polymer Science, 2009. **112**(1): p. 142-156.

50. Tallury, S.S. and M.A. Pasquinelli, *Molecular Dynamics Simulations of Flexible Polymer Chains Wrapping Single-Walled Carbon Nanotubes.* The Journal of Physical Chemistry B, 2010. **114**(12): p. 4122-4129.

51. Kawauchi, T., J. Kumaki, A. Kitaura, K. Okoshi, H. Kusanagi, K. Kobayashi, T. Sugai, H. Shinohara, and E. Yashima, *Encapsulation of Fullerenes in a Helical PMMA Cavity Leading to a Robust Processable Complex with a Macromolecular Helicity Memory.* Angewandte Chemie, 2008. **120**(3): p. 525-529.

52. *https://e2e.ti.com/blogs_/b/fullycharged/archive/2015/07/17/supercapacitors*. 2015].

53. Endo, M., T. Maeda, T. Takeda, Y.J. Kim, K. Koshiba, H. Hara, and M.S. Dresselhaus, *Capacitance and Pore-Size Distribution in Aqueous and Nonaqueous Electrolytes Using Various Activated Carbon Electrodes.* Journal of The Electrochemical Society, 2001. **148**(8): p. A910-A914.

54. Qu, D., *Studies of the activated carbons used in double-layer supercapacitors.* Journal of Power Sources, 2002. **109**(2): p. 403-411.

55. Jiang, Q., M.Z. Qu, G.M. Zhou, B.L. Zhang, and Z.L. Yu, *A study of activated carbon nanotubes as electrochemical super capacitors electrode materials.* Materials Letters, 2002. **57**(4): p. 988-991.

56. Vivekchand, S.R.C., C. Rout, K.S. Subrahmanyam, A. Govindaraj, and C.N.R. Rao, *Graphene-based electrochemical supercapacitors.* Journal of Chemical Sciences, 2008. **120**(1): p. 9-13.

57. Stoller, M.D., S. Park, Y. Zhu, J. An, and R.S. Ruoff, *Graphene-Based Ultracapacitors.* Nano Letters, 2008. **8**(10): p. 3498-3502.

58. Wang, Y., Z. Shi, Y. Huang, Y. Ma, C. Wang, M. Chen, and Y. Chen, *Supercapacitor Devices Based on Graphene Materials.* The Journal of Physical Chemistry C, 2009. **113**(30): p. 13103-13107.

59. Niu, C., E.K. Sichel, R. Hoch, D. Moy, and H. Tennent, *High power electrochemical capacitors based on carbon nanotube electrodes.* Applied Physics Letters, 1997. **70**(11): p. 1480.

60. Frackowiak, E., K. Jurewicz, S. Delpeux, and F. Beguin, *Electrochemical Application of Carbon Nanotubes*, in *Low-Dimensional Systems: Theory, Preparation, and Some Applications*, L. Liz-Marzán and M. Giersig, Editors. 2003, Springer Netherlands. p. 305-318.

61. Gamby, J., P.L. Taberna, P. Simon, J.F. Fauvarque, and M. Chesneau, *Studies and characterisations of various activated carbons used for carbon/carbon supercapacitors.* Journal of Power Sources, 2001. **101**(1): p. 109-116.

62. Lin, C., J.A. Ritter, and B.N. Popov, *Correlation of Double-Layer Capacitance with the Pore Structure of Sol-Gel Derived Carbon Xerogels.* Journal of The Electrochemical Society, 1999. **146**(10): p. 3639-3643.

63. Garcia, B.B., S.L. Candelaria, D. Liu, S. Sepheri, J.A. Cruz, and G. Cao, *High performance high-purity sol-gel derived carbon supercapacitors from renewable sources.* Renewable Energy, 2011. **36**(6): p. 1788-1794.

64. Li, W., G. Reichenauer, and J. Fricke, *Carbon aerogels derived from cresol–resorcinol–formaldehyde for supercapacitors.* Carbon, 2002. **40**(15): p. 2955-2959.

65. Zhou, C., T. Liu, T. Wang, and S. Kumar, *PAN/SAN/SWNT ternary composite: Pore size control and electrochemical supercapacitor behavior.* Polymer, 2006. **47**(16): p. 5831-5837.

66. Kalpana, D., K.S. Omkumar, S.S. Kumar, and N.G. Renganathan, *A novel high power symmetric ZnO/carbon aerogel composite electrode for electrochemical supercapacitor.* Electrochimica Acta, 2006. **52**(3): p. 1309-1315.

67. Carlson, T., D. Ordéus, M. Wysocki, and L.E. Asp, *Structural capacitor materials made from carbon fibre epoxy composites.* Composites Science and Technology, 2010. **70**(7): p. 1135-1140.

68. Qu, D. and H. Shi, *Studies of activated carbons used in double-layer capacitors.* Journal of Power Sources, 1998. **74**(1): p. 99-107.

69. Tamai, H., M. Kouzu, M. Morita, and H. Yasuda, *Highly Mesoporous Carbon Electrodes for Electric Double-Layer Capacitors.* Electrochemical and Solid-State Letters, 2003. **6**(10): p. A214-A217.

70. Barbieri, O., M. Hahn, A. Herzog, and R. Kötz, *Capacitance limits of high surface area activated carbons for double layer capacitors.* Carbon, 2005. **43**(6): p. 1303-1310.

71. Lin, J., C. Zhang, Z. Yan, Y. Zhu, Z. Peng, R.H. Hauge, D. Natelson, and J.M. Tour, *3-Dimensional Graphene Carbon Nanotube Carpet-Based Microsupercapacitors with High Electrochemical Performance.* Nano Letters, 2013. **13**(1): p. 72-78.

72. Zhu, Y., L. Li, C. Zhang, G. Casillas, Z. Sun, Z. Yan, G. Ruan, Z. Peng, A.-R.O. Raji, C. Kittrell, R.H. Hauge, and J.M. Tour, *A seamless three-dimensional carbon nanotube graphene hybrid material.* Nat Commun, 2012. **3**: p. 1225.

73. Pham, D.T., T.H. Lee, D.H. Luong, F. Yao, A. Ghosh, V.T. Le, T.H. Kim, B. Li, J. Chang, and Y.H. Lee, *Carbon Nanotube-Bridged Graphene 3D Building Blocks for Ultrafast Compact Supercapacitors.* ACS Nano, 2015. **9**(2): p. 2018-2027.

74. Fan, Z., J. Yan, L. Zhi, Q. Zhang, T. Wei, J. Feng, M. Zhang, W. Qian, and F. Wei, *A Three-Dimensional Carbon Nanotube/Graphene Sandwich and Its Application as Electrode in Supercapacitors.* Advanced Materials, 2010. **22**(33): p. 3723-3728.

75. Barisci, J.N., W.G. G., and R.H. Baughman, *Electrochemical studies of single-wall carbon nanotubes in aqueous solutions.* Journal of Electroanalytical Chemistry, 2000. **488**(2): p. 92-98.

76. Zhou, C., S. Kumar, C.D. Doyle, and J.M. Tour, *Functionalized Single Wall Carbon Nanotubes Treated with Pyrrole for Electrochemical Supercapacitor Membranes.* Chemistry of Materials, 2005. **17**(8): p. 1997-2002.

77. Yoon, B.-J., S.-H. Jeong, K.-H. Lee, H. Seok Kim, C. Gyung Park, and J. Hun Han, *Electrical properties of electrical double layer capacitors with integrated carbon nanotube electrodes.* Chemical Physics Letters, 2004. **388**(1–3): p. 170-174.

78. Lu, W., L. Qu, K. Henry, and L. Dai, *High performance electrochemical capacitors from aligned carbon nanotube electrodes and ionic liquid electrolytes.* Journal of Power Sources, 2009. **189**(2): p. 1270-1277.

79. Frackowiak, E., K. Metenier, V. Bertagna, and F. Beguin, *Supercapacitor electrodes from multiwalled carbon nanotubes.* Applied Physics Letters, 2000. **77**(15): p. 2421-2423.

80. Frackowiak, E., S. Delpeux, K. Jurewicz, K. Szostak, D. Cazorla-Amoros, and F. Béguin, *Enhanced capacitance of carbon nanotubes through chemical activation.* Chemical Physics Letters, 2002. **361**(1–2): p. 35-41.

81. Boukhalfa, S., K. Evanoff, and G. Yushin, *Atomic layer deposition of vanadium oxide on carbon nanotubes for high-power supercapacitor electrodes.* Energy & Environmental Science, 2012. **5**(5): p. 6872-6879.

82. Huang, J., B.G. Sumpter, and V. Meunier, *A Universal Model for Nanoporous Carbon Supercapacitors Applicable to Diverse Pore Regimes, Carbon Materials, and Electrolytes.* Chemistry – A European Journal, 2008. **14**(22): p. 6614-6626.

83. Galiński, M., A. Lewandowski, and I. Stępniak, *Ionic liquids as electrolytes.* Electrochimica Acta, 2006. **51**(26): p. 5567-5580.

84. Coleman, J.N., U. Khan, and Y.K. Gun'ko, *Mechanical Reinforcement of Polymers Using Carbon Nanotubes.* Advanced Materials, 2006. **18**(6): p. 689-706.

85. Ayatollahi, M.R., S. Shadlou, M.M. Shokrieh, and M. Chitsazzadeh, *Effect of multi-walled carbon nanotube aspect ratio on mechanical and electrical properties of epoxy-based nanocomposites.* Polymer Testing, 2011. **30**(5): p. 548-556.

86. Cox, H.L., *The elasticity and strength of paper and other fibrous materials.* British Journal of Applied Physics, 1952. **3**(3): p. 72.

87. Abu Al-Rub, R.K., A.I. Ashour, and B.M. Tyson, *On the aspect ratio effect of multi-walled carbon nanotube reinforcements on the mechanical properties of cementitious nanocomposites.* Construction and Building Materials, 2012. **35**(0): p. 647-655.

88. Zygon, P., M. Gwozdzik, J. Peszke, and Z. Nitkiewicz, *COMPARISON OF PROPERTIES OF POLYMER COMPOSITE MATERIALS REINFORCED WITH CARBON NANOTUBES.* Archives of Metallurgy and Materials, 2015. **60**(1): p. 193-198.

89. Rahmat, M. and P. Hubert, *Carbon nanotube-polymer interactions in nanocomposites: A review.* Composites Science and Technology, 2011. **72**(1): p. 72-84.

90. Moniruzzaman, M. and K.I. Winey, *Polymer nanocomposites containing carbon nanotubes.* Macromolecules, 2006. **39**(16): p. 5194-5205.

91. Miyagawa, H., M. Misra, and A.K. Mohanty, *Mechanical properties of carbon nanotubes and their polymer nanocomposites.* Journal of Nanoscience and Nanotechnology, 2005. **5**(10): p. 1593-1615.

92. Hwang, G.L., Y.T. Shieh, and K.C. Hwang, *Efficient load transfer to polymer-grafted multiwalled carbon nanotubes in polymer composites.* Advanced Functional Materials, 2004. **14**(5): p. 487-491.

93. Coleman, J.N., U. Khan, W.J. Blau, and Y.K. Gun'ko, *Small but strong: A review of the mechanical properties of carbon nanotube-polymer composites.* Carbon, 2006. **44**(9): p. 1624-1652.

94. Coleman, J.N., M. Cadek, K.P. Ryan, A. Fonseca, J.B. Nagy, W.J. Blau, and M.S. Ferreira, *Reinforcement of polymers with carbon nanotubes. The role of an ordered polymer interfacial region. Experiment and modeling.* Polymer, 2006. **47**(26): p. 8556-8561.

95. Cadek, M., J.N. Coleman, K.P. Ryan, V. Nicolosi, G. Bister, A. Fonseca, J.B. Nagy, K. Szostak, F. Beguin, and W.J. Blau, *Reinforcement of polymers with carbon nanotubes: The role of nanotube surface area.* Nano Letters, 2004. **4**(2): p. 353-356.

96. Cadek, M., J.N. Coleman, V. Barron, K. Hedicke, and W.J. Blau, *Morphological and mechanical properties of carbon-nanotube-reinforced semicrystalline and amorphous polymer composites.* Applied Physics Letters, 2002. **81**(27): p. 5123-5125.

97. Breuer, O. and U. Sundararaj, *Big returns from small fibers: A review of polymer/carbon nanotube composites.* Polymer Composites, 2004. **25**(6): p. 630-645.

98. Andrews, R. and M.C. Weisenberger, *Carbon nanotube polymer composites.* Current Opinion in Solid State & Materials Science, 2004. **8**(1): p. 31-37.

99. Ajayan, P.M., O. Stephan, C. Colliex, and D. Trauth, *ALIGNED CARBON NANOTUBE ARRAYS FORMED BY CUTTING A POLYMER RESIN-NANOTUBE COMPOSITE.* Science, 1994. **265**(5176): p. 1212-1214.

100. Thostenson, E.T., Z.F. Ren, and T.W. Chou, *Advances in the science and technology of carbon nanotubes and their composites: a review.* Composites Science and Technology, 2001. **61**(13): p. 1899-1912.

101. Chang, T.E., L.R. Jensen, A. Kisliuk, R.B. Pipes, R. Pyrz, and A.P. Sokolov, *Microscopic mechanism of reinforcement in single-wall carbon nanotube/polypropylene nanocomposite.* Polymer, 2005. **46**(2): p. 439-444.

102. Kearns, J.C. and R.L. Shambaugh, *Polypropylene fibers reinforced with carbon nanotubes.* Journal of Applied Polymer Science, 2002. **86**(8): p. 2079-2084.

103. Velasco-Santos, C., A.L. Martínez-Hernández, F.T. Fisher, R. Ruoff, and V.M. Castaño, *Improvement of Thermal and Mechanical Properties of Carbon Nanotube Composites through Chemical Functionalization.* Chemistry of Materials, 2003. **15**(23): p. 4470-4475.

104. Gong, X., J. Liu, S. Baskaran, R.D. Voise, and J.S. Young, *Surfactant-Assisted Processing of Carbon Nanotube/Polymer Composites.* Chemistry of Materials, 2000. **12**(4): p. 1049-1052.

105. Dewei, Q., H. Jeffrey, and H. Gouwei, *Molecular dynamics simulation of thermal and mechanical properties of polyimide–carbon-nanotube composites.* Modelling and Simulation in Materials Science and Engineering, 2005. **13**(4): p. 493.

106. Han, Y. and J. Elliott, *Molecular dynamics simulations of the elastic properties of polymer/carbon nanotube composites.* Computational Materials Science, 2007. **39**(2): p. 315-323.

107. Frankland, S.J.V., V.M. Harik, G.M. Odegard, D.W. Brenner, and T.S. Gates, *The stress–strain behavior of polymer–nanotube composites from molecular dynamics simulation.* Composites Science and Technology, 2003. **63**(11): p. 1655-1661.

108. Frankland, S.J.V., A. Caglar, D.W. Brenner, and M. Griebel, *Molecular Simulation of the Influence of Chemical Cross-Links on the Shear Strength of Carbon Nanotube−Polymer Interfaces.* The Journal of Physical Chemistry B, 2002. **106**(12): p. 3046-3048.

109. Liu, J., L. Zhang, D. Cao, and W. Wang, *Static, rheological and mechanical properties of polymer nanocomposites studied by computer modeling and simulation.* Physical Chemistry Chemical Physics, 2009. **11**(48): p. 11365-11384.

110. Erik, T.T. and C. Tsu-Wei, *On the elastic properties of carbon nanotube-based composites: modelling and characterization.* Journal of Physics D: Applied Physics, 2003. **36**(5): p. 573.

111. Seidel, G.D. and D.C. Lagoudas, *Micromechanical analysis of the effective elastic properties of carbon nanotube reinforced composites.* Mechanics of Materials, 2006. **38**(8–10): p. 884-907.

112. Haque, A. and A. Ramasetty, *Theoretical study of stress transfer in carbon nanotube reinforced polymer matrix composites.* Composite Structures, 2005. **71**(1): p. 68-77.

113. Gao, X.L. and K. Li, *A shear-lag model for carbon nanotube-reinforced polymer composites.* International Journal of Solids and Structures, 2005. **42**(5–6): p. 1649-1667.

114. Tsai, J.-L., S.-H. Tzeng, and Y.-T. Chiu, *Characterizing elastic properties of carbon nanotubes/polyimide nanocomposites using multi-scale simulation.* Composites Part B: Engineering, 2010. **41**(1): p. 106-115.

115. Gates, T.S., G.M. Odegard, S.J.V. Frankland, and T.C. Clancy, *Computational materials: Multi-scale modeling and simulation of nanostructured materials.* Composites Science and Technology, 2005. **65**(15–16): p. 2416-2434.

116. Zare, Y. and H. Garmabi, *Attempts to Simulate the Modulus of Polymer/Carbon Nanotube Nanocomposites and Future Trends.* Polymer Reviews, 2014. **54**(3): p. 377-400.

117. Mallick, P.K., *Fiber-reinforced composites: materials, manufacturing, and design*. 2007, Boca Raton: Taylor & Francis.

118. Ozkan, T., Q. Chen, and I. Chasiotis, *Interfacial strength and fracture energy of individual carbon nanofibers in epoxy matrix as a function of surface conditions.* Composites Science and Technology, 2012. **72**(9): p. 965-975.

119. Barber, A.H., S.R. Cohen, and H.D. Wagner, *Measurement of carbon nanotube–polymer interfacial strength.* Applied Physics Letters, 2003. **82**(23): p. 4140-4142.

120. Tsuda, T., T. Ogasawara, F. Deng, and N. Takeda, *Direct measurements of interfacial shear strength of multi-walled carbon nanotube/PEEK composite using a nano-pullout method.* Composites Science and Technology, 2011. **71**(10): p. 1295-1300.

121. Chen, X., M. Zheng, C. Park, and C. Ke, *Direct Measurements of the Mechanical Strength of Carbon Nanotube–Poly(methyl methacrylate) Interfaces.* Small, 2013. **9**(19): p. 3345-3351.

122. Gou, J., B. Minaie, B. Wang, Z. Liang, and C. Zhang, *Computational and experimental study of interfacial bonding of single-walled nanotube reinforced composites.* Computational Materials Science, 2004. **31**(3–4): p. 225-236.

123. Liao, K. and S. Li, *Interfacial characteristics of a carbon nanotube–polystyrene composite system.* Applied Physics Letters, 2001. **79**(25): p. 4225-4227.

124. Roy, D., S. Bhattacharyya, A. Rachamim, A. Plati, and M.-L. Saboungi, *Measurement of interfacial shear strength in single wall carbon nanotubes reinforced composite using Raman spectroscopy.* Journal of Applied Physics, 2010. **107**(4): p. 043501.

125. Newcomb, B.A., H.G. Chae, P.V. Gulgunje, K. Gupta, Y. Liu, D.E. Tsentalovich, M. Pasquali, and S. Kumar, *Stress transfer in polyacrylonitrile/carbon nanotube composite fibers.* Polymer, 2014. **55**(11): p. 2734-2743.

126. Huang, Y. and R.J. Young, *Effect of fibre microstructure upon the modulus of PAN- and pitch-based carbon fibres.* Carbon, 1995. **33**(2): p. 97-107.

127. Cronin, S.B., A.K. Swan, M.S. Ünlü, B.B. Goldberg, M.S. Dresselhaus, and M. Tinkham, *Resonant Raman spectroscopy of individual metallic and semiconducting single-wall carbon nanotubes under uniaxial strain.* Physical Review B, 2005. **72**(3): p. 035425.

128. Kumar, R. and S.B. Cronin, *Raman scattering of carbon nanotube bundles under axial strain and strain-induced debundling.* Physical Review B, 2007. **75**(15): p. 155421.

129. Huong, P.V., R. Cavagnat, P.M. Ajayan, and O. Stephan, *Temperature-dependent vibrational spectra of carbon nanotubes.* Physical Review B, 1995. **51**(15): p. 10048-10051.

130. Chang, C.-C., I.K. Hsu, M. Aykol, W.-H. Hung, C.-C. Chen, and S.B. Cronin, *A New Lower Limit for the Ultimate Breaking Strain of Carbon Nanotubes.* ACS Nano, 2010. **4**(9): p. 5095-5100.

131. May, 2016]; Available from: http://energy.gov/articles/top-9-things-you-didn-t-know-about-carbon-fiber.

132. Chae, H.G., Y.H. Choi, M.L. Minus, and S. Kumar, *Carbon nanotube reinforced small diameter polyacrylonitrile based carbon fiber.* Composites Science and Technology, 2009. **69**(3–4): p. 406-413.

133. Newcomb, B.A., L.A. Giannuzzi, K.M. Lyons, P.V. Gulgunje, K. Gupta, Y. Liu, M. Kamath, K. McDonald, J. Moon, B. Feng, G.P. Peterson, H.G. Chae, and S. Kumar, *High resolution transmission electron microscopy study on polyacrylonitrile/carbon nanotube based carbon fibers and the effect of structure development on the thermal and electrical conductivities.* Carbon, 2015. **93**: p. 502-514.

134. Wojdyr, M., *http://debyer.readthedocs.org/en/latest/*. 2011.

135. Baskaran, D., J.W. Mays, and M.S. Bratcher, *Noncovalent and Nonspecific Molecular Interactions of Polymers with Multiwalled Carbon Nanotubes.* Chemistry of Materials, 2005. **17**(13): p. 3389-3397.

136. Nishio, M., Y. Umezawa, M. Hirota, and Y. Takeuchi, *The CH/π interaction: Significance in molecular recognition.* Tetrahedron, 1995. **51**(32): p. 8665-8701.

137. Kodama, Y., K. Nishihata, M. Nishio, and N. Nakagawa, *Attractive interaction between aliphatic and aromatic systems.* Tetrahedron Letters, 1977. **18**(24): p. 2105-2108.

138. O'Connell, M.J., S. Sivaram, and S.K. Doorn, *Near-infrared resonance Raman excitation profile studies of single-walled carbon nanotube intertube interactions: A direct comparison of bundled and individually dispersed.* Physical Review B, 2004. **69**(23): p. 235415.

139. Mayo, M.L., D. Hogle, B. Yilmaz, M.E. Kose, and S. Kilina, *Morphology and dispersion of polycarbazole wrapped carbon nanotubes.* RSC Advances, 2013. **3**(43): p. 20492-20502.

140. Heller, D.A., P.W. Barone, J.P. Swanson, R.M. Mayrhofer, and M.S. Strano, *Using Raman Spectroscopy to Elucidate the Aggregation State of Single-Walled Carbon Nanotubes.* The Journal of Physical Chemistry B, 2004. **108**(22): p. 6905-6909.

141. Bonhommeau, S., P. Deria, M.G. Glesner, D. Talaga, S. Najjar, C. Belin, L. Auneau, S. Trainini, M.J. Therien, and V. Rodriguez, *Raman Spectroscopic Investigation of Individual Single-Walled Carbon Nanotubes Helically Wrapped by Ionic, Semiconducting Polymers.* The Journal of Physical Chemistry C, 2013. **117**(28): p. 14840-14849.

142. Fantini, C., A. Jorio, A.P. Santos, V.S.T. Peressinotto, and M.A. Pimenta, *Characterization of DNA-wrapped carbon nanotubes by resonance Raman and optical absorption spectroscopies.* Chemical Physics Letters, 2007. **439**(1–3): p. 138-142.

143. Quan-Hong, Y., G. Nittaya, J.O. Claudio, L. Feng, V. Alun, S. Riichiro, S.N. Iris, T. Zhi-Yuan, C. Hui-Ming, B. Tom, and H.L. Wei, *A Raman probe for selective wrapping of single-walled carbon nanotubes by DNA.* Nanotechnology, 2007. **18**(40): p. 405706.

144. Wonsuk, J., W. Ju Yeon, L. Seung Ho, K. Duckjong, K. Soohyun, and H. Chang-Soo, *Evaluation of the individualization state in single-walled carbon nanotube solutions using absorption, Raman and photoluminescence spectroscopy.* Measurement Science and Technology, 2012. **23**(12): p. 125501.

145. Kuzmany, H., W. Plank, M. Hulman, C. Kramberger, A. Grüneis, T. Pichler, H. Peterlik, H. Kataura, and Y. Achiba, *Determination of SWCNT diameters from the Raman response of the radial breathing mode.* Eur. Phys. J. B, 2001. **22**(3): p. 307-320.

146. El-Kady, M.F., V. Strong, S. Dubin, and R.B. Kaner, *Laser Scribing of High-Performance and Flexible Graphene-Based Electrochemical Capacitors.* Science, 2012. **335**(6074): p. 1326-1330.

147. Pech, D., M. Brunet, H. Durou, P. Huang, V. Mochalin, Y. Gogotsi, P.-L. Taberna, and P. Simon, *Ultrahigh-power micrometre-sized supercapacitors based on onion-like carbon.* Nat Nano, 2010. **5**(9): p. 651-654.

148. Demczyk, B.G., Y.M. Wang, J. Cumings, M. Hetman, W. Han, A. Zettl, and R.O. Ritchie, *Direct mechanical measurement of the tensile strength and elastic modulus of multiwalled carbon nanotubes.* Materials Science and Engineering: A, 2002. **334**(1–2): p. 173-178.

149. Yu, M.-F., B.S. Files, S. Arepalli, and R.S. Ruoff, *Tensile Loading of Ropes of Single Wall Carbon Nanotubes and their Mechanical Properties.* Physical Review Letters, 2000. **84**(24): p. 5552-5555.

150. Yu, M.-F., O. Lourie, M.J. Dyer, K. Moloni, T.F. Kelly, and R.S. Ruoff, *Strength and Breaking Mechanism of Multiwalled Carbon Nanotubes Under Tensile Load.* Science, 2000. **287**(5453): p. 637-640.

151. Mathur, R.B., S. Pande, B.P. Singh, and T.L. Dhami, *Electrical and mechanical properties of multi-walled carbon nanotubes reinforced PMMA and PS composites.* Polymer Composites, 2008. **29**(7): p. 717-727.

152. Blond, D., V. Barron, M. Ruether, K.P. Ryan, V. Nicolosi, W.J. Blau, and J.N. Coleman, *Enhancement of Modulus, Strength, and Toughness in Poly(methyl methacrylate)-Based Composites by the Incorporation of Poly(methyl methacrylate)-Functionalized Nanotubes.* Advanced Functional Materials, 2006. **16**(12): p. 1608-1614.

153. Gorga, R.E. and R.E. Cohen, *Toughness enhancements in poly(methyl methacrylate) by addition of oriented multiwall carbon nanotubes.* Journal of Polymer Science Part B: Polymer Physics, 2004. **42**(14): p. 2690-2702.

154. Sabba, Y. and E.L. Thomas, *High-Concentration Dispersion of Single-Wall Carbon Nanotubes.* Macromolecules, 2004. **37**(13): p. 4815-4820.

155. Kim, K.H. and W.H. Jo, *Improvement of tensile properties of poly(methyl methacrylate) by dispersing multi-walled carbon nanotubes functionalized with poly(3-hexylthiophene)-graft-poly(methyl methacrylate).* Composites Science and Technology, 2008. **68**(9): p. 2120-2124.

156. Lahelin, M., A. Vesterinen, A. Nykänen, J. Ruokolainen, and J. Seppälä, *In situ polymerization of methyl methacrylate/multi-walled carbon nanotube composites using cationic stearyl methacrylate copolymers as dispersants.* European Polymer Journal, 2011. **47**(5): p. 873-881.

157. Boge, J., L.J. Sweetman, M. in het Panhuis, and S.F. Ralph, *The effect of preparation conditions and biopolymer dispersants on the properties of SWNT buckypapers.* Journal of Materials Chemistry, 2009. **19**(48): p. 9131-9140.

158. Che, J., P. Chen, and M.B. Chan-Park, *High-strength carbon nanotube buckypaper composites as applied to free-standing electrodes for supercapacitors.* Journal of Materials Chemistry A, 2013. **1**(12): p. 4057.

159. Giang, T.P., P. Young-Bin, W. Shiren, L. Zhiyong, W. Ben, Z. Chuck, F. Percy, and K. Leslie, *Mechanical and electrical properties of polycarbonate nanotube buckypaper composite sheets.* Nanotechnology, 2008. **19**(32): p. 325705.

160. Guo, H., T.V. Sreekumar, T. Liu, M. Minus, and S. Kumar, *Structure and properties of polyacrylonitrile/single wall carbon nanotube composite films.* Polymer, 2005. **46**(9): p. 3001-3005.

161. Zhang, X., T.V. Sreekumar, T. Liu, and S. Kumar, *Properties and Structure of Nitric Acid Oxidized Single Wall Carbon Nanotube Films.* The Journal of Physical Chemistry B, 2004. **108**(42): p. 16435-16440.

162. Cooper, C.A., R.J. Young, and M. Halsall, *Investigation into the deformation of carbon nanotubes and their composites through the use of Raman spectroscopy.* Composites Part A: Applied Science and Manufacturing, 2001. **32**(3–4): p. 401-411.

163. Cronin, S.B., A.K. Swan, M.S. Ünlü, B.B. Goldberg, M.S. Dresselhaus, and M. Tinkham, *Measuring the Uniaxial Strain of Individual Single-Wall Carbon Nanotubes: Resonance Raman Spectra of Atomic-Force-Microscope Modified Single-Wall Nanotubes.* Physical Review Letters, 2004. **93**(16): p. 167401.

164. Bakhtiary Davijani, A.A. and S. Kumar, *Ordered wrapping of poly(methyl methacrylate) on single wall carbon nanotubes.* Polymer, 2015. **70**: p. 278-281.

165. Affdl, J.C.H. and J.L. Kardos, *The Halpin-Tsai equations: A review.* Polymer Engineering & Science, 1976. **16**(5): p. 344-352.

166. Rosenthal, J., *A model for determining fiber reinforcement efficiencies and fiber orientation in polymer composites.* Polymer Composites, 1992. **13**(6): p. 462-466.

167. Omidi, M., H. Rokni D.T, A.S. Milani, R.J. Seethaler, and R. Arasteh, *Prediction of the mechanical characteristics of multi-walled carbon nanotube/epoxy composites using a new form of the rule of mixtures.* Carbon, 2010. **48**(11): p. 3218-3228.

168. Shao, L.H., R.Y. Luo, S.L. Bai, and J. Wang, *Prediction of effective moduli of carbon nanotube–reinforced composites with waviness and debonding.* Composite Structures, 2009. **87**(3): p. 274-281.

169. Fisher, F.T., R.D. Bradshaw, and L.C. Brinson, *Fiber waviness in nanotube-reinforced polymer composites—I: Modulus predictions using effective nanotube properties.* Composites Science and Technology, 2003. **63**(11): p. 1689-1703.

170. Basu-Dutt, S., M.L. Minus, R. Jain, D. Nepal, and S. Kumar, *Chemistry of Carbon Nanotubes for Everyone.* Journal of Chemical Education, 2012. **89**(2): p. 221-229.

171. Bachilo, S.M., M.S. Strano, C. Kittrell, R.H. Hauge, R.E. Smalley, and R.B. Weisman, *Structure-Assigned Optical Spectra of Single-Walled Carbon Nanotubes.* Science, 2002. **298**(5602): p. 2361-2366.

172. Patra, N., A.C. Barone, and M. Salerno, *Solvent Effects on the Thermal and Mechanical Properties of Poly(methyl methacrylate) Casted from Concentrated Solutions.* Advances in Polymer Technology, 2011. **30**(1): p. 12-20.

173. Jin, Z., K.P. Pramoda, G. Xu, and S.H. Goh, *Dynamic Mechanical Behavior of Melt-Processed Multi-Walled Carbon Nanotube/Poly(methyl methacrylate) Composites.* Chemical Physics Letters, 2001. **337**(1–3): p. 43-47.

174. Tsagaropoulos, G. and A. Eisenberg, *Dynamic Mechanical Study of the Factors Affecting the Two Glass Transition Behavior of Filled Polymers. Similarities and Differences with Random Ionomers.* Macromolecules, 1995. **28**(18): p. 6067-6077.

175. Shaffer, M.S.P. and A.H. Windle, *Fabrication and Characterization of Carbon Nanotube/Poly(vinyl alcohol) Composites.* Advanced Materials, 1999. **11**(11): p. 937-941.

176. Liu, H.C., A.-T. Chien, B.A. Newcomb, Y. Liu, and S. Kumar, *Processing, Structure, and Properties of Lignin- and CNT-Incorporated Polyacrylonitrile-Based Carbon Fibers.* ACS Sustainable Chemistry & Engineering, 2015. **3**(9): p. 1943-1954.

177. Liu, H.C., A.-T. Chien, B.A. Newcomb, A.A. Bakhtiary Davijani, and S. Kumar, *Stabilization kinetics of gel spun polyacrylonitrile/lignin blend fiber*. Carbon, 2016. **101**: p. 382-389.

178. Chae, H.G., M.L. Minus, and S. Kumar, *Oriented and exfoliated single wall carbon nanotubes in polyacrylonitrile.* Polymer, 2006. **47**(10): p. 3494-3504.

179. Liu, T., Z. Xiao, and B. Wang, *The exfoliation of SWCNT bundles examined by simultaneous Raman scattering and photoluminescence spectroscopy.* Carbon, 2009. **47**(15): p. 3529-3537.

180. Lee, G.-W., S. Jagannathan, H.G. Chae, M.L. Minus, and S. Kumar, *Carbon nanotube dispersion and exfoliation in polypropylene and structure and properties of the resulting composites.* Polymer, 2008. **49**(7): p. 1831-1840.

181. Kusner, I. and S. Srebnik, *Conformational behavior of semi-flexible polymers confined to a cylindrical surface.* Chemical Physics Letters, 2006. **430**(1–3): p. 84-88.

182. Tallury, S.S. and M.A. Pasquinelli, *Molecular Dynamics Simulations of Polymers with Stiff Backbones Interacting with Single-Walled Carbon Nanotubes.* The Journal of Physical Chemistry B, 2010. **114**(29): p. 9349-9355.

183. Chen, J., H. Liu, W.A. Weimer, M.D. Halls, D.H. Waldeck, and G.C. Walker, *Noncovalent Engineering of Carbon Nanotube Surfaces by Rigid, Functional Conjugated Polymers.* Journal of the American Chemical Society, 2002. **124**(31): p. 9034-9035.

184. Yang, M., V. Koutsos, and M. Zaiser, *Interactions between Polymers and Carbon Nanotubes: A Molecular Dynamics Study.* The Journal of Physical Chemistry B, 2005. **109**(20): p. 10009-10014.

185. Conley, R.T. and J.F. Bieron, *Examination of the oxidative degradation of polyacrylonitrile using infrared spectroscopy.* Journal of Applied Polymer Science, 1963. **7**(5): p. 1757-1773.

186. Gupta, A.K., D.K. Paliwal, and P. Bajaj, *Acrylic Precursors for Carbon Fibers.* Journal of Macromolecular Science, Part C, 1991. **31**(1): p. 1-89.

187. Chae, H.G., M.L. Minus, A. Rasheed, and S. Kumar, *Stabilization and carbonization of gel spun polyacrylonitrile/single wall carbon nanotube composite fibers.* Polymer, 2007. **48**(13): p. 3781-3789.

188. Duan, H., E. Xie, L. Han, and Z. Xu, *Turning PMMA Nanofibers into Graphene Nanoribbons by In Situ Electron Beam Irradiation.* Advanced Materials, 2008. **20**(17): p. 3284-3288.

189. Huigao, D., Z. Jianguo, Z. Yongzhe, X. Erqing, and H. Li, *Preparing patterned carbonaceous nanostructures directly by overexposure of PMMA using electron-beam lithography.* Nanotechnology, 2009. **20**(13): p. 135306.

190. Ganesh, K., R. Latha, K. Kishore, B. George, and K.N. Ninan, *Stabilization of thermal degradation of poly(methyl methacrylate) by polysulfide polymers.* Journal of Applied Polymer Science, 1997. **66**(11): p. 2149-2156.

191. Laachachi, A., D. Ruch, F. Addiego, M. Ferriol, M. Cochez, and J.M. Lopez Cuesta, *Effect of ZnO and organo-modified montmorillonite on thermal degradation of poly(methyl methacrylate) nanocomposites.* Polymer Degradation and Stability, 2009. **94**(4): p. 670-678.

192. Dong, Y., Z. Gui, S. Jiang, Y. Hu, and K. Zhou, *Carbonization of Poly(methyl methacrylate) by Incorporating Hydroxyapatite Nanorods during Thermal Degradation.* Industrial & Engineering Chemistry Research, 2011. **50**(19): p. 10903-10909.

193. Hirata, T., T. Kashiwagi, and J.E. Brown, *Thermal and oxidative degradation of poly(methyl methacrylate): weight loss.* Macromolecules, 1985. **18**(7): p. 1410-1418.

194. Manring, L.E., *Thermal degradation of poly(methyl methacrylate). 2. Vinyl-terminated polymer.* Macromolecules, 1989. **22**(6): p. 2673-2677.

195. Liu, Y., H.G. Chae, and S. Kumar, *Gel-spun carbon nanotubes/polyacrylonitrile composite fibers. Part I: Effect of carbon nanotubes on stabilization.* Carbon, 2011. **49**(13): p. 4466-4476.

196. Yu, J.F.S., J.L. Zakin, and G.K. Patterson, *Mechanical degradation of high molecular weight polymers in dilute solution.* Journal of Applied Polymer Science, 1979. **23**(8): p. 2493-2512.

197. Brostow, W., *Drag reduction and mechanical degradation in polymer solutions in flow*. Polymer, 1983. **24**(5): p. 631-638.

198. Henglein, A. and M. Gutierrez, *Sonolysis of polymers in aqueous solution. New observations on pyrolysis and mechanical degradation.* The Journal of Physical Chemistry, 1988. **92**(13): p. 3705-3707.

199. Fan, Z. and S.G. Advani, *Rheology of multiwall carbon nanotube suspensions.* Journal of Rheology, 2007. **51**(4): p. 585-604.

200. Huang, Y.Y., S.V. Ahir, and E.M. Terentjev, *Dispersion rheology of carbon nanotubes in a polymer matrix.* Physical Review B, 2006. **73**(12): p. 125422.

201. Ratzsch, K.-F., V. Cecen, F. Tölle, K.-A. Wartig, R. Thomann, R. Mülhaupt, and C. Friedrich, *Rheology, Electrical Properties, and Percolation of TRGO-Filled EVA-Copolymers.* Macromolecular Materials and Engineering, 2014. **299**(9): p. 1134-1144.

202. Hine, P.J. and I.M. Ward, *Measuring the elastic properties of high-modulus fibres.* Journal of Materials Science, 1996. **31**(2): p. 371-379.

203. Loidl, D., O. Paris, H. Rennhofer, M. Müller, and H. Peterlik, *Skin-core structure and bimodal Weibull distribution of the strength of carbon fibers.* Carbon, 2007. **45**(14): p. 2801-2805.

204. Wang, H., Y. Wang, T. Li, S. Wu, and L. Xu, *Gradient distribution of radial structure of PAN-based carbon fiber treated by high temperature.* Progress in Natural Science: Materials International, 2014. **24**(1): p. 31-34.